Florida State University Libraries

2013

Photoproduction of # Mesons and ### Meson Pairs off the Free Proton

Andrew Matthew Wilson

THE FLORIDA STATE UNIVERSITY

COLLEGE OF ARTS AND SCIENCES

PHOTOPRODUCTION OF ω MESONS AND $\pi^0\omega$ MESON PAIRS OFF THE

FREE PROTON

By

ANDREW MATTHEW WILSON

A Dissertation submitted to the
Department of Physics
in partial fulfillment of the
requirements for the degree of
Doctor of Philosophy

Degree Awarded:
Spring Semester, 2013

Andrew Matthew Wilson defended this dissertation on December 5, 2012.

The members of the supervisory committee were:

Volker Crede
Professor Directing Thesis

Philip Sura
University Representative

Paul Eugenio
Committee Member

Winston Roberts
Committee Member

Joseph Owens
Committee Member

The Graduate School has verified and approved the above-named committee members, and certifies that the dissertation has been approved in accordance with the university requirements.

To my family, who supported me so well during this process.

ACKNOWLEDGMENTS

First and foremost, I would like to thank Dr. Volker Crede for all the great advice and support throughout my time here at Florida State. I could not have asked for a better adviser. I would also like to thank all of the professors and staff at the Florida State University Physics department for creating a great atmosphere for learning and growth.

At the experiment site in Bonn, Germany, the staff, professors and students were wonderfully helpful to me during my time working with the experiment. I also would like to thank Aaron McVeigh for helping me acclimate initially to living in Bonn.

Many thanks to Dr. Winston Roberts for helping me through many calculations and other mathematical troubles. Even though not much progress came from this work, I learned huge amounts about the mathematical concepts behind describing amplitudes. I would like to thank several of my fellow graduate students for great conversations and good times during my time here.

And finally, I would like to thank the members of my PhD committee for their work in reading and considering this thesis.

TABLE OF CONTENTS

LIST OF TABLES

LIST OF FIGURES

x

xi

LIST OF SYMBOLS

The following short list of symbols are used throughout the document. The symbols represent quantities that I tried to use consistently.

p	Proton
n	Neutron
eV	eEectron volts - A measure of energy
MeV	Mega electron volts $= 10^6$ eV
GeV	Giga electron volts $= 1000$ MeV
c	Speed of light
π^0	Uncharged pion meson - The lightest, uncharged meson with mass ≈ 135 MeV/c^2
ω	Omega meson - The uncharged meson with mass ≈ 782 MeV/c^2
γ	Photon - quantum of electromagnetic radiation
η	Eta meson - The uncharged pseudo scalar meson with mass ≈ 548 MeV/c^2
$\hat{q}$	A unit vector in three dimensional space
i	Imaginary number $= \sqrt{-1}$
c.m.	Center-of-mass frame. The frame of reference where the sum of momenta of all particles is zero.

ABSTRACT

The photoproduction of ω mesons and $\pi^0\omega$ meson pairs is studied with the intention of providing data which will be useful in isolating baryon resonances. The data used for this analysis was recorded using the CBELSA/TAPS experiment in Bonn, Germany during October-November 2002. This experiment used photons incident upon free (unbound) protons, which were contained in a liquid hydrogen target. The differential cross sections for $\gamma p \rightarrow p\omega$ reaction are presented for the first time by analyzing the ω meson in its radiative decay. The differential cross sections for the $\gamma p \rightarrow p\pi^0\omega$ are also presented for the first time with enough statistics and resolution to isolate baryon resonances. The initial photon energies range from threshold for each reaction to 2.5 GeV. These data show the full kinematic range of the differential cross sections for both reactions.

In addition to the differential cross sections, the spin-density matrix elements have been extracted for the $\gamma p \rightarrow p\omega$ reaction. The unpolarized spin-density matrix elements are presented from threshold up to 2.5 GeV in initial photon energy and show remarkable agreement with previous analyses over a large angular range. Unpolarized measurements in the very forward direction are, for the first time, presented with a resolution useful for isolating baryon resonances. Also, the polarized spin-density matrix elements, ρ^1_{00} and ρ^1_{11}, are reported for the first time. These polarized elements were reported from threshold up to 1.7 GeV in initial photon energy. These spin-density matrix elements indicate the relative rate at which ω mesons are produced with a certain spin projection and will be useful in learning about the spin dynamics of the intermediate processes and any contributing baryon resonances.

CHAPTER 1

INTRODUCTION

Since very nearly after the discovery of protons and neutrons, nucleons (protons and neutrons) have been known to be composite particles. The compositeness of nucleons along with the knowledge of quantum mechanics suggest these nucleons have a discrete pattern of excited states. This pattern of excited states depends upon the nature of the constituent particles and the forces binding them together.

Answering the question of what these constituent particles are and what is the nature of the force holding them together has been one of the most challenging questions in physics over the last few decades. The effort put towards the answering of this question has been enormous with the construction of particle accelerators devoted to measuring these excited states and the other properties of the nucleons.

The constituent particles responsible for the overall properties of the nucleon are called quarks and gluons. These quarks and gluons are currently believed to be fundamental particles (i.e. non-composite particles). Table 1.1 shows some of the known properties of the quarks. The gluon is the particle responsible for carrying the strong force which binds the quarks together.

Particles made of quarks are called hadrons. Quarks have only been found to exist in particles either in a system of 2 bound quarks (mesons) or 3 bound quarks (baryons). The lowest mass baryons are the nucleons, proton and neutron. The proton, the ground state baryon, is made of two up quarks and one down quark and its mass is 938.272 MeV/c^2. When the mass of these three quarks are summed and compared to the overall mass of the proton, more than 98% of the mass is unaccounted for. This extra mass is a result of the interaction between the quarks, quark kinetic energy, and a "sea" of quark anti-quark pairs and gluons.

1.1   Properties of Hadrons

Hadrons have quantum numbers which describe their properties. The important quantities for the discussion of hadrons, for the purposes of this thesis, are intrinsic spin, parity, isospin, strangeness, charmness, bottomness, topness, and baryon num-

1

Table 1.1: Quark Properties. Obtained from [1]. The charge is reported in relation to the absolute value of the charge of the electron (e).

Name	Symbol	Charge(e)	Mass(MeV/c^2)
up	u	+2/3	1.7-3.1
down	d	-1/3	4.1-5.7
strange	s	-1/3	100^{+30}_{-20}
charm	c	+2/3	1290^{+50}_{-110}
bottom	b	-1/3	4190^{+180}_{-60}
top	t	+2/3	$172,900 \pm 600 \pm 800$

ber. Each one of these quantities is "quantized" and is not a continuous number but has a discrete value.

The strangeness, charmness, bottomness, and topness quantum numbers refer to the quark content of the hadron. Since the hadrons discussed in this thesis have low masses (below 3 GeV/c^2), charmness, bottomness and topness are all zero because there is not enough energy to generate these flavors of quark.

The strangeness quantum number is a measure of the overall number of strange quarks inside a hadron (times -1, by convention). For a hadron to have strangeness of zero, the hadron must either have no strange quarks or have both a strange quark and an anti-strange quark (anti-matter version of the strange quark). The π^0 and ω mesons have zero strangeness. Therefore any baryon decaying to these mesons and a proton (zero strangeness) must have zero strangeness. This decay must happen via the strong interaction, which conserves strangeness.

Baryon number is a quantity which is universally conserved. No interaction can change the number of baryons. Baryons have baryon number $B = 1$. Mesons have baryon number $B = 0$. For example, the reactions considered in this thesis, $\gamma p \rightarrow p\omega$ and $\gamma p \rightarrow p\pi^0\omega$, each have one baryon in the initial state (proton) and one baryon in the final state (proton).

Isospin is a quantum number which describes the number of up and down quarks which are in a hadron. The up quark is assigned a total isospin of $I = 1/2$ and isospin projection of $I_z = 1/2$. The down quark is assigned a total isospin $I = 1/2$ and isospin projection of $I_z = -1/2$. The addition of isospin follows the vector addition rules for spin. The ω meson is a symmetric combination of isospin forming an overall isospin of $I = 0$ and therefore its isospin projection is $I_z = 0$. The π^0 meson has a total isospin $I = 1$ and projection of $I_z = 0$. The π^0 is part of a triplet of pions π^-, π^0, and π^+, which all have total isospin $I = 1$ and projection $I_z = -1, 0, 1$, respectively. The proton has isospin $I = 1/2$ and, by convention, projection $I_z = 1/2$. The neutron has isospin $I = 1/2$ and projection $I_z = -1/2$. From the total isospin quantum number, the number of projections (and therefore particles) is $2I + 1$. Therefore, the nucleon collectively has a total isospin $I = 1/2$ with two projections $I_z = 1/2$, the proton, and $I_z = -1/2$, the neutron.

2

The parity of a particle is the quantum number describing the behavior of its wavefunction when a parity transformation is performed. A parity transformation in three dimensions occurs when the Cartesian coordinates (x, y, z) are transformed into $(-x, -y, -z)$. If this operation is applied to the wavefunction of a particle $|\phi\rangle$, then the parity quantum number (P) is defined as

$$\hat{P}|\phi\rangle = P|\phi\rangle \quad , \tag{1.1}$$

where $\hat{P}$ is the quantum mechanical operator which does the parity transformation. The π^0 and ω meson both have negative parity. The proton and neutron have positive parity.

The intrinsic spin of each particle follows the rules of vector addition. A particle of total spin S has $2S + 1$ spin projections. Therefore, an ω meson with spin $S = 1$ has three spin projections $-1, 0, 1$. Mesons have integer spins $(S = 0, 1, 2, ...)$ and are labeled as bosons. Baryons have half odd integer spins $(S = 1/2, 3/2, 5/2, ...)$ and are labeled as fermions. A particularly interesting consequence of intrinsic spin is the statistics rules these particles obey. Fermions obey Fermi-Dirac Statistics, which follow the Pauli Exclusion Principle. This principle states that identical fermions in the same system cannot occupy the same quantum state at the same time. However, bosons do not obey these statistics.

1.1.1 Baryon Nomenclature

Baryons are labeled with their quantum numbers and mass. The name of a baryon is identified by the quark flavor content, which is specified by the quantum numbers: isospin, strangeness, charmness, bottomness, and topness. The labels for baryons which contain only up, down, and strange quarks are given in Table 1.2.

Table 1.2: Light Quark Baryon Labels.   The baryons listed are only those with no charm, bottom, or top quarks.

Label	Isospin	Strangeness
N	1/2	0
Δ	3/2	0
Λ	0	−1
Σ	1	−1
Ξ	1/2	−2
Ω	0	−3

When a baryon resonance is being identified in this thesis, the nomenclature is

$$Label(Mass)Spin^{Parity} \quad , \tag{1.2}$$

where Label is one of the labels in Table 1.2, Mass is in MeV/c^2, Spin is the intrinsic spin, and Parity is the parity of the state. For instance, the spin $S = 3/2$ baryon

3

with isospin $I = 3/2$, zero strangeness, parity $P = +1$, and mass $M = 1232$ MeV/c^2 is called $\Delta(1232)\frac{3}{2}^+$.

1.2 Theoretical Situation

1.2.1 Quantum Chromodynamics

The study of the strong nuclear force, which is responsible for binding the quarks together in hadrons, has produced the very successful theory of Quantum Chromodynamics (QCD). This theory is based on a Lagrangian describing the interaction of quarks and gluons.

The QCD Lagrangian is not always solvable and approximations and numerical calculations need to be made to extract solutions. At large interaction energies[1], the strong force becomes weaker and the Lagrangian can be perturbatively solved using the strong coupling constant. Comparing these large interaction energy solutions to experimental data have been used to suggest this Lagrangian is correct. As the energy of the interaction decreases to the energies characteristic of the proton, perturbation in this manner is no longer useful.

Numerical solutions of the QCD Lagrangian seem to be the most promising way to get solutions which can be compared to experiment. Currently, attempts to solve the QCD Lagrangian on a lattice (Lattice QCD) are ongoing. The continuous space-time of the real world are discretized to a lattice and computational techniques are applied to extract solutions. Successes have occured in this field such as [2]. However, the full calculation of the spectrum of excited states has yet to be finished.

1.2.2 Constituent Quark Models

In the absence of direct solutions of the QCD Lagrangian, models are developed to get an idea of the dynamics of the internal structure of the nucleon. One of the most successful of these is the constituent quark model.

Constituent Quark Models (CQMs) are based on the nucleon being made of three "valence" quarks. The quarks are dressed with a mass and a potential is proposed. In this simplified environment, the mass of the quarks are dressed with a fitted mass to ensure the mass of the calculated nucleon matches the real world nucleon and an infinite tower of excited states is calculated.

One example of the predictions for isospin $I = 1/2$, non-strange baryons from a Constituent Quark Model is shown in Figure 1.1. This model is a relativistic quark model. Each double column is labeled with the quantum numbers of the states marked with horizontal lines. Each quantum number assignment has two columns. The left column of states are the theoretically predicted states. The right column of states are the experimentally discovered states with the uncertainty of the mass

---

[1]equivalently small distances both compared to nucleon properties
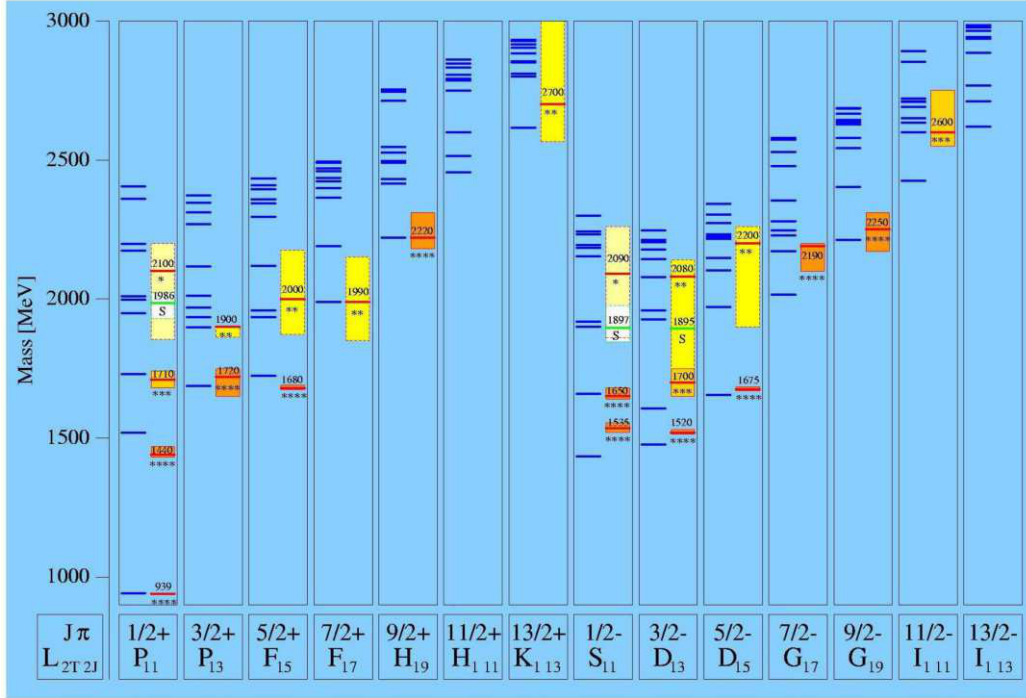
Figure 1.1: Constituent Quark Model Predictions for Isospin 1/2, Non-strange Baryons. Published in [3]. This model is a relativistic quark model. Each double column is labeled with the quantum numbers of the states marked with horizontal lines. Each quantum number assignment has two columns. The left column of states are the theoretically predicted states. The right column of states are the experimentally discovered states with the uncertainty of the mass represented with a colored bar. Each experimentally discovered state is marked with a star assignment from the PDG [1]. **** is a state for which existence is considered certain. * is a state having poor evidence for existence. For this plot only, the baryon quantum numbers are denoted with isospin T, spin J, and L, the relative angular momentum of a πN system which would create the baryon resonance.

represented with a colored bar. Each experimentally discovered state is marked with a star assignment from the PDG [1]. A four-star state is a state for which existence is considered certain and properties are fairly well explored. A three-star state is a state for which existence ranges from likely to certain but further information is desired. A two-star state is a state for which evidence of existence is only fair. A one-star state is a state for which evidence of existence is poor. For this plot only, the baryon quantum numbers are labeled with isospin T, spin J, and L, the relative angular momentum of a πN system which would create the baryon resonance.

These predictions are fairly similar to the other Constituent Quark Models in the agreement with existing experimental data. The agreement is good below about

1800 MeV/c^2 in mass but fails at higher masses. Since some agreement is seen, these models must describe at least some aspects of the system. However, the possible reasons for the discrepancies above 1800 MeV/c^2 are 1) the model is correct but we have not experimentally isolated these higher mass states or 2) the model does not account for some dynamics of the system.

A competing model which predicts fewer states is the diquark model, where the dynamics of a pair of quarks are "frozen". The system is then considered as a two-body system [4]. This model's predictions also match the experimental data below 1800 MeV/c^2 in baryon mass and predict fewer higher mass baryon resonances. However, the number of predicted diquark baryon resonances still outnumbers the experimental states. Unfortunately, there have been no satisfactory modifications to either of these models to successfully predict the current pattern of experimental states.

Experimentally, the isolating of the full spectrum of excited states is a challenging endeavor due to many reasons which will be discussed in the Section 1.3. Because the number of predicted high energy baryons outnumber the experimentally verified states, this discrepancy is called the "Missing Baryon Problem". To understand the nature of the strong interaction in the regime of non-perturbative QCD, the baryon resonances must be fully isolated and characterized.

1.3   Experimental Situation

The search for and study of the excited states of the nucleon is called baryon spectroscopy. The motivation for doing baryon spectroscopy is based on the very successful application of atomic spectroscopy. Atomic spectroscopy led to many discoveries including quantum mechanics and Quantum Electrodynamics (QED) and allowed a very successful description of the electromagnetic force. The plan used in atomic spectroscopy is basically :

- Excite the system.

- Measure the energy of the emissions as the system relaxes.

- Identify the characteristic energy of each excited state.

In measuring the decay products from excited atoms, the only necessary particle to measure is the photon. The photon is a stable particle and the excited states of the atom are relatively long lived[2]. Therefore, the discreteness of the measured energy is, in most cases, only a function of the detector systems, i.e. the natural width of the state is not large compared to the separation of states. To separate the signal from two excited states which are close in energy, only the detector resolution must be improved.

---

[2]compared to baryon excited states

1.3.1 Baryon Spectroscopy

The situation in baryon spectroscopy is much more challenging. The decays from excited baryons can be a zoo of particles which include mesons, photons, leptons and other baryons. Many of these particles are very short lived and decay to other particles which can either be neutral or charged. To detect the different types of particles, different detectors must be employed. At the energies characteristic of low-mass baryon resonance decays, the different detectors can affect the operation of others, if used simultaneously. This forces experiments to focus on subsets of the particles to detect. For instance, the experimental setup used in this thesis, the CBELSA/TAPS experiment, can detect the energy and position of photons in the final state but only the presence of charged particles. All other information, such as momentum, charge, and mass, on the charged particles in the final state must be deduced.

Another issue complicating the isolation of excited states of the baryon is that these excited baryons have extremely short lifetimes ($\sim 10^{-23}$ s), which according to the Heisenberg Uncertainty Principle, means the mass of the baryon when measured has a natural width on the order of 100 MeV/c^2. These natural widths, in many cases, are at least as big as the separation of these states from each other. The challenging part is to isolate these states which overlap and interfere with each other. In Figure 1.1 where the excited states are predicted to be close together in mass (above 1800 MeV/c^2), the absence of experimentally discovered states could be due to this overlapping issue.

The first baryon spectroscopy experiments were performed by exciting the nucleons with pions (low mass mesons). These experiments led to the largest share of the excited baryon discoveries currently known. However, some studies suggest some of these missing states do not couple to pions. Work done by Koniuk and Isgur [5] and later by Capstick and Roberts [6, 7, 8] shows many of the "missing" baryons have weak $N\pi$ couplings but have strong $N\gamma$, $N\omega$ and $N\eta$ couplings.

Currently, many experiments are trying to excite nucleons with photons. By analyzing data coming from photoproduction[3] experiments, the baryons missed via pion excitation could be isolated. Laboratories like Jefferson Lab (JLab), ELSA, MAMI, GRAAL, and SPring-8 have had experiments exploring these photoproduction reactions.

1.4 Finding Baryons Contributing to Experimentally Measured Observables

When searching for evidence for baryon resonances, experimentalists can usually first start looking for their signatures in unpolarized scattering cross sections. A cross section is proportional to the probability of a particular reaction happening (see

---

[3]producing particles from a photon
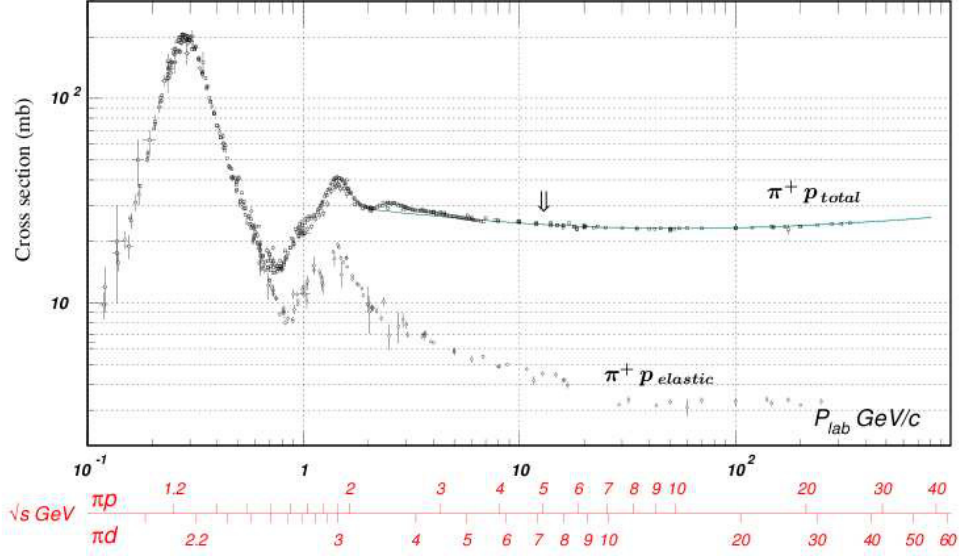
Figure 1.2: Total and Elastic Cross Sections for the Scattering of π^+ Mesons off of Protons. The peak at center-of-mass energy ($\sqrt{s} = 1.232$ GeV) is the ground state Δ baryon resonance, $\Delta(1232)\frac{3}{2}^+$. Courtesy of the COMPAS group, IHEP, Protvino.

Section 1.4.1). A baryon resonance when produced directly from the initial particles will produce, in the absence of any interfering processes, an increase (a peak) in the cross section. Figure 1.2 shows the total and elastic cross sections from π^+ mesons scattering off of protons and shows the cross section peak (largest and lowest energy peak) corresponding to the $\Delta^{++}(1232)\frac{3}{2}^+$ baryon resonance. However, as the energy increases past the first peak, fewer and smaller peaks are seen. This gradual disappearance of peaks suggests the resonance widths are becoming large and the resonance contributions are overlapping and interfering with each other. In fact, the smaller peaks in Figure 1.2 could be a result of a combination of several resonances [9]. In order to disentangle these resonance states at higher energies, more information and more sophisticated techniques are needed.

1.4.1 Observables

Differential Cross Sections. A differential cross section is the probability that a certain reaction happens when its final state particles scatter into some final state kinematics. For the purposes of an experimental measurement, this means the number of reactions (N_{scat}) which scattered into some final state kinematics divided by the total number of opportunities for the reaction to happen. The differential cross section is a function of the reaction's final particle kinematic variables X_i. When no preferred polarization is produced, the cross section is called an unpolarized differential cross

8

section. As a beam of photons is scattered off of a stationary target of protons, the total number of opportunities for the reaction to happen is equal to the product of the total number of photons traversing the target during data taking (Photon Flux $\mathcal{F}$) and the density of protons in the target per unit area perpendicular to the beam (target area density ρ_t^A). Therefore, a differential cross section for photons scattering off of a target of stationary protons is measured by the formula (independent of any experiment specific issues)

$$\frac{d\sigma}{dX_i} = \frac{N_{scat}}{\mathcal{F}\,\rho_t^A\,\Delta X_i} \quad . \tag{1.3}$$

Total Cross Sections. A total cross section is the total probability that a certain reaction happens at some energy. To get to a total cross section from the differential cross section, the differential cross section is integrated over the final state kinematic variables.

Polarization Observables. When spin polarizations are measured, polarization observables are possible and are quantities which quantify how the differential cross section depends on the spin polarization of the initial or final state particles. These quantities can be used to separate the contribution from baryon resonances with different spin and parity.

One example of a polarization observable, which is used in this thesis, is the spin-density matrix. When analyzing reactions with a decaying particle with spin larger than zero, the probability that a particle is produced with a certain spin polarization is detectable in the decay distribution of its decay products. For example, two ω mesons with different spin polarizations will eject the same decay products in different directions. By analyzing the angular distribution of the decay photon in the $\omega \rightarrow \pi^0\gamma$ decay, the relative probability that each ω spin polarization is produced can be extracted.

The spin projection of the ω meson is measured in a reference system. The popular systems to choose are [10]

- Helicity system - z-axis is chosen to be in the same direction as the ω meson in the overall center-of-mass frame,

- Adair system - z-axis is chosen to be in the same direction as the initial photon in the overall center-of-mass frame, and

- Gottfried-Jackson system - z-axis is chosen to be in the same direction as the initial photon in the rest frame of the ω meson.

In each system, the y-axis is defined to be $\hat{k} \times \hat{q}$, where $\hat{k}$ is a unit vector in the direction of the initial photon in the center-of-mass frame, $\hat{q}$ is a unit vector in the direction of travel of the ω meson in the center-of-mass frame and $\times$ is the vector cross product. The x-axis is defined by $\hat{y} \times \hat{z}$.

1.4.2 Interpretation

In order to find the contribution of all the baryon resonances contributing to a final state, the observables must be interpreted by modeling the effect of every possible contributing process (e.g. baryon resonance production, meson exchange, baryon exchange). These individual processes can be modeled and combined at varying strengths to fit to the measured observables.

To model each of these processes, the matrix element ($\mathcal{M}$) is derived by mathematically modeling each process and combining them using constants which define the probability each process occurs. The expression for each process is defined by the spin polarization of each of the initial and final state particles. The differential cross section defined in terms of these matrix elements is [1]

$$d\sigma = \frac{(2\pi)^4}{4\sqrt{(p_1 \cdot p_2) - m_1^2 m_2^2}} \frac{1}{N_{initial\ spins}} \sum_{spins} |\mathcal{M}|^2 \delta^4\left(P - \sum_{i=1}^{n} p_i\right) \prod_{i=1}^{n} \frac{d^3 p_i}{(2\pi)^3 2E_i} \quad , \quad (1.4)$$

where the subscripts 1 and 2 are the index of the initial particles and the subscript i is the index of the n final state particles, p_i is the momentum, m_i is the mass, P is the total initial momentum, E_i is the energy, and $N_{initial\ spins}$ is the number of possible spin polarizations of the initial particles.

Several schemes for defining the matrix elements exist. The most widely used of these is the partial wave analysis (PWA). The partial wave analysis is a method by which each matrix element is constructed as a sum over the angular momentum states. Since the relative strengths of these different angular momentum states are defined by the angular distribution of the observable values, the full angular distribution of an observable must be well measured to do a proper partial wave analysis.

The contributions of the baryon resonances are modeled in partial wave analyses as Breit-Wigner functions. These functions have a dependence on energy resembling the $\Delta(1232)\frac{3}{2}^+$ peak in Figure 1.2. Since most known baryon resonances have widths of around 100 MeV, the mass resolution of observable measurements must be of at least 100 MeV in order to resolve baryon resonances.

Therefore, a differential cross section measurement which would have the best chance of allowing a proper partial wave analysis solution is one which has full angular coverage and has enough statistics to provide data points dense enough to resolve baryon resonances.

The spin-density matrix elements (SDMEs) will also help in fixing the strengths of processes by fixing the relative contributions of processes which result in different ω meson spin polarizations. In terms of the matrix element, the SDME (ρ_{ij}) is

$$\rho_{ij} \sim M_i M_j^* \quad , \tag{1.5}$$

where the $*$ denotes complex conjugation, and i and j are the index of the spin polarization of the ω meson. The spin-density matrix elements and other polarization observables will help define the relative strengths of these matrix elements.

1.5 Finding the "Missing" Baryons

The experimental plan for finding these elusive "missing" baryon states involves a multi-pronged approach. With an eye for what has been done in the past, the plan entails:

- Photon beams - Use photons as the particle to excite nucleons. The photon does not interact with the nucleon via the strong force, therefore does not have the same coupling issues. The resulting excited states should not be restricted.

- Full kinematic variable measurement of observables - To separate processes with different angular distributions, the full angular range should be measured with good angular resolution.

- Small energy resolution - Since baryon resonances typically have mass widths of around 100 MeV, the measured observables should have an energy resolution of at least this order to separate the contributions from neighboring states.

- Multi-particle final states - Some of these missing baryons could possibly not couple to photons either. Therefore, these states could show up in an intermediate decay when measuring a reaction with 3 or more final state particles. (e.g. $\gamma p \rightarrow N^* \omega \rightarrow p \pi^0 \omega$, where the N^* is a baryon resonance).

- Polarization Observables/ Spin-Density Matrix Elements - Processes couple to different initial and final state particles with different spin polarizations at different strengths. Using polarization observables along with the unpolarized differential cross sections in an interpretation analysis, more information is available to separate the different processes and to obtain the correct strength for each baryon resonance contribution.

1.6 Motivation

A prediction on baryon resonances decaying to one proton and one ω meson published in [7] has shown non-negligible couplings for 32 states with masses below 2.3 GeV/c^2, the range of sensitivity for the data in this analysis. Currently in The Review of Particle Physics (RPP) published by the PDG [1], only 14 states are listed in this same mass range with at least very likely evidence for existence (3- or 4- star status). By studying the $\gamma p \rightarrow p\omega$ and $\gamma p \rightarrow p\pi^0\omega$ reactions, the existence of more of these states can be proven and help give vital information on the pattern of excited baryon resonances.

An additional benefit of studying baryon resonances decaying to ω mesons is any baryon decaying to an ω meson and a baryon must have the same isospin as the decay baryon. When a hadron decays to hadrons, the mediating interaction is the strong force. Since the strong force conserves total isospin, a baryon which decays to an

isospin scalar ($I = 0$) ω meson and an isospin I baryon then the baryon itself can only have isospin I. For this reason in hadron spectroscopy, the final state with one proton and one isospin scalar mesons, such as the ω meson, is often called an isospin filter.

1.6.1 $\gamma p \rightarrow p\omega$

The contributions of the "missing" baryon resonances to the $\gamma p \rightarrow p\omega$ reaction could be potentially masked by the π^0 exchange process reported in [11] and shown in Figure 1.3b (with the ? $= \pi^0$). The difficulty in isolating these baryon resonances is to obtain enough information to subtract the contributions from the dominant π^0 exchange (also called t-channel).

(a) Resonance   (b) Meson Exchange   (c) Baryon Exchange
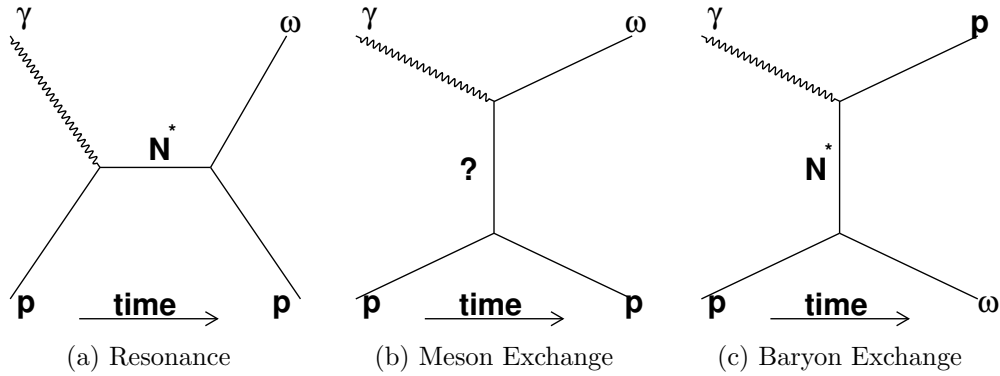
Figure 1.3: Diagrams for Single ω Photoproduction.   The initial particles, photon (γ) and proton (p), are on the left side of each diagram. The final state particles (p, ω) are shown on the right side of each diagram. The N^* represents any baryon or baryon resonance. The ? represent mesons which have integer spin (S = 0,1,2,...).

Several different baryon resonance contributions have been used to explain the behavior of the $\gamma p \rightarrow p\omega$ differential cross sections. A coupled-channel effective Lagrangian analysis performed by the Gießen group was published in 2005 [12]. This analysis included baryon resonances with spin up to 5/2 and was based on available data from πN scattering and γN scattering from the final states πN, $2\pi N$, ηN and ωN. Data with an initial photon energy range from the pion production threshold up to 2 GeV were analyzed. The results of this analysis indicated that two sub-threshold resonances, N(1675)$\frac{5}{2}^-$ and N((1680)$\frac{5}{2}^+$, were responsible for a resonance peak close to threshold, while showing large t-channel contributions as energy increased.

A partial wave analysis based only on the data measured at the CLAS experiment (Section 2.1.3) was published in [13] and indicated the N(1700)$\frac{3}{2}^+$ and N(1680)$\frac{5}{2}^+$ baryon resonances were responsible for the resonance peak near threshold. At energies above 2 GeV in initial photon energies, the PWA analysis on the CLAS results required additional resonances, two spin 5/2 resonances and one 7/2 resonance, to

describe the cross sections. The 7/2 state is the N(2190)$\frac{7}{2}^-$ which has a 4-star status in the RPP [1]. The N(1680)$\frac{5}{2}^+$ and N(2000)$\frac{5}{2}^+$, a 4-star and 2-star state, respectively, were the claimed 5/2 states. To uniquely isolate these resonances, the full angular differential cross sections and polarization observables need to be used in a coupled-channel analysis.

Unfortunately, as can be seen in Section 2.1, the existing data sets have angular or bin size limitations which could affect these solutions. The most critical angular range to use for getting information about the strength of the π^0 exchange is the very forward direction, where the ω meson is close to the exiting beamline. In the previous measurements at the CLAS [14] and SAPHIR [15] experiments, the ω meson was detected in its $\pi^+\pi^-\pi^0$ decay by detecting the charged pions. Unfortunately, the charged pions have masses and charges which can be very difficult to separate from the electron positron pair production naturally occurring close to the beamline. However, the CBELSA/TAPS experiment has the capability to measure the $\pi^0\gamma \to \gamma\gamma\gamma$ decay of the ω meson. The photon is both massless and uncharged and is much easier to separate from electrons and positrons. Using this decay mode, the CBELSA/TAPS experiment can measure the full angular range while isolating enough of these events to allow mass resolution on the order of the typical baryon resonance width in this angular range.

The spin-density matrix elements for the $\gamma p \to p\omega$ reaction are polarization observables which will allow the separation of processes which produce ω mesons with different spin polarizations. For instance, baryon resonances with different spin polarizations would produce different ω spin polarizations. Also, the π^0 (spin = 0, parity = −1) exchange diagrams (Figure 1.3b) would produce a different ω spin polarization than the exchange of some other particle with different spin and parity from the same photon polarization.

1.6.2 $\gamma p \to p\pi^0\omega$

The $\gamma p \to p\pi^0\omega$ reaction provides many opportunities to observe baryon resonances. Some of the possible processes are shown in Figure 1.4. All but one of these diagrams have the possibility to involve baryon resonances. In diagrams a,b,d, and e, there is an opportunity to observe baryon resonances decaying to $p\pi^0$ and $p\omega$. However, the difference in detecting them in $\gamma p \to p\pi^0$ and $\gamma p \to p\omega$ reactions is the ability to observe them independent of the γp coupling. Therefore, the different production could enable us to see the previously "missing" baryon resonances if they did not couple directly to γp production. In diagram c, the observation of new baryon resonances decaying to a new set of mesons could happen. The $b_1(1235)$ meson, which is a spin 1 meson with positive parity with 1229 MeV/c^2 mass, has a very strong decay to the $\pi^0\omega$ final state. Therefore, this is the first chance to observe baryon resonances decaying to $p\, b_1(1235)$. Since the previous data on the $\gamma p \to p\pi^0\omega$ channel is quite limited [16] (dicussed further in Section 2.2), the analysis presented in this work will

provide the first chance to isolate any of the "missing" baryon resonances contributing to this final state.

The previous analysis of this reaction was of poor statistics but was useful in determining the most dominant process which contributed to this final state. The dominant process was determined to be the meson exchange process in Figure 1.4d with the π^0 meson as the exchange particle and $\Delta(1232)\frac{3}{2}^+$ as the baryon resonance. However, there is likely some resonance production of the $\omega\Delta(1232)\frac{3}{2}^+$ intermediate state as well, like in Figure 1.4b with N_2^* as the $\Delta(1232)\frac{3}{2}^+$ resonance. The N_1^* resonance in this diagram is restricted to a few possibilities due to the isospin filtering effect of the ω meson, spin dynamics, and the available energy. Since there is not much energy available when producing an intermediate state close to threshold, the orbital angular momentum is restricted to small values, $L = 0$. If we consider the combination of a spin $\frac{3}{2}^+$ $\Delta(1232)\frac{3}{2}^+$ resonance combined with a spin 1^- ω meson at orbital angular momentum $L = 0$, then the only resonance spin-parities which can contribute are $\frac{5}{2}^-$, $\frac{3}{2}^-$, and $\frac{1}{2}^-$. Using the isospin property of the ω meson, the N_1^* resonance in this diagram must have isospin $I = 3/2$ and is a Δ resonance. Therefore, we are restricted to five resonances which are listed in the RPP [1]. These are $\Delta(1620)\frac{1}{2}^-$(3 stars), $\Delta(1700)\frac{3}{2}^-$(4 stars), $\Delta(1900)\frac{1}{2}^-$(2 stars), $\Delta(1930)\frac{5}{2}^-$(2 stars), and $\Delta(1940)\frac{3}{2}^-$(2 stars). To disentangle the contributions of these resonances from the dominant contributions requires a full partial wave analysis with each process defined over an observable measurement which has the energy binning and kinematic coverage to isolate the non-dominant contributions. The measurement in this thesis offers the first measurement capable of increasing the evidence for existence for any of these states through this channel and could lead to an upgrade of star assignment.

Recently, there has been interest in the reconstruction of exotic mesons, specifically the $\pi_1(1600)$, from the $\pi b_1(1235)$ decay. The $\pi_1(1600)$ meson has measured quantum numbers which are not represented by constructing mesons from a quark anti-quark system and therefore called exotic. To study this meson, the meson must be reconstructed by combining all $\pi b_1(1235)$ combinations of which the exotic meson will be only a small fraction. However, another contribution which could be at the same strength or larger is the contributions of the $\Delta(1232)\frac{3}{2}^+ b_1(1235)$ decaying to $p\pi b_1(1235)$. The information gathered from this analysis on the production of $b_1(1235)$ mesons off the proton could be used to help define the strength of $\Delta(1232)\frac{3}{2}^+ b_1(1235)$. If the meson is produced via π^0 meson exchange, the strength can be well determined.

(a) Resonance 1   (b) Resonance 2   (c) Resonance 3

(d) Meson Exchange 1   (e) Meson Exchange 2   (f) Meson Exchange 3

(g) Baryon Exchange 1   (h) Baryon Exchange 2   (i) Baryon Exchange 3
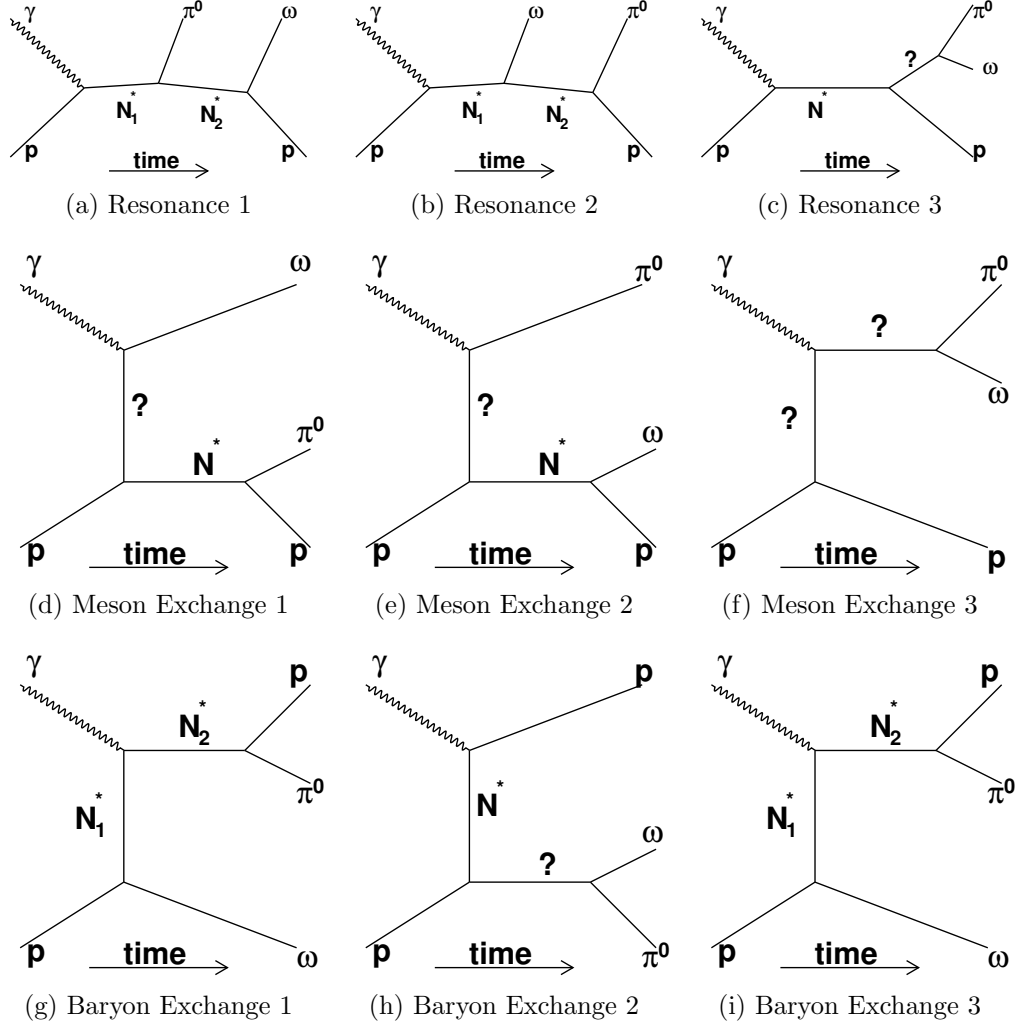
Figure 1.4: Diagrams for $\pi^0\omega$ Photoproduction. The initial particles, photon (γ) and proton (p), are on the left side of each diagram. The final state particles (p, π^0, ω) are shown on the right side of each diagram. The ? are mesons which have integer spin. N^*, N_1^* and N_2^* represents any baryon or baryon resonance. This list is not exhaustive and are the processes featuring only the three-particle vertex. Each exchange diagram is named by what is being exchanged in the vertical.

15

CHAPTER 2

PREVIOUS MEASUREMENTS

The measurements in this section will be presented as a function of $\cos\theta^{\omega}_{c.m.}$ and initial photon energy E_γ. $\cos\theta^{\omega}_{c.m.}$ is the cosine of the polar angle measured in the center-of-mass frame with respect to the direction of travel of the initial photon (Figure 2.1). E_γ is the energy of the initial photon measured in the lab frame.

2.1 $\quad \gamma p \rightarrow p\omega$

The differential cross sections for the reaction $\gamma p \rightarrow p\omega$ have been measured three times with initial photon energies from threshold (≈ 1.11 GeV) up to 2.5 GeV. The unpolarized spin-density matrix elements have been measured twice. These measurements, however, are without the angular coverage and mass resolution ideal for isolating baryon resonances from the background. The need for a new measurement over the full angular range is motivated by the dominance of the π^0 meson exchange and obtaining enough information to separate this effect from the contributing "missing" baryon resonances.

2.1.1 SAPHIR 2003

The first measurement in this energy range with characteristics useable to disentangle "missing" baryon resonances was published by the SAPHIR collaboration in 2003 [15]. The SAPHIR experiment used a spectrometer which covered approximately 60% of the full angular range and was fed tagged bremsstrahlung photons produced by colliding ELSA accelerator electrons into a radiator. The ω meson was measured by detecting the $\omega \rightarrow \pi^+\pi^-\pi^0$ decay.

Figure 2.2 shows the differential cross sections (▲) published in [15]. The SAPHIR experiment used a tagged photon beam incident on a liquid hydrogen target. The charged particles were detected in the spectrometers. The π^0 meson was reconstructed using missing mass. The low energy data shows a relatively constant angular distribution indicating baryon resonance production. The high energy data show that the differential cross sections peak in forward direction, which suggests meson exchange.

16
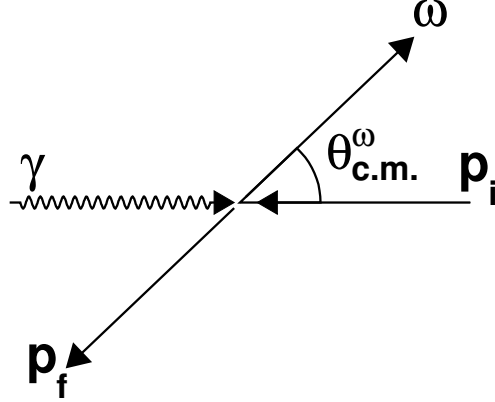
Figure 2.1: Single ω Photoproduction Kinematics Diagram. The initial and final state particles are shown in the center-of-mass frame. The γ is the photon. The p_i is the inital state proton. The ω is the final state meson. The p_f is the final state proton. The angle $\theta^{\omega}_{c.m.}$ is the angle between momentum direction on the initial photon and the final state ω meson.

The differential cross sections were measured generally between -0.9 and 0.967 in $\cos\theta^{\omega}_{c.m.}$ and in 23 energy bins between threshold and 2.6 GeV in initial photon energy. The angular bins in the low energy region are quite large and are not ideal for an interpretation analysis.

Unpolarized spin-density matrix elements for this experiment were extracted in the helicity and Gottfried-Jackson frames by fitting the decay angular distrbutions. Spin-density matrix elements measured in the helicity frame are shown in Figure 2.3.

The spin-density matrix elements have 2 angular bins and 4 energy bins. These measurements are a good first look at the values but again are not ideal for an interpretation analysis.

2.1.2 LEPS 2006

The LEPS collaboration published differential cross sections for the photoproduction of ω mesons in 8 energy bins in initial photon energies from 1.6 to 2.4 GeV [17]. The differential cross sections were measured in one angular bin when the ω meson travels in an angular range $-0.8 < \cos\theta^{\omega}_{c.m.} < -0.7$.

Figure 2.4 shows the differential cross sections reported by the LEPS collaboration. These data points were extracted using backward-Compton scattering of laser photons with 8 GeV electrons interacting with a stationary liquid hydrogen target. The proton was detected in a spectrometer and the ω meson was reconstructed using missing

17
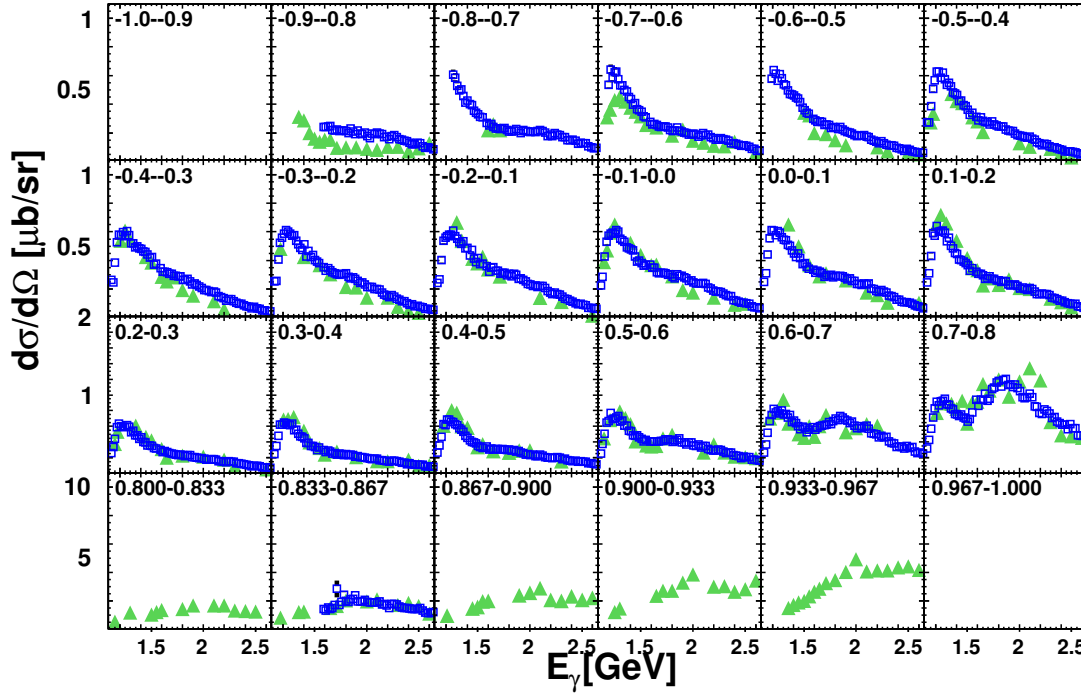
Figure 2.2: SAPHIR and CLAS Excitation Functions. Differential cross sections published by the SAPHIR Collaboration [15] (▲) and the CLAS collaboration [14] (□). Each histogram is labeled with its range in cosine of the polar angle of the ω meson in the center-of-mass frame ($\cos \theta^{\omega}_{c.m.}$). The $\cos \theta^{\omega}_{c.m.}$ value for each point is the center of the bin converted from the original data plot.

mass. The angular range of these data is restricted and by themselves the data are not sufficient for isolating baryon resonances.

2.1.3 CLAS 2009

The CLAS collaboration published differential cross sections at center-of-mass energies from threshold up to 2.4 GeV. These data were produced by scattering tagged photons off of stationary liquid hydrogen. The decay products were detected in a spectrometer which detected the charged pions coming from the $\omega \rightarrow \pi^+\pi^-\pi^0$ decays. The π^0 meson was reconstructed using missing mass.

Figure 2.2 shows the differential cross sections (□) reported by the CLAS collaboration in [14]. The data show 109 10-MeV wide bins measured in center-of-mass energy and 20 angular bins. The energy resolution in this data set is excellent but the angular coverage is not complete in the forward ($\cos \theta^{c.m.}_{\omega} \approx 1$) and backward ($\cos \theta^{c.m.}_{\omega} \approx -1$) regions.

18
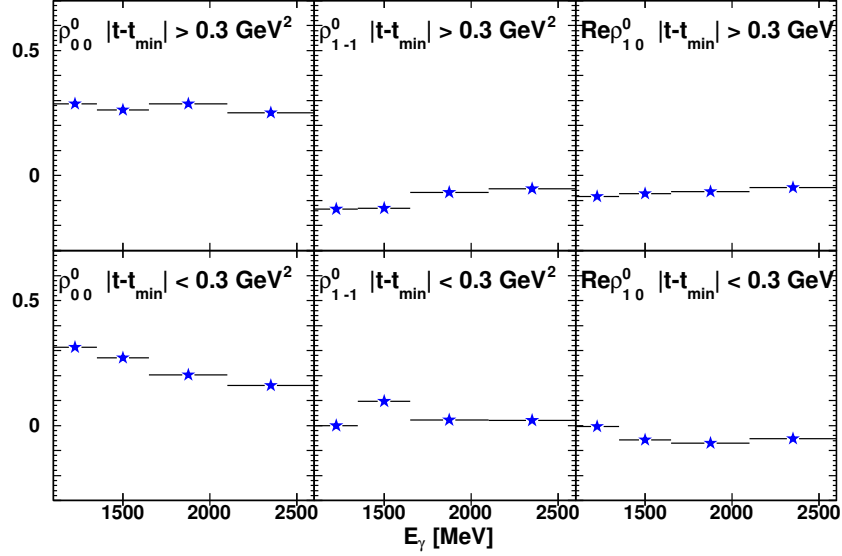
Figure 2.3: SAPHIR 2003 Spin-density Matrix Elements Measured in the Helicity Frame. (defined in Section 1.4.1) Published by the SAPHIR Collaboration [15]. Each histogram is labeled with its range in the mandelstam t variable which is inversely proportional to $\cos\theta^\omega_{c.m.}$. The lowest energy data point in the plots on the top row was measured in the range $|t - t_{min}| > 0.2$ GeV^2. The lowest energy data point in the plots on the bottom row was measured in the range $|t - t_{min}| < 0.2$ GeV^2.

The unpolarized spin-density matrix elements (SDMEs) defined in the Adair frame (defined in Section 1.4.1) were also published using the CLAS data. The SDMEs are shown in Figure 2.5. These data have the same binning as the differential cross section data. These SDMEs were extracted by modeling all s-channel processes of the form $\gamma p \to J^p \to p\omega \to p\pi^+\pi^-\pi^0$ in a partial wave analysis fit. The J is the total spin of the amplitude and p is the parity. All s-channel waves with $J \leq 21/2$ with both parities were used in the fit. From this fit, the SDMEs were extracted.

Again, these data have excellent mass resolution but do not have full angular coverage. These observables are only measured down to approximately 23° in $\theta^\omega_{c.m.}$. As can be seen in the differential cross sections which will be presented in this thesis, there is a characteristic forward peak which can be seen and used to characterize the t-channel meson exchange contribution. This forward peak can not be fully measured with this data.

2.1.4 Differential Cross Section Discrepancies

The SAPHIR collaboration differential cross sections (▲) and CLAS differential cross sections (□) shown in Figure 2.2 show some differences. When comparing the data in the backward angular region ($\cos\theta^\omega_{c.m.} < -0.5$), a discrepancy in the value of
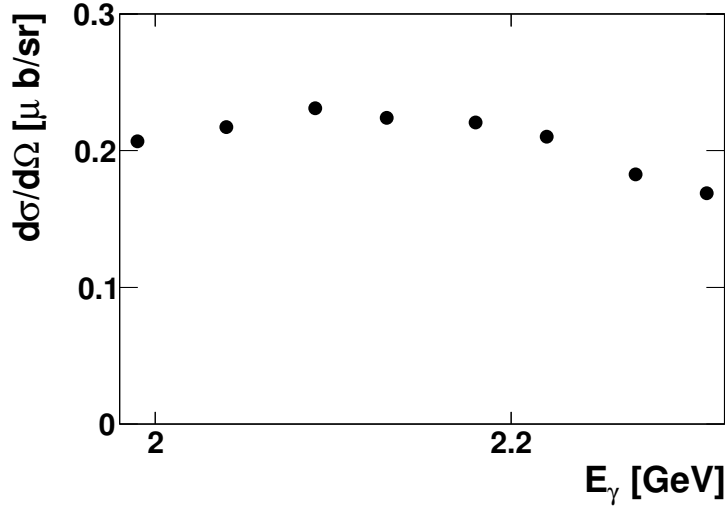
Figure 2.4: LEPS Excitation Function. Differential cross sections published by the LEPS collaboration [17] in 2009. This data represents $0.7 < \cos\theta^\omega_{c.m.} < 0.8$. The errors are not shown.

the differential cross sections can be seen. Since the angular distribution has a large impact on the results of an interpretation analysis, the question arises about which data set is correct and which one has problems. A new measurement in this kinematic region would help in resolving this issue. The analysis in this thesis will provide this new measurement.

2.2 $\gamma p \to p\pi^0\omega$

The only previous measurements of the reaction $\gamma p \to p\pi^0\omega$ was done by an earlier iteration of the CBELSA/TAPS experiment called the CB-ELSA experiment in [16].

Figure 2.6 shows the resultant data from the CB-ELSA experiment and were measured from approximately 2000 reconstructed $p\pi^0\omega$ events. The most noticeable feature is the rise in cross sections at the forward angles. This type of rise is associated with a meson exchange process of the type
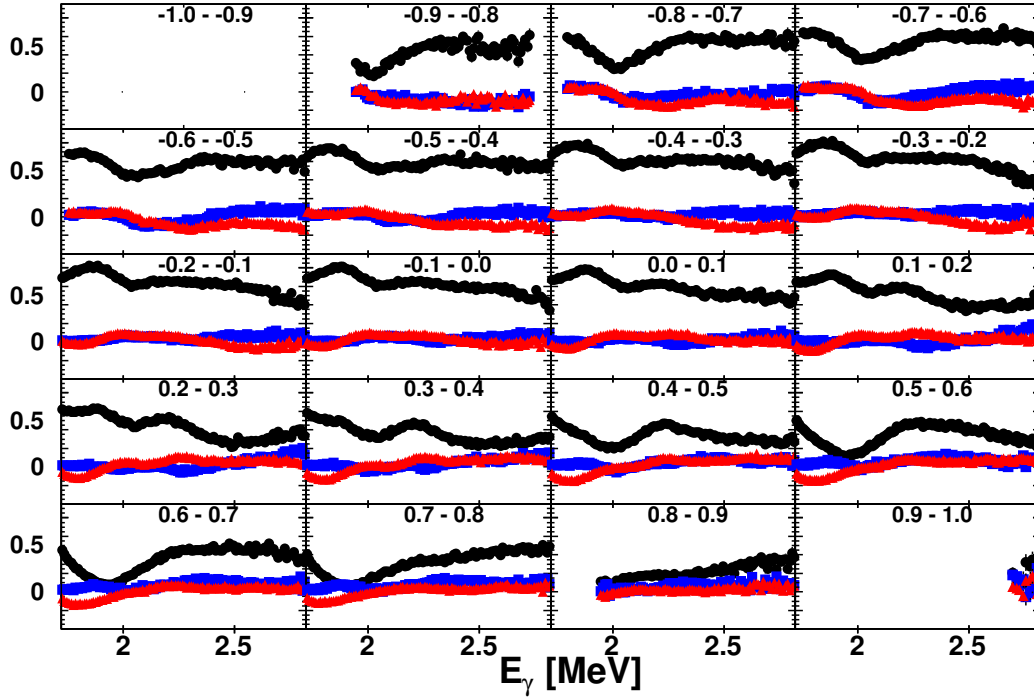
Figure 2.5: CLAS 2009 Unpolarized Spin-density Matrix Elements Measured in the Adair Frame. (defined in Section 1.4.1) Published by the CLAS Collaboration [14]. Each histogram is labeled with its range in cosine of the polar angle of the ω meson in the center-of-mass frame ($\cos\theta_\omega^{c.m.}$). ρ_{00}^0 ($\bullet$), ρ_{1-1}^0 ($\blacksquare$), and $Re\rho_{01}^0$ ($\blacktriangle$) are shown.
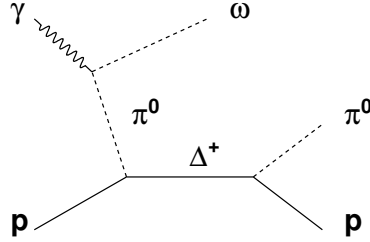
The Δ^+ is named because the most likely resonance is the $\Delta(1232)\frac{3}{2}^+$, a well established baryon resonance (4-star state). Beyond this dominant process, there could be "missing" baryon resonance contributions which contribute but can only be isolated through an interpretation analysis.

While this measurement is useful in revealing the main features of the reaction, this data is not as useful in finding new baryon resonances. This measurement is not sufficient for an interpretation analysis due to the sparse nature of the data points. The data presented in this thesis has an order of magnitude more events while enabling

21

a more complete acceptance correction. This new data will enable an interpretation analysis which will explore the contributions of "missing" baryon resonances.
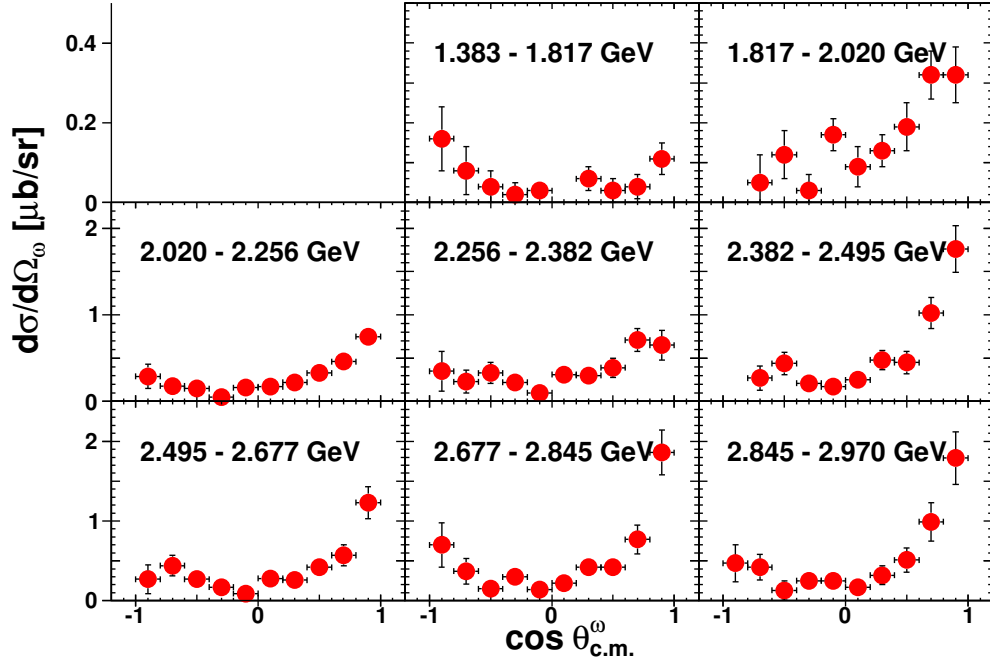
Figure 2.6: CB-ELSA $\gamma p \rightarrow p\pi^0\omega$ Differential Cross Section. Published in [16]. Each histogram is labeled with its range in initial photon energy. The errors presented are only statistical errors.

CHAPTER 3

CBELSA/TAPS EXPERIMENT

The CBELSA/TAPS experiment in its 2002-2003 configuration was located on the campus of the University of Bonn, in Bonn, Germany. The detector systems are centered around the Crystal Barrel detector, which was previously used in the CB-ELSA experiment in the same location and also at CERN at LEAR (Low Energy Antiproton Ring). The Crystal Barrel is a calorimeter designed to provide excellent photon energy detection efficiencies while offering good granularization in reconstructing photon positions.

Using the Crystal Barrel detector, this experiment offers an excellent tool for studying hadronic reactions which eventually will decay to photons. Since many neutral mesons decay this way at least some of the time, this means any reaction which exclusively produces neutral mesons will be available to be studied.
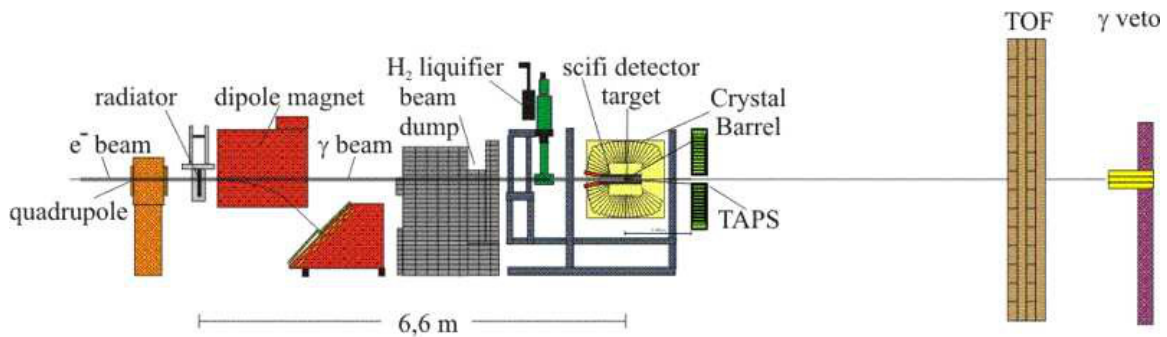
Figure 3.1: CBELSA/TAPS Experimental Setup (2002-2003).

The general setup is shown in Figure 3.1. Accelerated electrons (coming in from the left in Figure 3.1) from the ELSA accelerator (See Section 3.1) are incident upon a radiator, which produces photons via bremstrahlung reactions. The bremstrahlung electron was deflected by the Tagger (See Section 3.3) and the photon continued to the center of the Crystal Barrel detector and interacted with the liquid hydrogen target. The resultant particles were detected in the detector systems (See Section 3.5). Any bremstrahlung photons which did not interact with the target continued

downstream and were detected in the γ Veto detector. The γ Veto detector was used to help determine the photon flux used in the cross section determinations. In this analysis, the Time of Flight wall (TOF) was not used and therefore not discussed here.

3.1   ELSA Accelerator

The ELectron Stretcher Accelerator (ELSA) used a system of two sychrotrons and injector LINACs (LINear particle ACcelerators) to accelerate electrons up to 3.5 GeV in energy. This facility has had an accelerator in place since 1953 and in its current configuration of two syncrotrons since 1987 [18].
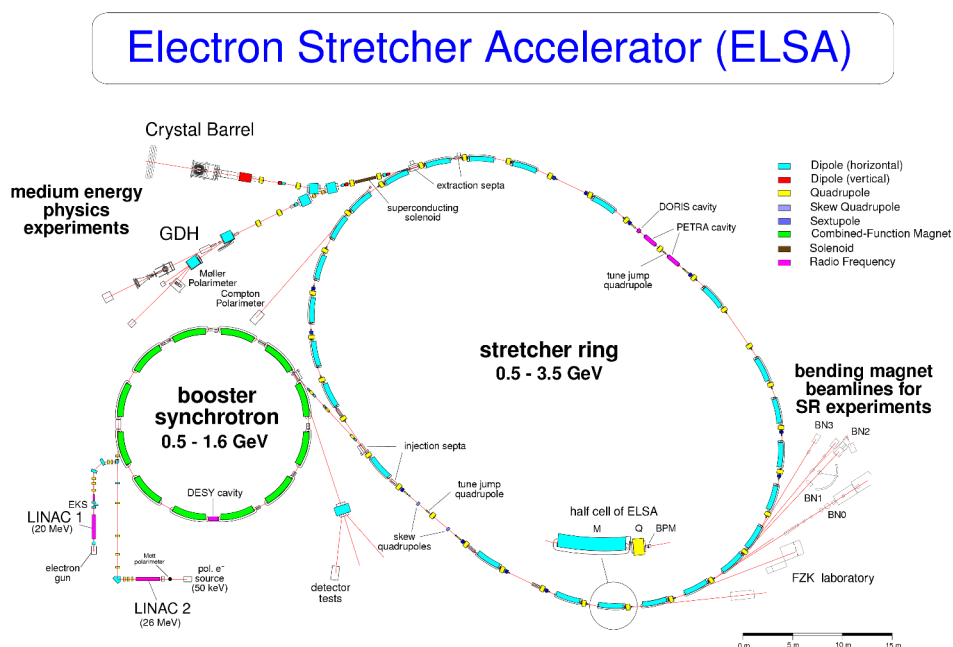
Figure 3.2: ELSA Accelerator Map (2003).

Figure 3.2 is the map of the ELSA facility as of 2003. The accelerator was capable of supplying a quasi-continuous beam of unpolarized electrons at energies up to 3.5 GeV in energy.

Initial electrons were produced at the beginnings at either of the two LINACs. The two different LINAC lines were present in order to produce either polarized or unpolarized electrons.

LINAC 1 was used for the production of unpolarized electrons and used a thermal electron gun. The unpolarized electrons were accelerated and injected into the booster synchrotron. Unpolarized electrons were the only ones used for hadronic studies during the 2002-2003 CBELSA/TAPS experiment.

24

Polarized electrons are produced and accelerated via LINAC 2. Polarized electrons were produced using a 50 keV source which used polarized laser light incident on a Be-InGaAs/Be-AlGaAs supperlattice crystal.

The booster synchrotron was used to accelerate the electrons up to 1.6 GeV and injected them into the stretcher ring. The resultant current from the booster synchrotron was pulsed with a duty factor[1] of around 5%. In order to deliver the continuous beam which hadronic experiments need, this beam needed to be "stretched" out.

When the output energy of the needed electrons was 1.6 GeV or below, the stretcher ring was set into *stretcher mode*. In this mode, the stretcher ring served as a storage ring which stretched out several pulses into an almost continuous beam. The beam was then slowly extracted to the experiment.

When the needed output energy of the electrons is above 1.6 GeV, the accelerator was set into *post-accelerator mode*. In this mode, an extra step involved increasing the energy of the electrons. Several pulses from the booster were collected in the stretcher ring and then accelerated to the desired energy and then stretched out to form a continuous beam. Then the beam was extracted slowly and continuously. This mode resulted in a continuous beam with some dead times for refilling the ring and ramping up the energy. This mode had a macroscopic duty factor up to 95%.

Once the high energy electrons were accelerated to the desired energy and continuously distributed, the beam could either be slowly extracted using an extraction magnet or the beam could be stored in the stretcher ring for several hours. The stored beam could be used to feed experiments using synchrotron radiation.

The electrons for this analysis were extracted over a period of about 10 seconds while maintaining a duty factor of about 80% with a final electron energy of 3.175 GeV.

3.2   Radiator

As the 3.2 GeV electrons came in from the ELSA accelerator, the electrons encountered a radiator. This radiator caused some of the electrons to undergo a bremsstrahlung reaction and lose some of their energy by emitting a photon. The radiator used for all differential cross sections and unpolarized spin-density matrix element measurements was a copper radiator with a thickness of $3/1000$ X_R (radiation lengths). This ensured statistically only one interaction occurs per electron.

For measurements using linearly polarized photons, the goniometer (shown in Figure 3.3) was used to switch to a diamond radiator. The diamond radiator provided a regular lattice for the electrons to scatter from. When scattering occurs at certain angles and momenta, coherent production of photons with polarization vectors parallel to the lattice vectors occur. When the crystal lattice is fixed in space and the energy of the initial electrons is fixed, the preferential production of photons with

---

[1]time with beam/total time
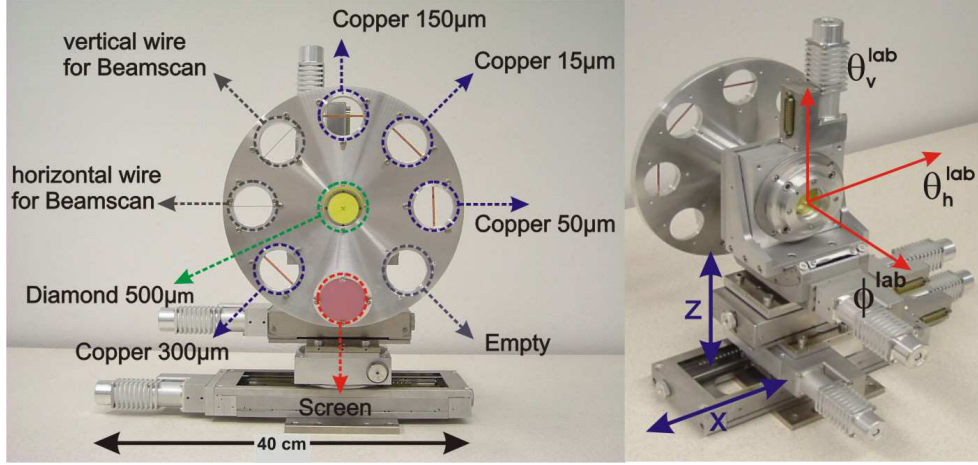
Figure 3.3: Goniometer Schematic. Holds the radiators used to create bremstrahlung reactions, which coverts the ELSA electron beam to a photon beam.

linear polarization occurs at its maximum just below the coherent edge energy. The coherent edge is a discontinuity in the cross section of polarized photons versus energy where above this energy the degree of polarization drops.

A linearly polarized photon beam data run is defined by the position of the coherent edge. Generally, the degree of polarization of the beam above this energy is small.

In this thesis, the data used for the measurement of the differential cross sections and unpolarized spin-density matrix elements was measured using an unpolarized photon beam produced via the copper radiator. All plots of experimental data in this thesis is made using this unpolarized data, unless otherwise noted. Only the polarized spin-density matrix elements were measured using the diamond radiator. Therefore, only data plots in Section 9.3.2 use these polarized data.

3.3   Tagger

The result of the bremstrahlung reaction was a photon traveling along the same direction as the initial electron and an electron of lower energy. Since energy is conserved, the total energy of the initial electron was equal to the combined energy of the photon and final electron. Therefore once the energy of one of the final particles was known, the energies of both final state particles were known. The initial electron's energy was already well defined by the ELSA accelerator.

Since measuring the photon's energy directly would affect its use as an initial particle in the subsequent hadronic reaction, the bremstrahlung electron was focused on as the source of information. To find the energy of this electron, the electron was

subjected to the magnetic field of a dipole magnet. This magnetic field deflected the electron while not affecting the photon. The energy of the bremstrahlung electron is directly related to the magnitude of the deflection of the electron. Since most of the electrons did not interact with the radiator and were unimportant to our analysis, most of the electrons are directed into a beam dump. The rest of the electrons traveled into an array of scintillating bars and fibers, which recorded the passage of charged particles. These scintillators recorded the timing of each electron as it passed by, which in turn fixed the energy and timing of each photon passing into the liquid hydrogen target (after the energy calibration).

The dipole magnet and scintillating fibers and bars are collectively called the Tagging Hodoscope (Tagger) (Figure 3.4). Its function was to "tag" each incoming photon with energy and timing information. The tagger magnet was a 1.63 T dipole magnet which deflected the unscattered electrons 7.5° into a beam dump. Since a scattered electron had less energy than an unscattered electron, the scattered electrons were deflected farther and passed through the electron detection assembly.
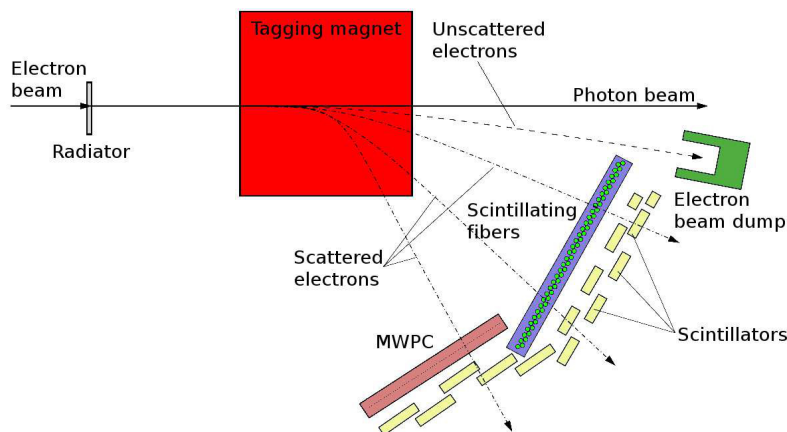
Figure 3.4: CBELSA/TAPS Tagging Hodoscope (Tagger).

The setup to detect the scattered electrons were divided into regions. The high energy region was used to detect electrons which had energies from 80% to 92% of the initial electron beam energy. This region used a Multi-Wire Proportional Chamber (MWPC). The lower energy region detected electrons which had 22% to 80% of the initial electron beam energy. This region used 480 plastic scintillating fibers to detect electrons. Covering both regions, 14 partially overlapping scintillating bars were used in coincidence. The Multi-Wire Proportional Chamber was not used in this work due to the lack of timing information available from this detector.

The scintillating fibers were grouped into bunches of 16 and read out by a photomultiplier tube. The fibers were arranged in 2 overlapping layers and were used in coincidence with its neighboring scintillating bar to detect the presence of an electron

scattered from the beam. Each scintillating bar was read out by two photomultiplier tubes attached to each end.

3.4   Target

Located at the geometrical center of the Crystal Barrel Detector, the target cell was a 5.275 cm long, 3 cm diameter cylinder. The target walls were made of 125 μm thick kapton on the sides and 80 μm thick kapton on the ends. The low density kapton has a very long radiation length (28.6 cm) which decreased the chance of interaction with the photons emitted from the hadronic reactions of interest. The kapton on the sides was also covered by a 1 mm thick aluminum beam pipe for stability.

The target material itself included either liquid hydrogen, liquid deuterium, carbon, calcium, niobium, or lead. For this analysis, only liquid hydrogen was used. The liquid hydrogen provided the unbound, low momentum protons needed to measure photoproduction cross sections off the free proton.

3.5   Detector System

The detector systems for this experiment were designed to provide excellent photon energy and position reconstruction, while registering the presence of charged particles as they passed through the calorimeters. Since the final states for the reactions $\gamma p \rightarrow p\omega$ and $\gamma p \rightarrow p\pi^0\omega$ always included at least one charged particle (proton), the information for charged particles must be treated differently than for photons.

3.5.1   Crystal Barrel Detector

The Crystal Barrel Detector is shown in Figure 3.5 and was constructed of 1290 CsI(Tl) crystals. Each crystal had the long axis pointed towards the target center and was read out by a photodiode. This detector covered the whole azimuthal range and from 30° to 168° in the polar angle, using the exiting photon beam as the reference axis. The crystals were arranged in 23 rings around the beam axis. Each individual crystal covered a solid angle of $\theta = 6°$ and $\phi = 6°$. Only the last 3 rings in the upstream direction had crystals covering a solid angle of $\theta = 6°$ and $\phi = 12°$. The properties for the CsI crystals are listed in Table 3.1.

When a high-energy photon entered the CsI crystal, the photon's energy was deposited via electromagnetic showers. The size of a shower depends on the properties of the crystal. The depth of the shower is important because if a large fraction of the energy was lost out of the end of the crystal, the reconstruction of the energy of the original photon became poor. The length of these CsI crystals was approximately 16 radiation lengths and absorbed practically all of the energy of a 2 GeV photon. The lateral extent of the electromagnetic shower was important in reconstructing
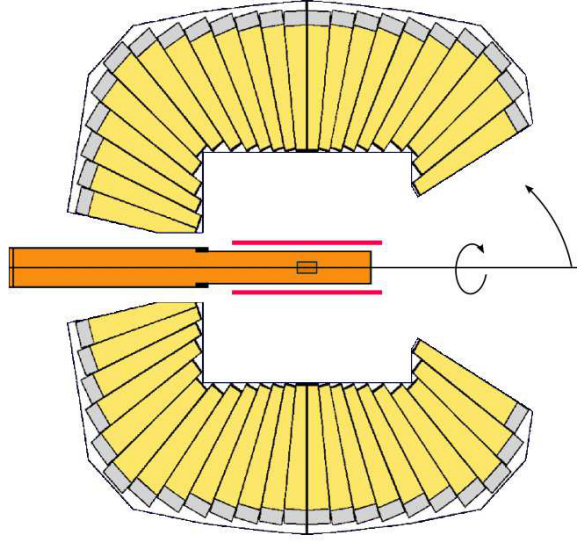
Figure 3.5: Crystal Barrel Detector Schematic. The target assembly is at the center of the Crystal Barrel with the beam coming in from the left and exiting to the right. The two lines surrounding the target are the Inner Detector (See Section 3.5.2).

the point of impact of the photon. The Molière radius[2] for CsI (See Table 3.1) was actually larger than a single crystal and meant a photon will deposit its energy over several crystals, called a cluster. Using an energy weighted reconstruction, the angular resolution was optimized to $1° - 1.5°$, depending on the energy of the initial photon. The reconstructed energy resolution of the Crystal Barrel was

$$\frac{\Delta E}{E} = \frac{2.8\%}{\sqrt[4]{E[\text{GeV}]}} \quad .$$
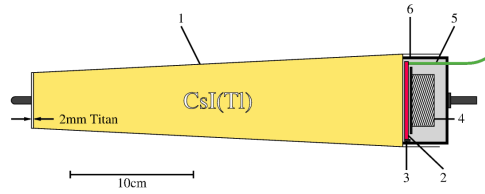
Figure 3.6: Crystal Barrel Crystal Module Schematic. Crystal Barrel CsI(Tl) Crystal Module. (1) Titanium Casing, (2) Wavelength Shifter, (3) Photodiode, (4) Preamplifier, (5) Optical Fiber, (6) Electronics Casing

---

[2]The radius of a cylinder in which a photon deposits 90% of its energy.

Table 3.1: Detector Crystal Properties. Previously published in [19, 20]. The radiation length is for a 2 GeV photon.

	CsI(T1) Crystals	BaF_2 Crystals
Detector	Crystal Barrel	TAPS
Density	4.53 g/cm^3	4.89 g/cm^3
Radiation Length (X_0)	1.86 cm	2.05 cm
Crystal Length	25 cm	30 cm
Molière Radius	3.8 cm	3.1 cm
Energy Loss Rate	5.6 MeV/cm	6.6 MeV/cm
Emission Maximum (decay time)	550 nm (0.9 μs, 7 μs)	220 nm (0.9 ns)
		300 nm (630 ns)

Figure 3.6 shows a picture of an individual module in the Crystal Barrel detector. Once the shower has happened in the crystal, the light then went through a wavelength shifter. The wavelength shifter shifted the light from the crystal to a wavelength which was optimal for the photodiode to detect. The output of the photodiode was amplified and transmitted to readout electronics outside the experimental area. An additional optical fiber was used to feed a known light source directly into the wavelength shifter to monitor the response of the photodiode.

3.5.2 Inner Detector
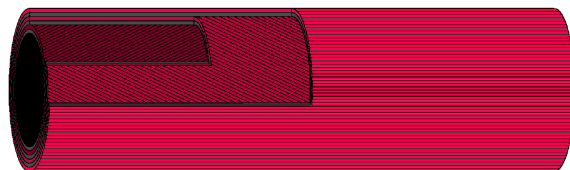
Figure 3.7: Inner Detector Schematic. Consists of 513 scintillating fibers arranged in 3 layers to detect the passage of charged particles.

Figure 3.7 shows the composition and Figure 3.5 shows the position of the Inner Detector in the experimental setup. The function of this detector was to record the timing and position of charged particles which could be detected by the Crystal Barrel crystals. The angular coverage of the detector covers the whole azimuthal range and from 30° to 172° in the polar angle.

The Inner Detector was composed of 513 2-mm diameter scintillating fibers arranged in 3 layers. These three layers were attached to 40 cm long carbon fiber tubes stabilized by a 1.8 mm thick aluminum pipe surrounding the target. The scintillating fibers were connected in groups of 16 to a multi-anode photomultiplier tube, which

provided fast timing signals. As a charged particle passed by a scintillating fiber, light was sent down the fiber and transmitted by lightguides to the photomultiplier tube, which was located outside the Crystal Barrel detector.

Each layer of scintillating fibers was arranged in different orientations to the beam line. The outermost layer of fibers were aligned parallel to the beam line. The middle layer and inner layers were lying at $+25.7°$ and $-24.5°$ angles to the beam line respectively. Each fiber in the middle and inner layers extended the whole length of the detector and half a revolution around the cylinder. This arrangement allowed a unique position to be determined when a hit was registered in two of the three layers. The detection efficiency[3] for a hit required in two of three layers was 98.4%, while a hit required in all three layers had an efficiency of 77.6% [21].

3.5.3 TAPS Detector
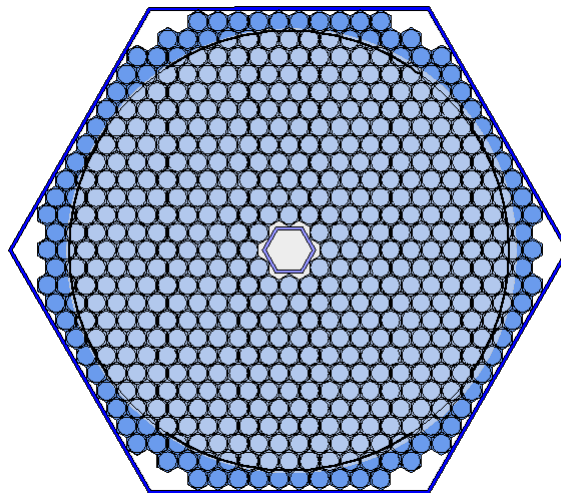
Figure 3.8: TAPS Detector Schematic. 528 BaF_2 crystals arranged in a hexagon. The lighter colored area is the $30°$ area left open by the the Crystal Barrel Detector in the downstream direction.

Figure 3.8 shows the overall design of the TAPS detector. The TAPS was designed in the mid 1980's as a portable electromagnetic calorimeter which was excellent at detecting photon energy and timing information, while also detecting the presence of charged particles. The TAPS detector was moved from Mainz to Bonn in 2001 to be used in conjunction with the Crystal Barrel detector for this experiment.

The TAPS detector was a wall of 528 BaF_2 crystal modules built into a hexagonal wall and was placed 1.81 m downstream of the target to cover the forward hole left by the Crystal Barrel detector. The TAPS detector covered the whole azimuthal angle

---

[3]probability for a charged particle to be detected
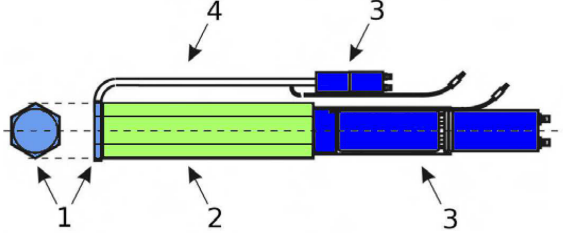
Figure 3.9: TAPS Crystal Module Schematic. TAPS BaF_2 Crystal Module. (1) Plastic scintillator (2) BaF_2 Crystal (3) Photomultipliers (4) Optical Fiber

and from 30° to 5.8° in the polar angle. This forward polar angle coverage was critical since the kinematics of the initial state indicate many of the particles of interest would travel through this region.

The schematic of an individual crystal module is shown in Figure 3.9. The properties of the BaF_2 crystals are summarized in Table 3.1. The BaF_2 crystal faces were hexagonal in shape and were 59 mm in height and 25 cm in length ($\approx$ 12 radiation lengths). The crystals tapered down to a 54 mm diameter cylinder which connected to a photomultiplier tube. The face of each crystal was covered by a 5 mm thick plastic scintillator producing a signal which was conveyed to another photomultiplier tube via a lightguide. This plastic scintillator produced a signal when a charged particle passed into the face of the crystal. The energy resolution for a 45-790 MeV photon of the TAPS detector was given by [22]

$$\frac{\sigma(E_\gamma)}{E_\gamma} = \frac{0.59\%}{\sqrt{E_\gamma}} + 1.8\% \ \ .$$

The combination of relatively fast decay times (compared to CsI) and photomultiplier readouts allowed the TAPS detector output to be used efficiently in the trigger system (See Section 3.6). The output from the photomultiplier tubes were split 4 times and processed simultaneously for data storage and triggering. Two of the outputs are linked to the LEDs[4] which led to the triggering decisions (Section 3.6.1). The data storage was linked to digitization components for storage on disks. The final output was fed into a Constant Fraction Discriminator (CFD) used for timing information and possibly further trigger processing.

3.5.4 γ Veto Detector

The γ Veto Detector is shown in the far right of Figure 3.1 and was important for determining the photon flux and beam position. The γ Veto Detector was made of 9 PbF_2 crystals arranged in a 3 by 3 cube and readout by photomultiplier tubes. As unreacted beam photons entered the crystals, pair production of particles caused the emission of Cherenkov light.

---

[4]Leading Edge Discriminators

The γ Veto Detector was mainly used to check the spacial distribution of photons in the beam. Some of the photons detected in the tagging hodoscope did not actually pass through the target and should not be counted in the photon flux. If these photons do not pass through the target then they did not have a chance to produce a hadronic reaction and can cause an error in the normalization needed to measure a differential cross section.

3.6 Trigger

When a photon interacts with matter, most interactions do not involve the production of hadrons. At photon energies above 10 MeV, the most likely process is the production of electron-positron pairs. Since the probability of the reactions $\gamma p \to p\omega$ and $\gamma p \to p\pi^0\omega$ happening is many magnitudes less than pair production, it would be wasteful to store the data from every particle detection.

The solution to this problem was to decide what is a good reaction to record as it happened. In order to decide "on-the-fly" and collect enough events to have reasonable statistical error bars on the results, the decision must be done quickly and accurately. Too much time spent deciding meant time was not used taking data.

The trigger is the name of the decision making component, which for the CBELSA/TAPS experiment was constructed as a two-level process. Since the TAPS detector output was very fast and could be read and used in a decision as soon as it reached the readout electronics, its output was used in the first level trigger. The first level trigger was entirely electronics based, therefore only very simple trigger logic could be used. Once the output passed the first level trigger, digitization of the analog detector signals began and more complex trigger logic was applied using output from the much slower Crystal Barrel detector output during the second level trigger, which was also electronics based.

3.6.1 First Level Trigger

The output of each TAPS crystal module was split and connected to two leading edge discriminators (LEDs). The two LEDs were set to two different threshold values to enable two different types of discriminator signals called *LED high* and *LED low*. The threshold values were set ring by ring by how close the crystal was to the beamline and to be above most of the electromagnetic background. The ring of crystals closest to the beamline had threshold values of approximately 1 GeV. The threshold values decreased as the crystals got farther away from the beamline and suppressed a large amount of electromagnetic background and noise which grows in energy and size as the distance to the beamline gets small.

The LED low and LED high threshold signals were grouped together into 8 segments and are shown in Figure 3.10. All the individual crystal modules in a segment were linked together with a logical OR circuit producing one LED signal per segment.
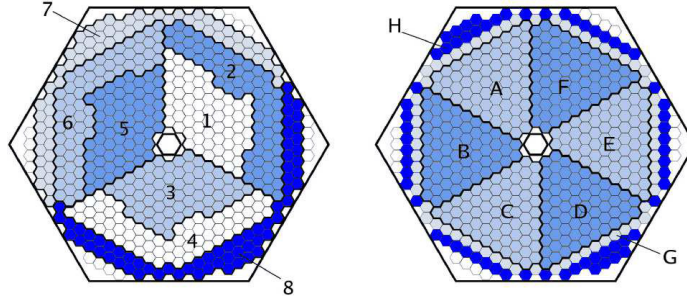
Figure 3.10: TAPS Trigger LED Map. The TAPS trigger segments for the LED low (left) and LED high (right) trigger conditions.

This arrangement of LED low segments allowed the suppression of electron-positron pair triggering by requiring a hit in two different segments.

3.6.2 Second Level Trigger

Once the first level decision was made, enough time had passed to gather information from the Crystal Barrel. Simultaneously, the data from the detectors began to be digitized for storage and used to make a final decision on whether to record the data to disk.

To determine if the event was to be kept, the trigger system determined quickly how many photons had been recorded. Since a photon showered its energy over several crystals, the determination came down to how many clusters[5] of hits were recorded. The FAst Cluster Encoder (FACE) was the component responsible for finding clusters based on a cellular logic. The cluster finding took from 6-10 μs, depending on the number of crystals involved. If after counting the clusters, it was determined not enough photons had been detected, the trigger system interrupted the digitization process and cleared the buffers to consider another event. Otherwise, the event was recorded to disk.

The total time needed for digitization was on the order of 1 ms and allowed time for a complex second level decision.

3.6.3 Trigger Conditions

The conditions for triggering were selected to maximize the number of desired hadronic events while minimizing the number of background events. For this data taking period, one of two conditions had to be met before an event was recorded. The conditions used for the data taken in this analysis are listed in Table 3.2.

For *trigger-or* data taking runs, a different trigger was used to take data used to count the total number of photons for purposes of photon flux determination. The

---

[5]A contiguous pattern of crystals recording a hit.

Table 3.2: List of Conditions for Triggering.

Condition A	Two LED-low segments registering at least one hit above the LED-low threshold.
Condition B	One LED-high segment registering at least one (two for polarized data) hit above the LED-high threshold and at least one cluster in FACE.

trigger used in these runs was only a hit in one of the scintillator bars of the tagging system.

3.6.4 Trigger Simulations

To ensure the Monte Carlo simulations and detector acceptance corrections of the experiment were correct, the trigger conditions have been properly modeled. The simulated detector response was analyzed to make sure the signals fulfilled the triggering conditions. For every data event recorded from the experiment and every Monte Carlo event analyzed for acceptance, a 16-bit word was generated describing the trigger conditions. This 16-bit word was either analyzed for quality control for data events or used as a trigger cut for Monte Carlo events.

The proper modeling of the trigger in the Monte Carlo study involved precise information on the LED thresholds used in making the trigger decision. The calibration and determination of the LED thresholds are discussed in Section 4.3.

3.7 Readout Electronics

When a suitable event for recording was found, the response of each component had to be converted to a digital signal for storage on disk. The conversion of energy signals from the photomultiplier tubes or photodiodes was done via Analog to Digital Converters (ADC). ADC output was a digital number which was proportional to the original analog signal. Timing information was recorded using Time to Digital Converters (TDC). TDCs are devices which express the timing of detector outputs as a digital signal. The TDC modules recorded the timing of signals continuously but when recording the TDC output on disk, the signal was reported as relative to the timing of the trigger signal.

In order for the ADC and TDC output to be useful, the calibration of these signals was done. In the next chapter, the calibration of these outputs will be discussed.

CHAPTER 4

SUB-DETECTOR CALIBRATIONS

The output of each individual detector module was converted from an analog signal to a digital signal by an Analog to Digital Converter (ADC) or a Time to Digital Converter (TDC). The output of an ADC is a digital value related to the energy recorded of a signal. The output of a TDC is a digital value related to the timing of the signal. The ADC and TDC outputs are the values written to disk during data taking.

After data taking is over, each TDC and ADC output must be calibrated to be useful in reconstructing events. The calibration of TDC values is discussed as the time calibration in Section 4.1.

The energy calibration of the calorimeter crystals is the most critical part of the calibration. The output of each crystal module was converted to a physical unit by comparing to some known quantity. The quantity used in this case was the nominal invariant mass of the π^0 meson ($\sim 135 \mathrm{MeV}/c^2$). The π^0 meson decays to two photons approximately 98% of the time. By using the energy and position detected for each pair of detected photons, the invariant mass for any potential π^0 mesons can be reconstructed. The most prominent peak in this distribution is most likely the π^0 meson. By moving the peak position of this peak to the nominal mass of the π^0 using the calibration constants for each crystal, each crystal module was calibrated. This procedure is discussed further for the TAPS crystal modules in Section 4.2.1 and for Crystal Barrel crystal modules in Section 4.2.2.

To optimize the triggering process described in Section 3.6, the calibration of both LED-low and LED-high thresholds is described in Section 4.3.

4.1   Time Calibration

The first step in the time calibration was to obtain the conversion factor relating the value of the TDC output to physical units. The TDC module output was calibrated to physical time units by feeding light pulses of known frequencies into the PMTs. The TDC output could then be monitored to obtain a multiplicative factor which converted the output to usable values.
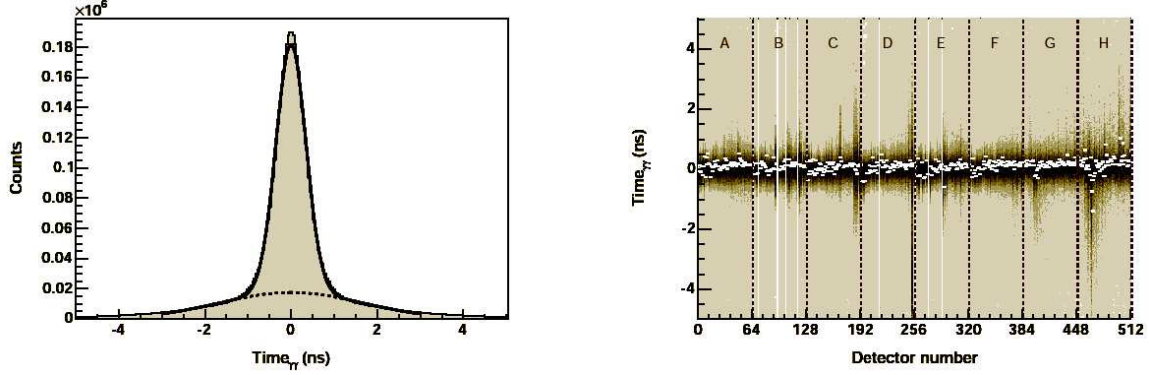
Figure 4.1: TAPS Time Spectrum (Calibrated). The time difference between two photons decaying from one π^0 meson detected in TAPS crystals. Left: Time difference integrated over all TAPS Crystals. Right: Time difference separated into the difference for each crystal module in TAPS. The white points correspond to the peak position determined using a Gaussian fit. Vertical white bars or empty channels are from crystal modules with defective time signals. An overall time resolution of 0.39 ns has been achieved.

The second step to the time calibration was to synchronize the signals from each TDC-module in the TAPS detector. Each TDC-module and PMT had cables and components with potentially varying lengths which could affect at what time the TDC signal was recorded and processed. This calibration is discussed in Section 4.1.1.

Finally, the TDC output from the Tagger scintillating fibers were calibrated in relation to the TAPS detector TDCs. The TAPS detector was used as the standard due to its excellent timing resolution. This is discussed in Section 4.1.2.

4.1.1 TAPS Detector Time Calibration

Once the TDC output was converted to time units, the timing of each crystal module in the TAPS detector must be synchronized. An offset of timing signals could happen because the length of each cable could be different for different crystals causing the timing of the signals to reach different TDCs at different times. These differences must be calibrated away in order for the TDC output to be useful in reconstruction.

The most copiously produced meson decaying to photons is the π^0 meson. This meson decays to photons approximately 98% of the time and when decaying at the momentums characteristic of this experiment, the photons are detected at small opening angles. This meant a π^0 meson decaying into the TAPS detector produced photons which were detected in crystals fairly close together. By reconstructing π^0 mesons detected in TAPS, the difference between the TDC values for the crystals detecting each photon should be zero.
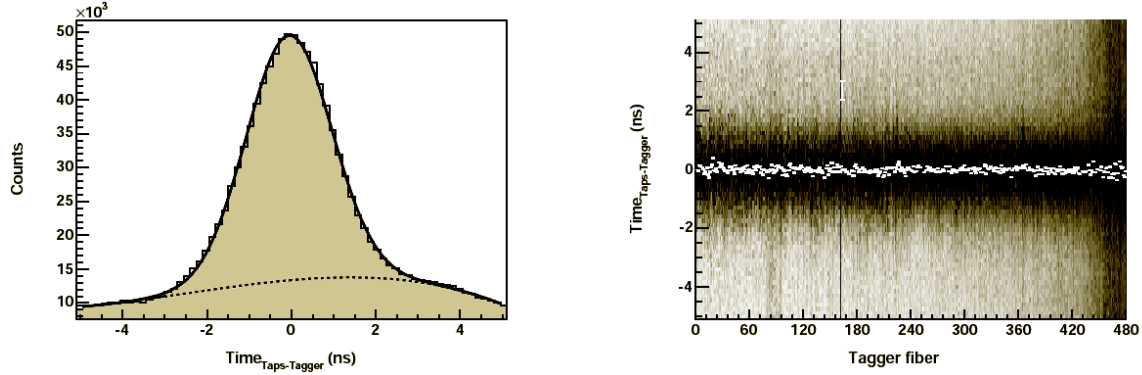
Figure 4.2: Tagger Hodoscope Time Calibration Relative to TAPS. The time difference between a π^0 meson detected in TAPS crystals and an electron detected in a tagging fiber. The difference has been calibrated to zero. Left: Time difference integrated over all Tagger fibers. Right: Time difference separated into the difference for each Tagger fiber. The white points correspond to the peak position determined using a Gaussian fit. An overall time resolution of 0.69 ns has been achieved.

The actual calibration of the TAPS TDC values took a large amount of data and many iterations to complete. To do the calibration, data events from the experiment were used to reconstruct π^0 mesons from photons detected in TAPS. The photon clusters were reconstructed with the central crystal being defined as the crystal with the largest energy deposit. The time information from each central crystal is filled into its histogram. After all the potential π^0 decays were processed, the histogram for each crystal was fitted with a Gaussian function to determine the peak position, or the average time difference from all the other surrounding crystals. An additive offset value was determined to move the peak position in the histogram to zero, or no time difference. Since this process was dependent on the rest of the crystals having the correct timing calibration on average, the process was repeated until all the time differences "relax" to zero. The calibrated time differences for the TAPS crystals are shown in Figure 4.1 and suggests the average time difference between each crystal and its neighbors is approximately zero. An overall time resolution of 0.39 ns has been estimated [23].

4.1.2 Tagger Hodoscope Time Calibration

Once the TAPS timing calibration was complete and the TDC for each tagger scintillating fiber was converted to a time, the timing calibration for the tagger was done. The TAPS reconstructed π^0 mesons were used again, however this time the average time between the two photons in the decay were used as the timing reference. Since these π^0 mesons were the result of an initial state photon passing through the tagger, a corresponding electron must have been detected in the tagger fiber

scintillators. Time values from electron hits in the tagger fibers were used to form a time difference from each reconstructed π^0 in TAPS and was filled into a histogram for each tagger fiber. In the resulting histogram, a peak was seen corresponding to the time for travel from the tagger to TAPS. In each fiber, the peak of the timing spectrum was found and a calibration value was defined by moving the peak position to zero.

Figure 4.2 shows the result of the Tagger time calibration. The time differences have been calibrated to zero. An overall time resolution for the Tagger timing of initial state photons has been estimated to be 0.69 ns [23].

4.2 Energy Calibration

The conversion of ADC values to physical units for each crystal module in the TAPS and Crystal Barrel detector is called the energy calibration. The response of each crystal module was dependent on a multitude of factors causing each one of the over 1800 crystals to be treated individually. The calibration of TAPS crystal modules (Section 4.2.1) and Crystal Barrel crystal modules (Section 4.2.2) were similar but required slightly different procedures to calibrate, due to the different spacial orientation of the crystals.

The energy of the initial state photons was detected using the Tagging hodoscope. The calibration of the Tagger output is described in Section 4.2.3.

The trigger system, described in Section 3.6, relied on the LED thresholds to make decisions on whether to record an event or not. For the trigger system to work efficiently, the LED thresholds were optimized (Section 4.3).

4.2.1 TAPS Detector Energy Calibration

The ADC output from the TAPS crystal modules had a linear relationship with the energy deposited in the crystal [24]. To convert the ADC value to a physical unit, both a zero-point value (y-intercept) and a gain (slope) must be determined. Two methods for determining the calibration for the TAPS crystal modules were used in succession: Cosmic Ray Method and Invariant Mass Method.

Cosmic Ray Calibration Method. The output from the uncalibrated TAPS crystal modules to the same stimuli can differ greatly. A rough calibration using the cosmic ray calibration method was done before data taking, in order to monitor the output during the experimental data run.

To determine the zero-point value, or the ADC value corresponding to zero energy deposited (Pedestal), a 1 Hz pulser was linked to the Constant Fraction Discriminator (CFD) and was used during the cosmic ray calibration data taking run.

The gain was determined using naturally occurring cosmic muons. All the TAPS crystals are arranged in the same orientation with respect to the sky therefore the cosmic muons deposit the same amount of energy in each crystal. Assuming the
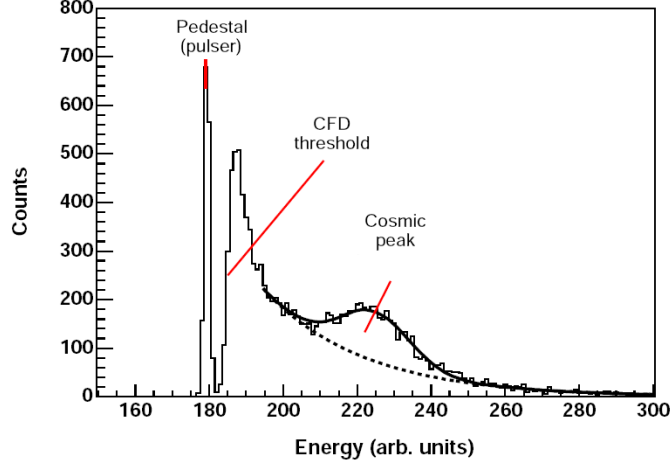
Figure 4.3: TAPS Spectrum of ADC Values During a Cosmic Ray Calibration.

muon penetrates the BaF_2 crystals perpendicularly, the energy deposit is 38.9 MeV[1]. Figure 4.3 shows a typical spectrum from a cosmic ray calibration run. The pedestal (zero-point value) peak indicates at what ADC value zero energy is deposited. The CFD threshold indicates at what value the constant fraction discriminator attenuates input. The cosmic peak shows the distribution of deposited energies which are left from cosmic muons. The gain for each crystal is obtained by histogramming the ADC values and fitting a Gaussian function to the cosmic peak. The gain was defined as the conversion factor between the precalibrated value of the cosmic peak position and the calculated muon deposition energy (38.9 MeV).

Invariant Mass Calibration Method. For data reconstruction and analysis, a much more precise method of energy calibration was needed. As with the time calibration of the TAPS TDC values, the π^0 decay to two photons was used as a reference. The well known invariant mass of the π^0 meson ($M_{\pi^0} = 134.9866 \pm 0.0006$ MeV) [1] was used as the value the crystals are calibrated to. Using the energy of each photon in the decay (E_1, E_2), the invariant mass of the π^0 meson was calculated by

$$M_{\pi^0} = \sqrt{E_1 \; E_2(1 - \cos\theta_{1,2})} \;\; ,$$

where $\theta_{1,2}$ is the angle between the two photons and the center of the target has been used as the vertex of the angle.

Because two photons decay from each pion, the calculated mass of the pion was dependent on the calibration of more than one crystal module. However, the central crystals for each photon cluster are the crystals which have the most effect. The reconstructed invariant mass for each pair of photons in TAPS was filled into the histogram for each central crystal. The value of the π^0 peak in each crystal's histogram

---

[1]Crystal thickness = 5.9 cm, dE/dx = 6.6 MeV/cm
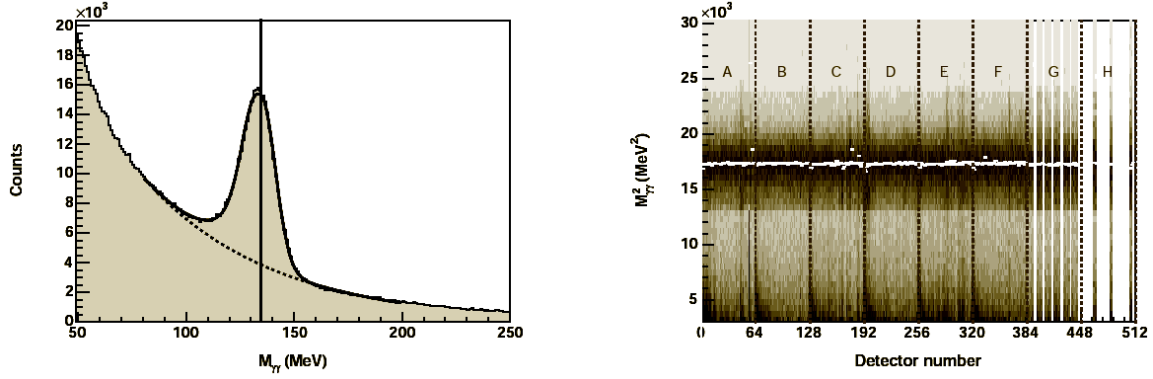
Figure 4.4: TAPS Calibrated Spectrum of Two Photon Invariant Masses. Left: Two photon invariant mass integrated over all crystals. Vertical line corresponds to the nominal mass of the π^0 meson. Right: Two photon invariant mass as a function of crystal module number. White points indicate the fitted peak of the π^0. The empty channels are due to the crystals shadowed by the edges of the Crystal Barrel detector.

was directly related to the calibration of that crystal. The contribution of other crystals, in theory, should be averaged out. Since this was not quite true, the process has to be done iteratively to "relax" the calibration into the correct values for all crystals.

Figure 4.4 shows the results of the energy calibration of the TAPS crystal modules. The invariant mass peak of the π^0 meson shows its peak position at the correct value. The empty channels in Figure 4.4 highlight an issue which arose due to the relative positions of the TAPS and Crystal Barrel detector. These empty channels were due to the shadowing of the Crystal Barrel detector of these crystals and therefore had a lack of π^0 photons striking this region (see Figure 3.8). To remedy this situation, these crystal modules were assigned calibration values which were an average of all other modules. These crystals were rejected as center crystals in the photon cluster reconstruction. In this way, the effect of the lack of direct calibration on these crystal modules was minimized.

As a cross check for this calibration, the invariant mass of the η meson was reconstructed using the calibration values from the π^0 invariant mass calibration. The invariant mass of the η meson was reconstructed through its two photon decay. Unfortunately, the reconstructed mass of the η was 5-10 MeV too large. This discrepancy was attributed to the crystals at the edge of a photon cluster not reporting an energy deposit because the value fell below the threshold for a hit (10 MeV). The deposited energy of each photon was mostly in the central crystal but a non-negligible fraction was deposited in the surrounding crystals. If the energy detected in the crystal on the outer range of the photon cluster fell below the threshold, an energy deposit was not recorded. This effect is amplified by the orientation of the crystals in the TAPS detector, which do not have their long axis pointed at the target center. This ori-

Table 4.1: TAPS π-η Calibration Values. Run numbers are the numbers given to each individual file in the dataset.

Run Numbers	b	c
Unpolarized Data (October-November 2002)		
21304-24378	1.012	$-2.47 \cdot 10^{-5}$
24379-24599	1.001	$-1.09 \cdot 10^{-5}$
24600-24949	1.041	$-2.52 \cdot 10^{-5}$
24950-26798	1.001	$-1.09 \cdot 10^{-5}$
Linearly Polarized Data (March 2003)		
35252-37610	1.012	$2.47 \cdot 10^{-5}$
Linearly Polarized Data (May 2003)		
45525-47176	1.001	$-0.88 \cdot 10^{-5}$

entation increases the chance for small energy deposits. This threshold value could not be tuned lower due to crystal noise and unwanted electromagnetic background. Since the photon energies from the η decay are typically larger than the photons from the π^0 decay, the effect was smaller in comparison. Since this effect was calibrated away for π^0 decay photons and assumes the same magnitude for the effect for η decay photons, the η decay photons have been over corrected.

To correct for this effect, a second calibration was added to the energy calibration procedure. The function used for calibration is

$$E_{final\ calibrated} = a + b\ E_{\pi^0\ calibrated} + c\ E^2_{\pi^0\ calibrated}\ ,$$

where a is set by the pedestal to be zero and $E_{\pi^0\ calibrated}$ is the energy value after the π^0 invariant mass calibration. The parameters b and c were determined to be

$$b = \frac{m_\pi}{m^{\gamma\gamma}_\pi} - c \cdot E_\pi$$

$$c = \left(\frac{m_\eta}{m^{\gamma\gamma}_\eta} - \frac{m_\pi}{m^{\gamma\gamma}_\pi} \right) \Big/ \left(E_\eta - E_\pi \right)\ ,$$

where (m_π, m_η) are the PDG invariant masses, $(m^{\gamma\gamma}_\eta, m^{\gamma\gamma}_\pi)$ are the reconstructed invariant mass peak positions and (E_η, E_π) are the mean reconstructed energies. The determined parameters are shown in Table 4.1.

4.2.2 Crystal Barrel Detector Energy Calibration

The energy calibration for the Crystal Barrel detector was much like the invariant mass calibration method for the TAPS detector. A histogram was defined for each crystal module and filled with two photon invariant masses. A histogram was filled with an invariant mass if its corresponding crystal was the central crystal in one of the
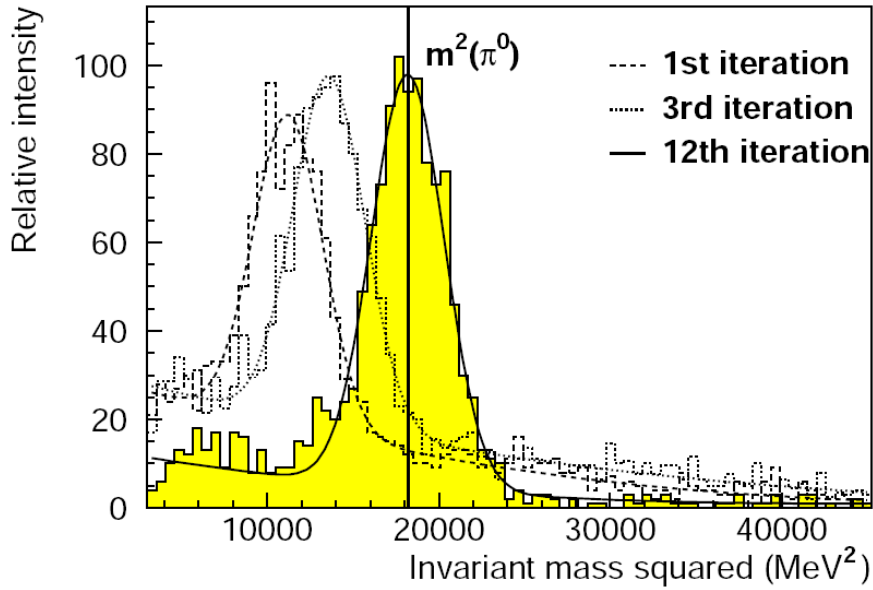
Figure 4.5: Crystal Barrel Spectrum of Two Photon Invariant Masses for One Crystal Module. Each layer in the plot shows the effect of the iterated energy calibration of the crystal modules. The line is the nominal mass of the π^0 meson.

two photon clusters. The π^0 peak was fitted using a Gaussian peak and a conversion factor defined which moved the peak position to the PDG mass of the π^0 meson. Since the invariant mass reconstruction always relied on more than one calibration value for one crystal, the process was done iteratively to "relax" the calibration values into the correct values.

Figure 4.5 shows the effect each iteration has on the position of the π^0 peak. As each iteration was done, the calibration value of each crystal was shifted closer to the value which placed the peak position to the nominal mass of the π^0 meson.

To check the calibration, the peak position of the η meson two photon invariant mass was checked. In this case, the peak position is within 1 MeV of the PDG value for the η meson and therefore no need for a second calibration function. The reason for this was the relatively low threshold values for recording an energy deposit (1 MeV) for Crystal Barrel crystal modules and the orientation of the crystals. These crystals had their long axis pointed at the target and had a lower probability for smaller energy deposits. The effect was a much smaller fraction of the total photon energy deposited goes unreported in the outer crystals in the photon clusters.

In order to check the energy calibration at even higher energies, the reconstructed mass of the ω meson was checked. The position of the invariant mass for the ω meson is important for this analysis and is shown in Figure 6.7. The position of the reconstructed ω is within 1 MeV of the nominal mass given in [1] to be 782.65 MeV.

4.2.3 Tagging Hodoscope Energy Calibration

In the tagging system, bremstrahlung electrons were bent out of the beamline using a dipole magnet and detected in one of 480 scintillating fibers. The central idea of the tagger energy calibration is to assign a photon energy to each of the scintillating fibers.

The calibration of the tagger hodoscope was done through Monte Carlo simulation after carefully modeling the magnetic field from the dipole magnet and spatial position of each scintillating fiber. A 5th order polynomial was used as a calibration function relating fiber number to photon energy and was initially fitted to the Monte Carlo simulation output. To provide a quality check and corrections to the polynomial, a very low intensity electron beam from the ELSA accelerator with known energy was fed directly into the tagging system at four different energies (direct injection). The direct injection primary electron energies were set to 680, 1300, 1800, and 2050 MeV with a constant magnetic field of B = 1.413 T and no radiator. The hit patterns for each run were compared to the polynomial and corrections were made. The final calibration function used for the data reported in this thesis, at an ELSA electron energy of 3.175 GeV, is

$$
\begin{aligned}
E_\gamma^{3.175 \text{ GeV}} \;=\; & 2533.81 - 190.67 \cdot 10^{-2}x + 28.86 \cdot 10^{-4}x^2 \\
& -34.43 \cdot 10^{-6}x^3 + 95.59 \cdot 10^{-9}x^4 - 12.34 \cdot 10^{-11}x^6 \quad,
\end{aligned}
$$

where E_γ is the photon energy in MeV and x is the tagger fiber number. Figure 4.6 shows the calibration polynomial along with the direct injection data. For different ELSA accelerator electron energies, this polynomial can be scaled according to

$$
E_\gamma^{E_2} = \frac{E_2}{3.175 \text{ GeV}} E_\gamma^{3.175 \text{ GeV}} \quad,
$$

where E_2 is the new beam energy in GeV.

4.3 TAPS LED Trigger Threshold Energy Calibration and Determination

As discussed in Section 3.6.1, the TAPS crystal module output was used to produce two Leading Edge Discriminator (LED) signals. The threshold signals, LED-high and LED-low, were used to determine whether a data event should be recorded (trigger). These thresholds were set in the hardware and were calibrated to suppress e^+e^- pair production which was an overwhelming fraction of the background. The threshold levels were the same for all crystal modules in the same ring, crystals with roughly the same distance from the beamline. These thresholds were at a maximum of 1 GeV in the closest ring to the beamline and decreased down to about 100 MeV as the ring's distance from the beamline increased.
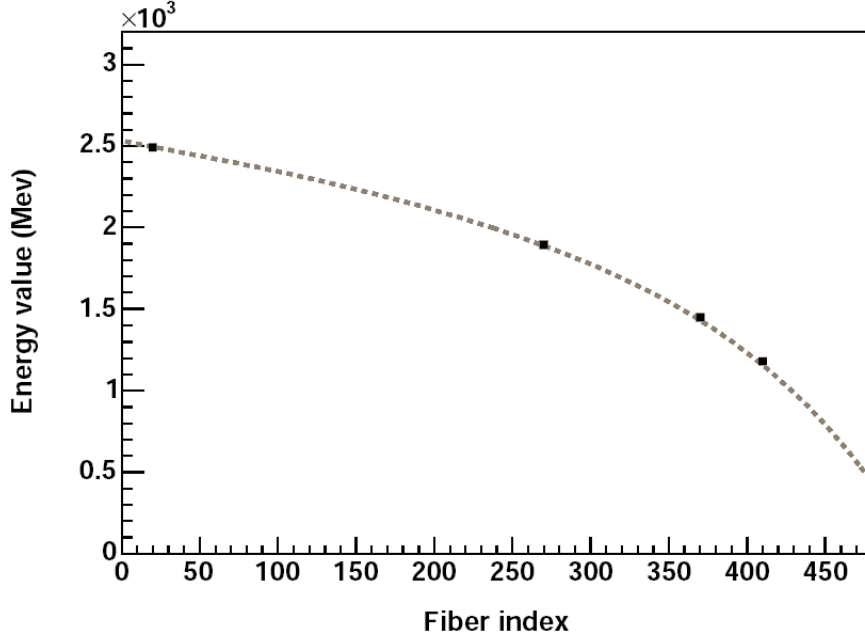
Figure 4.6: Tagger Energy Calibration Polynomial. The vertical axis is the energy of the bremstrahlung photon. The dashed line is the tagger polynomial. The data points are the direct injection data points used for corrections.

In order to correctly model the trigger in the Monte Carlo simulations, the threshold for each crystal module was determined and used in the simulation analysis. To determine the effective values, the same data were analyzed using the three possible LED signals. Data hits in a crystal had either a LED-low, LED-high or no signal. The ratio of the number of these data events with different signals as a function of energy deposited were used to determine the LED thresholds.

Figure 4.7 shows the LED threshold ratios for the different signals and different particles. These ratios were formed by dividing the number of hits which triggered a LED signal and all hits. The different behavior for photons and protons was due to the pulse shape or shower development the particle made in the crystal. The threshold was defined as the energy value where the ratio fell to 50%. A threshold was determined for all TAPS crystal modules and both signals.

In the final analysis in this thesis, these thresholds were changed in the software reconstruction of the data. The triggering on protons in TAPS caused detector acceptance issues when using the hardware threshold values described above. During the software reconstruction of these data, the signals were subjected to the same triggering rules as during the data taking but these thresholds were increased. This new threshold was also used in the Monte Carlo simulation reconstruction [25].
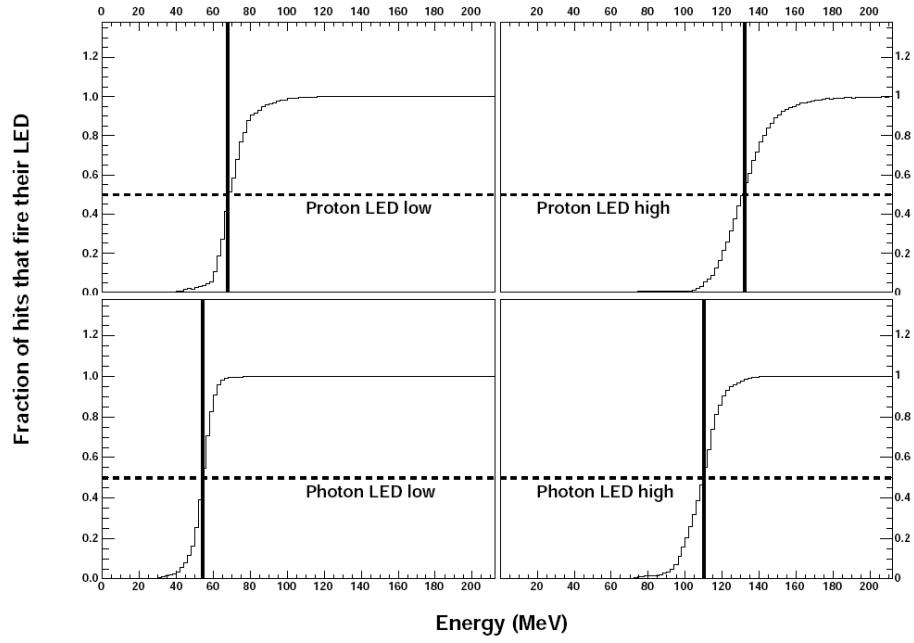
Figure 4.7: LED Threshold Ratios for a Typical Crystal Module. The ratios of crystal module hits with a LED-high (Right) or LED-low (Left) signal to all hits. The vertical line marks the threshold for the crystal.

CHAPTER 5

SUB-DETECTOR RECONSTRUCTION

The process of reconstructing a particle's energy and momentum from a recorded set of detector output is called reconstruction. In this chapter, the method by which particle information was deduced is discussed.

The energy deposits of charged particles were much smaller than for photons and left a signal in only one or two crystal modules. These clusters were treated exactly the same way as the photons, but the scintillating detectors which cover the same angular range marked the information as a charged particle. Since the proton usually does not leave all its energy in the crystal, the energy and momentum reconstruction was poor. However if the charged particle information is ignored and reconstructed using a missing particle fit, the energy and momentum of the proton can be deduced.

5.1   TAPS Reconstruction

When a photon interacted with the crystals in the CBELSA/TAPS experiment, its energy deposit was spread over several crystals. The electromagnetic shower caused by the photon leaked from the central crystal into the surrounding crystals. A contiguous group of crystals with an energy deposit from one photon is called a cluster. To find the full extent of the cluster, a cluster finding algorithm was used to find all the crystal modules with a contiguous energy deposit above the crystal's Constant Fraction Discriminator (CFD) threshold.

The hardware CFD thresholds for the TAPS modules in this analysis were all set to about 10 MeV. Any energy deposit in a crystal module below this threshold was not recorded. In independent analyses of the data, the experimentally determined CFD thresholds have been found to be varying over a large range. These varying thresholds could cause problems with the analysis, therefore the CFD threshold in the software reconstruction has been set to 30 MeV, which was above all hardware CFD thresholds. The new thresholds required the experiment to be recalibrated, since the energy calibration in the previous section corrected for the energy lost due to the threshold.

For crystals to be considered in the same TAPS cluster, the energy deposits had to have happened very close together in time. The crystal modules had to have recorded an energy deposit within 5 ns of the energy deposit of the central crystal to be considered within a cluster. If through defects in the crystal modules, no time was recorded by the central crystal module, the crystal with the next largest energy deposit was used as the timing reference. Crystal modules without timing information are assigned a time derived from the surrounding modules. If a module had an energy deposit spatially belonging to a cluster but has timing information outside the timing window, its contribution was ignored.

The energy of the photon is simply a sum of the energies in the crystal modules belonging to its cluster. The higher CFD threshold mentioned earlier also reduced the contribution of *split-offs*. Split-offs are energy deposits in a crystal which somehow got cut off from the main part of the cluster. The split-off resulted from a neighboring energy deposit leakage but through CFD thresholds or other effects became isolated from the cluster. These contributions must be suppressed because if the split-off was allowed to be counted as another particle, the number of particles would be wrong and the event would never be reconstructed as what originally happened.

The position of the photon was determined by the spatial distribution of the energies within the cluster. Using a weighting method, the position of the photon was determined to a finer resolution than the simple granulation of the detector suggests. To find the precise position of the photon, the weighted averages

$$X = \frac{\sum_i w_i x_i}{\sum_i w_i} \quad \text{and} \quad Y = \frac{\sum_i w_i y_i}{\sum_i w_i} \tag{5.1}$$

were computed, where

$$w_i = \max\left(0, W_0 + \ln \frac{E_i}{\sum_i E_i}\right) \quad, \tag{5.2}$$

where i is the index of crystals in the cluster. The constant W_0 was determined through Monte Carlo simulations to be $W_0 = 4$. This logarithmic weighting method has been found to yield a significantly better position description than a linear weighting [26].

Up to this point, the position determination of the photon has ignored the geometry of the TAPS detector. The geometry of a wall of crystals meant the photons will not enter the crystals perpendicularly and the non-negligible depth of the electromagnetic shower caused errors in the position reconstruction. Figure 5.1 shows a visual representation of this issue. To account for this discrepancy, the shower depth Z was calculated by [1]

$$Z = X_0 \left(ln\frac{E}{E_c} + C_\gamma \right) \quad, \tag{5.3}$$

48
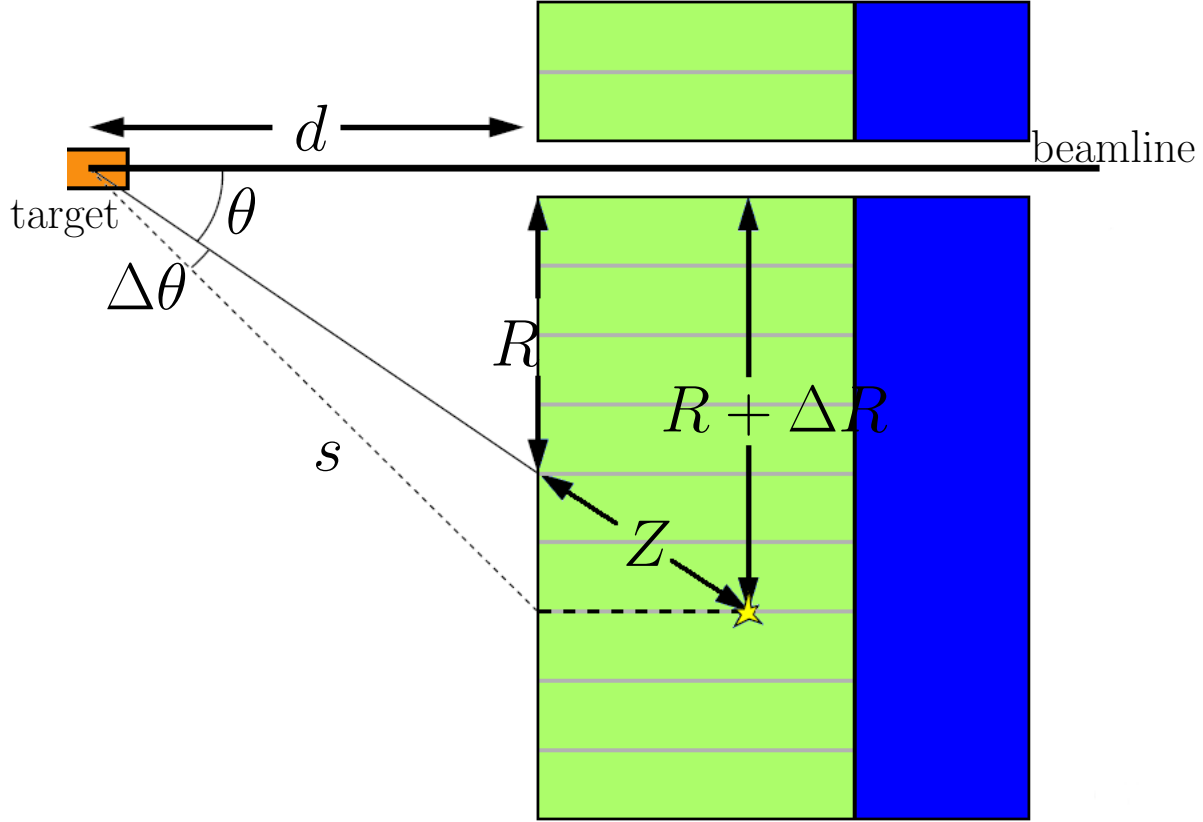
Figure 5.1: TAPS Shower Depth Correction. Due to the depth of the electromagnetic shower, the polar angle must be corrected.

where E_c is the critical energy[1] for BaF_2 crystals ($E_c = 12.78$ MeV) and X_0 is the radiation length of BaF_2 ($X_0 = 2.03$ cm). The constant parameter C_γ was reported in [1] to be $C_\gamma = 0.5$. However Monte Carlo simulations for this experiment indicated this value was too small and was set to $C_\gamma = 2.0$. This value returned the most accurate reconstruction according to Monte Carlo simulations. With the correct shower depth determined, the correction was approximated by [27]

$$\frac{\Delta R}{R} = \left(\frac{s}{Z} + 1\right)^{-1} \quad . \tag{5.4}$$

Using this method of reconstruction, the polar angle was determined to within $1.3°$ [23].

For a particle to be marked as charged, the plastic scintillator in front of either the central crystal or a crystal adjacent to the central crystal registered a hit.

---

[1]defined as the value of photon energy which is equal to its ionization energy lost per radiation length

5.2   Crystal Barrel Reconstruction
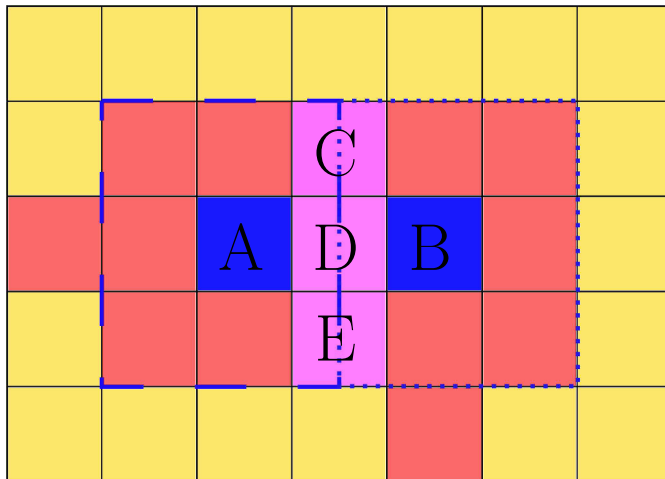
Figure 5.2: Crystal Barrel Detector PED Reconstruction.   Each square represents one crystal. The crystals A and B are crystals with local maxima (central crystals). The colored squares immediately surrounding crystals A and B are crystals with energy deposits. The lightly shaded crystals on the outside of the graphic are crystals with no energy deposit. The dotted (dashed) line indicates the energy deposits assigned to the "nine" energy of central crystal A (B).

The methods for reconstruction of photons in the Crystal Barrel (CB) detector are very similar to the methods for TAPS. Clusters were found in the same way as for TAPS clusters but the single crystal threshold energy for an energy deposit to be recorded was 1 MeV and the total cluster energy threshold for a cluster to be kept in the analysis was 20 MeV (suppression of split-off contributions). However due to the decreased granularity compared to the TAPS detector, the cluster finding algorithm for the CB detector searched for local maxima within clusters to determine if two or more particles had overlapping electromagnetic showers. If only one maxima existed within the cluster, all the energy deposits were summed over and assigned to the same Particle Energy Deposit (PED).

Figure 5.2 illustrates how the cluster finding algorithm separated the energy deposits for the two local maxima in a cluster. If two or more local maxima exceeding 13 MeV in energy within the cluster were found, the cluster finder assumed two or more particles were responsible for the cluster. The cluster finder attempted to separate the energy of the cluster into separate PEDs. The first step in cluster separation was to form the "nine" energy for each central crystal. The "nine" energy for a central crystal (E_9) was the sum of the energy deposit in the central crystal and its eight adjacent crystals. However, if a crystal was adjacent to more than one central crystal (C,D,E in Figure 5.2) then only a fraction of the energy deposit was added, where the fraction was defined by the relative magnitudes of the central crystal energy deposits.

Therefore, the nine energy for a central crystal k was calculated by

$$E_{9k} = E_k + \sum_i E_i + \frac{E_k}{\sum_l E_l} \sum_j E_j \quad , \tag{5.5}$$

where i is the index of any crystal adjacent to only central crystal k, j is the index of a crystal adjacent to two or more central crystals with index l of which k is included and E is the energy deposit in a crystal. To find the fraction of the total cluster energy to be assigned to each PED, the nine energy of each central crystal was used in

$$E_{PED}^k = \frac{E_{9k}}{\sum_l E_{9l}} E_{cluster}^{total} \quad , \tag{5.6}$$

where k is one central crystal index included in the l central crystal indexes and $E_{cluster}^{total}$ is the energy of the entire cluster. Like clusters with only one local maximum, these PED energies must have exceeded 20 MeV to be considered a particle.

Due to aluminum support structure and shower leakage at the edge of the calorimeter, an additional correction must be made to the PED energy. These effects have been found to vary with polar angle and PED energy. Therefore, a correction function of the form [28]

$$E_{PED}^{corr} = \left(a(\theta) + b(\theta) \, e^{-c(\theta) \, E_{PED}} \right) E_{PED} \tag{5.7}$$

was applied. Typical values for these parameters are $a \approx 1.05$, $b \approx 0.05$, and $c \approx 0.007$ and were determined by comparing to Monte Carlo simulations.

The position reconstruction was done very similarly for the CB detector as for the TAPS detector. By using a weighted sum over crystals in the cluster, the PED angles were reconstructed using

$$\phi_{PED} = \frac{\sum_i w_i \phi_i}{\sum_i w_i} \qquad \theta_{PED} = \frac{\sum_i w_i \theta_i}{\sum_i w_i} \quad , \tag{5.8}$$

where i is the index of a crystal in the cluster and w_i is defined by Equation 5.2. For the CB reconstruction, the parameter W_0 has been changed to $W_0 = 4.25$, which optimized reconstruction of CB photons in the Monte Carlo simulations. In the case of clusters where more than one PED has been reconstructed, only the crystals used for the central crystal's nine energy (Equation 5.5) were used for position reconstruction.

This method of position reconstruction had a spatial resolution of 1-1.5° in both ϕ_{PED} and θ_{PED} [29]. Since all CB crystals have their long axis pointed at the target and photons entered the crystals perpendicularly, a shower depth correction was not needed.

For a PED to be marked as charged, the inner detector had to register a hit in at least two of three scintillator layers within 30° of the reconstructed PED position relative to the target center. Due to the configuration of the inner detector scintillating fibers, a unique position could be reconstructed using a hit in two layers. By assuming the charged particle originated in the center of the target, the angular position of the detected charged particle was estimated. If this angular position was close enough, then the particle is marked as a charged particle.

CHAPTER 6

REACTION SELECTION

The selection of recorded data events which resulted from the desired hadronic reaction is called reaction selection. To select for the $\gamma p \to p\omega$ and $\gamma p \to p\pi^0\omega$ reactions, we must consider what particles to look for. The ω and π^0 mesons decay very quickly after being formed, decaying to the modes listed in Table 6.1.

Table 6.1: π^0 and ω Meson Branching Fractions. Values from [1]. The fraction of the time each meson decays to the listed decay mode.

Meson	Decay Mode	Branching Fraction
π^0	$\gamma\gamma$	$(98.823 \pm 0.034)\%$
	$e^+ \, e^- \, \gamma$	$(1.174 \pm 0.035)\%$
ω	$\pi^+ \, \pi^- \pi^0$	$(89.2 \pm 0.7)\%$
	$\pi^0 \gamma$	$(8.28 \pm 0.28)\%$
	$\pi^+ \, \pi^-$	$(1.53^{+0.11}_{-0.13})\%$

For all plots and discussions in this chapter, the units used are those where the speed of light c is set to $c = 1$. This means energy, momentum, and mass have the same units, electron volts (eV).

The π^0 and ω meson decay modes detectable using the CBELSA/TAPS experimental setup are

$$\pi^0 \to \gamma\gamma \quad \text{and} \quad \omega \to \pi^0\gamma \to \gamma\gamma\gamma \quad , \tag{6.1}$$

due to the experimental setup's ability to detect photons. The branching fractions for the decays being selected are shown in Table 6.1. Therefore, the decay chains selected in this analysis are

$$p\omega \to p\pi^0\gamma \to p\gamma\gamma\gamma \quad \text{and} \quad p\pi^0\omega \to p\pi^0\pi^0\gamma \to p\gamma\gamma\gamma\gamma\gamma \quad . \tag{6.2}$$

Since the detection of protons was not essential to the reconstruction of the event, the number of charged particles reconstructed did not matter as long as there are less than 2. Therefore for the reaction $\gamma p \to p\omega$ ($\gamma p \to p\pi^0\omega$), all recorded events in the dataset with 3(5) uncharged PEDs[1] and less than 2 charged PEDs were selected for

---

[1]Particle Energy Deposits

further analysis. The uncharged PEDs were assumed to be photons and the charged PEDs are assumed to be protons until a more sophisticated method for checking can be applied (kinematic fitting Section 6.2.3).

The selected events were then reduced further by making kinematic cuts (Section 6.2). To tune these kinematic cuts and to estimate how many events this analysis did not detect, these final states were simulated in a Monte Carlo Simulation program (described in the next section). After these kinematic cuts, there are still unwanted events present in the data which are from other reactions (background events). There is no way to cut these events out of the analysis without losing too many of the desired signal events. Therefore, the remaining events were subjected to an analysis technique which assigns a probability that it is a signal event (Q-factor). This Q-factor is then used to weight each event when measuring an observable to effectively subtract the background events (Q-factor method - Section 6.4).

The reaction selection for the $\gamma p \rightarrow p\omega$ analysis and $\gamma p \rightarrow p\pi^0\omega$ analysis were very similar and are discussed in parallel as much as possible.

6.1   Monte Carlo Simulations

In order to understand the response of the detector systems and the effect of kinematic cuts to these final states, the experiment was modeled in GEANT3 Monte Carlo simulations. Events were simulated using the GEANT3 based CBGEANT [30] simulation package. The simulated events were generated from threshold to 3.175 GeV in initial photon energy. The software begins an event by placing the final state particle in the target cell. The initial momenta were assigned by random number generators within the allowed kinematic phase space, while taking into account energy and momentum conservation. In small steps, the particles were allowed to propagate, decay, and interact with modeled support structures, scintillators and crystals. In the case of the neutral mesons (ω and π^0), these were allowed to decay according to the known parameters. The known electromagnetic response of the detectors and support structures to photons and protons were used to simulate experimental detector output. Simulated detector output was put into the same format as the experimental detector output so simulated data can be treated in exactly the same way as measured experimental data. To ensure the software was simulating the events correctly, the simulation output was compared to experimental data to check for corrections and quality checks.

These Monte Carlo simulations were done for two different reasons. These reasons are: 1) to guide the search for kinematic cuts which will not eliminate many of the desired signal events, and 2) estimate how many events were not seen by the analysis (i.e. detector acceptance).

The tuning of kinematic cuts was done by subjecting the simulated events to the same reconstruction and kinematic cuts as experimental data. In this way, kinematic

53

cuts which resulted in too much of the desired signal events being dropped from the analysis were not used.

Also after these simulated events were subjected to the same analysis as the experimental events, the number of reconstructed simulated events were compared to the number of simulated events which were originally generated. This comparison gives the probability a signal event is actually detected and counted by the analysis. Or equivalently, an estimate of how often the analysis did not detect a signal event. This ratio defines the detector acceptance which is used in the measurement of the differential cross sections.

6.2   Data Reduction Cuts

This section describes the data cuts used in selecting the events with $p\pi^0\gamma$ or $p\pi^0\pi^0\gamma$ final states. The reason for selecting the $p\pi^0\gamma$ and $p\pi^0\pi^0\gamma$ final states instead of fitting to the ultimate final states $p\omega$ and $p\pi^0\omega$ is due to the size of the natural mass width of the ω meson (8.49 MeV/c^2 [1]). This mass width is comparable to the experimental setup's uncertainty in reconstructing the ω meson invariant mass (≈ 20 MeV). Kinematic fitting is a method of evaluating how well an event's measured values match an ideally measured event of the desired final state. This is done by defining constraints such as energy and momentum conservation and invariant masses of the final state particles. If the ω meson invariant mass is used in defining a constraint, the fitting of a set of measured values to "ideal" values would have no meaning since the Heisenberg Uncertainty Principle indicates there are no ideal values for this reaction. To avoid this issue, the π^0 meson invariant mass with a mass width of ~ 8 eV was used as a constraint and the ω meson contributions were isolated through the Q-factor method of background subtraction.

The data used in the analysis of both $\gamma p \to p\omega$ and $\gamma p \to p\pi^0\omega$ for the purposes of measuring differential cross sections and unpolarized spin-density matrix elements were taken during October and November 2002. An ELSA accelerator electron beam with energy 3.175 GeV was used to create an unpolarized photon beam incident upon a liquid hydrogen target.

6.2.1   Tagger Time Cut

When a photon encounters a proton, the probability to get the desired hadronic reaction is quite small. To make the measurements required to isolate the "missing" baryon resonances, thousands of reactions must be measured. To measure this number of events in a reasonable amount of time, the current of photons interacting with the target must be large. The large current causes many photons to be detected in the tagger which could have been the initial photon. To reduce the number of initial photon candidates which caused the production of the particles detected in the calorimeters, a timing cut is used.
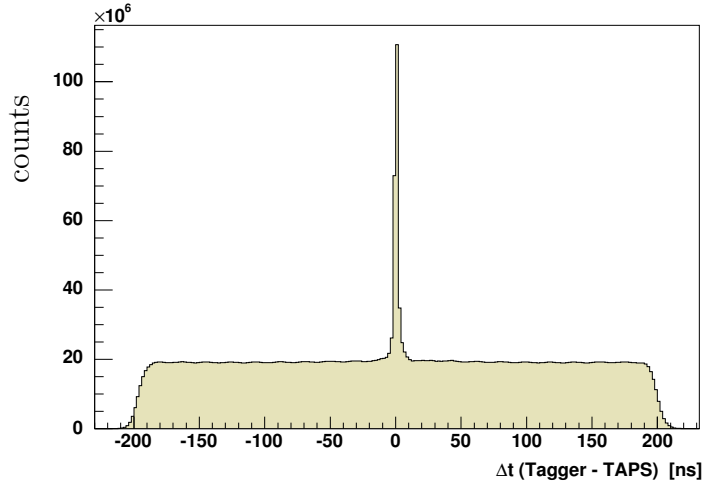
Figure 6.1: Tagger Photon Timing Spectrum. Timing spectrum of initial state photons with respect to the time calibration (Section 4.1) integrated over all the data. Only photons which had a time within ±3 ns were taken as initial state photon candidates.

The timing of each photon is measured with respect to particles detected in the TAPS detector. The TAPS detector has the best characteristics for providing timing information. Figure 6.1 shows the timing spectrum of the initial photons with respect to the timing calibration (Section 4.1). The peak in this figure shows timing information for the photons which most likely caused the production of particles detected in the TAPS detector. However, there exists a large number of photons which fall outside this peak and also exist underneath the peak (accidental background). These background photons are beam photons which did not produce the TAPS particles. The width of the peak shows the timing resolution of the timing measurement.

To help isolate which initial photon caused the reaction, a cut on the initial photons was made with respect to time. If at least one photon was detected in TAPS, only photons having a time ±3 ns relative to the time calibration were retained as initial photon candidates. If only a charged particle were detected in TAPS, then the timing window for the initial photon was increased to -5 to 15 ns relative to the time calibration. This wider cut reflects the fact that protons travel much slower than photons and due to the much smaller energy deposit causes a larger uncertainty in the timing information. This cut typically reduced the number of photon candidates from tens of photons to less than 3 for each event. To decide which remaining photon to use, the kinematic fitting method in Section 6.2.3 was used.

The background distribution in Figure 6.1 suggests the data set contains accidental background events which will be difficult to cut out and could potentially cause the measurement to be overestimated. To subtract this background contribution, a timing background analysis of events lying outside the timing window was done and

55

subtracted from the events inside. The timing requirement for the timing background events is -53 ns $< t_{TB} < -50$ ns and 50 ns $< t_{TB} < 53$ ns. The timing background subtraction is discussed further in Section 6.6.

6.2.2 Coplanarity Cut

For reactions with a charged particle detected within the timing window, an additional constraint was used to ensure the momentum in the plane perpendicular to the beamline was conserved. This cut helped to eliminate undesired background events by reducing the possibility of an undetected particle being involved in the reaction.

To define the cut, the reconstructed momentum of all photons (uncharged PEDs) were added to define a vector in the plane perpendicular to the beamline and was compared to the detected position of the proton (charged PED). Theoretically if this event involved nothing but the detected photons and the detected proton, the angle between these two vectors should have been $180°$. To cut events which deviate from this, any event with a detected charged particle that had an angle between these two vectors not within $180 \pm 30°$ were dropped from the analysis.

6.2.3 Kinematic Fitting Cut

To remove more of the undesired contributions and to isolate the correct initial state photon for an event, kinematic fitting was used to define a probability each event left in the analysis was the $p\pi^0\gamma$ or $p\pi^0\pi^0\gamma$ final state. The reconstructed photon energies and positions have small errors due to measurement uncertainties. A kinematic fit varies the measured quantities within the quoted errors of the experimental setup to match energy-momentum conservation and invariant mass constraints using a χ^2 minimization technique. The result of the fit is a χ^2 probability or confidence level value which is an estimate of the event's likelihood of fulfilling the constraints and therefore the likelihood of this event being the desired reaction.

For an event with multiple initial state photon candidates, all of the candidates are used as the initial photon in separate kinematic fits. The candidate which had the highest probability of fulfilling the energy and momentum conservation constraints was taken as the initial photon for an event.

Kinematic Fitting. If the n measured energies and angles of the particles are used in a n-dimensional vector $\vec{y}$ and the theoretically exact energies and angles of the detected particles are contained in the n-dimensional vector $\vec{\eta}$, then they relate to each other according to

$$\vec{y} = \vec{\eta} + \vec{\epsilon} \quad , \tag{6.3}$$

where $\vec{\epsilon}$ is a n-dimensional vector of the error in the measurement.

The constraints in the form of conservation laws and invariant masses can be used to deduce r number of unmeasured quantities, as long as the number of constraints m is larger than or equal to the r number of unmeasured quantities. If $\vec{x}$ is the r-dimensional vector of unmeasured quantities to be deduced, then the constraints can

56

be written as

$$f(\vec{x}, \vec{\eta}) = f(\vec{x}, \vec{y} - \vec{\epsilon}) = 0 \quad , \tag{6.4}$$

where $\vec{\epsilon}$ are the errors which are allowed to vary to fulfill the constraints. This set of constraints are referred to as the *fit hypothesis*.

The solution for $\vec{\epsilon}$ are the values which minimize

$$M = \vec{\epsilon}^T C_y^{-1} \vec{\epsilon} \tag{6.5}$$

while the constraints are fulfilled exactly, where C_y^{-1} is the covariance matrix which contains the quoted uncertainties of the measurements in $\vec{y}$.

The events to be reconstructed for the reaction $\gamma p \to p\omega$ were fitted to the $p\pi^0\gamma$ final state and the events to be reconstructed for the reaction $\gamma p \to p\pi^0\omega$ were fitted to the $p\pi^0\pi^0\gamma$ final state. In each case, the measured values were fitted by disregarding the charged particle information and fitting to a missing proton. In this way, the kinematic fitter will evaluate how well the measured event values match the fitted or ideal event values.

If no systematic errors are present and the event is the final state which defined the constraints, the difference between the ideal/fitted value (η_i) and the measured value (y_i) when averaged over many events should be zero. This is because the measurement error should be random and the error ϵ_i for a measurement has the same likelihood to be negative as positive. If this distribution is normalized according to

$$\text{pull}(y_i) = \frac{\eta_i - y_i}{\sqrt{\sigma^2(\eta_i) + \sigma^2(y_i)}} \quad , \tag{6.6}$$

it is referred to as a *pull*. A distribution of pulls should have a Gaussian width of 1 if the errors $\sqrt{\sigma^2}$ are set correctly. If the width is smaller (larger) than one, then the errors defined in the covariance matrix C_y have been determined too large (small). These errors are related to the granularity of the crystals and the natural uncertainty with which the detectors measure.

Figures 6.2 and 6.3 show the distribution of pulls separated for which detector the photon was detected in. The values used are the square root of the energy of the final state photons (γ Energy), the polar angle ($\gamma \theta$) with respect to the beamline, and the azimuthal angle ($\gamma \phi$) with respect to the beamline. These pulls are shown for photons detected in each detector. Since the information on charged particles were ignored during kinematic fitting, pulls are only generated for photons. Each plot is labeled with the parameters extracted from a fit of a Gaussian function fit.

The slightly unsymmetric shape and corresponding shift of the mean of the γ Energy pulls are due to the fact that crystal modules do not record photon energy values below 30 MeV and correspond to a lack of events of the low energy side of each pull distribution. The low energy behavior for the TAPS and CB photons cause the high energy behavior of the initial photons. This effect in the $p\pi^0\pi^0\gamma$ pull distributions is smaller due to the proportion of higher energy photons which are not close to the 30 MeV threshold.

57
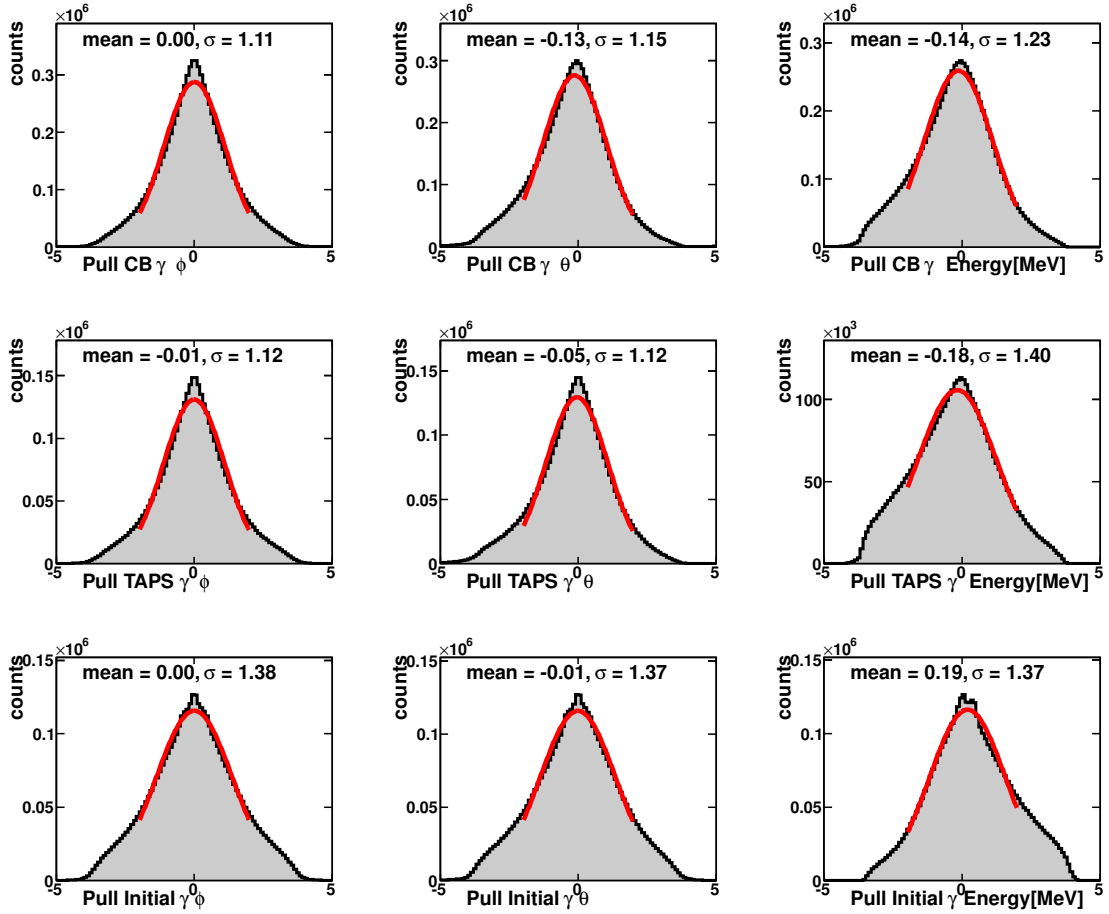
Figure 6.2: $p\pi^0\gamma$ Experimental Data Pull Distributions. The pulls are separated according to which detector the photon was detected in for the Crystal Barrel (CB, top row) and TAPS (middle row). Initial photons (bottom row) are for photons that were tagged in the tagging hodoscope. The mean and sigma parameters are from a fit of the data to a Gaussian function from -2 to 2.
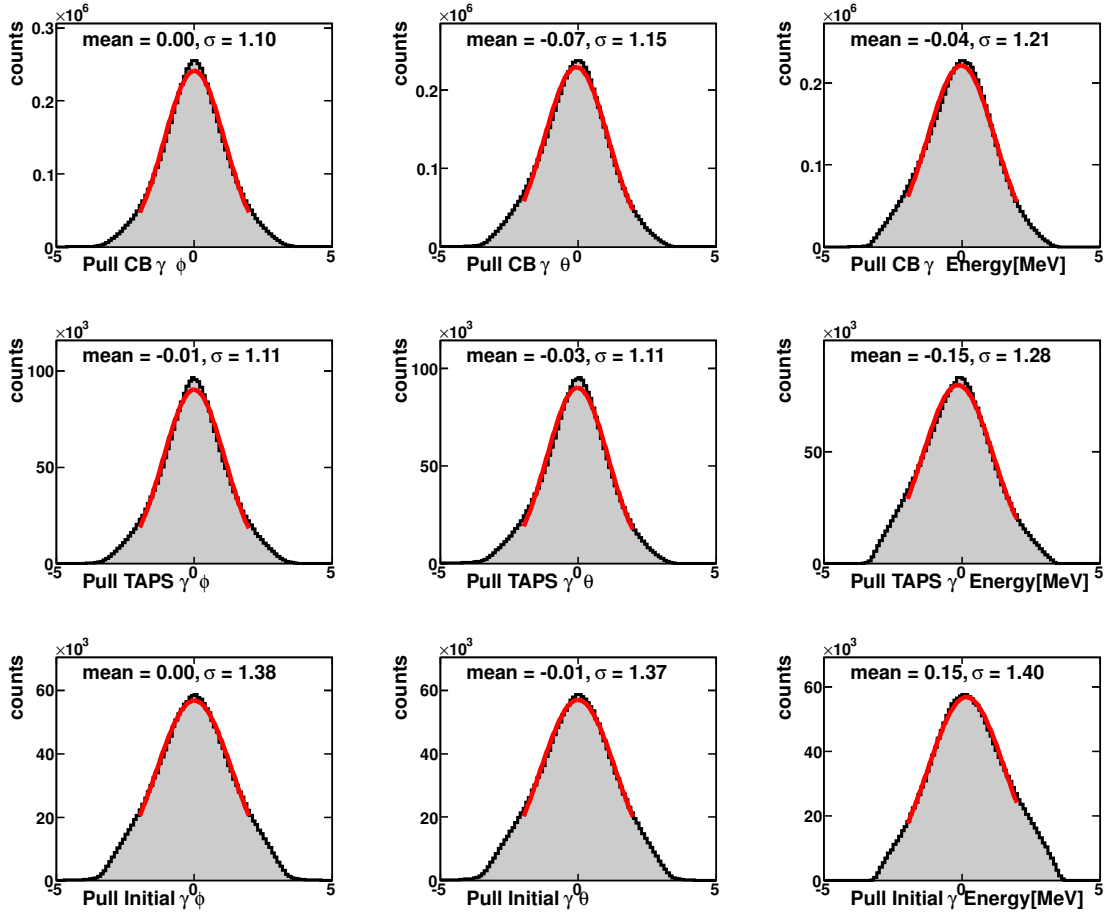
Figure 6.3: $p\pi^0\pi^0\gamma$ Experimental Data Pull Distributions. The pulls are separated according to which detector the photon was detected in for the Crystal Barrel (CB, top row) and TAPS (middle row). Initial photons (bottom row) are for photons which were tagged in the tagging hodoscope. The mean and sigma parameters are from a fit of the data to a Gaussian function from -2 to 2.
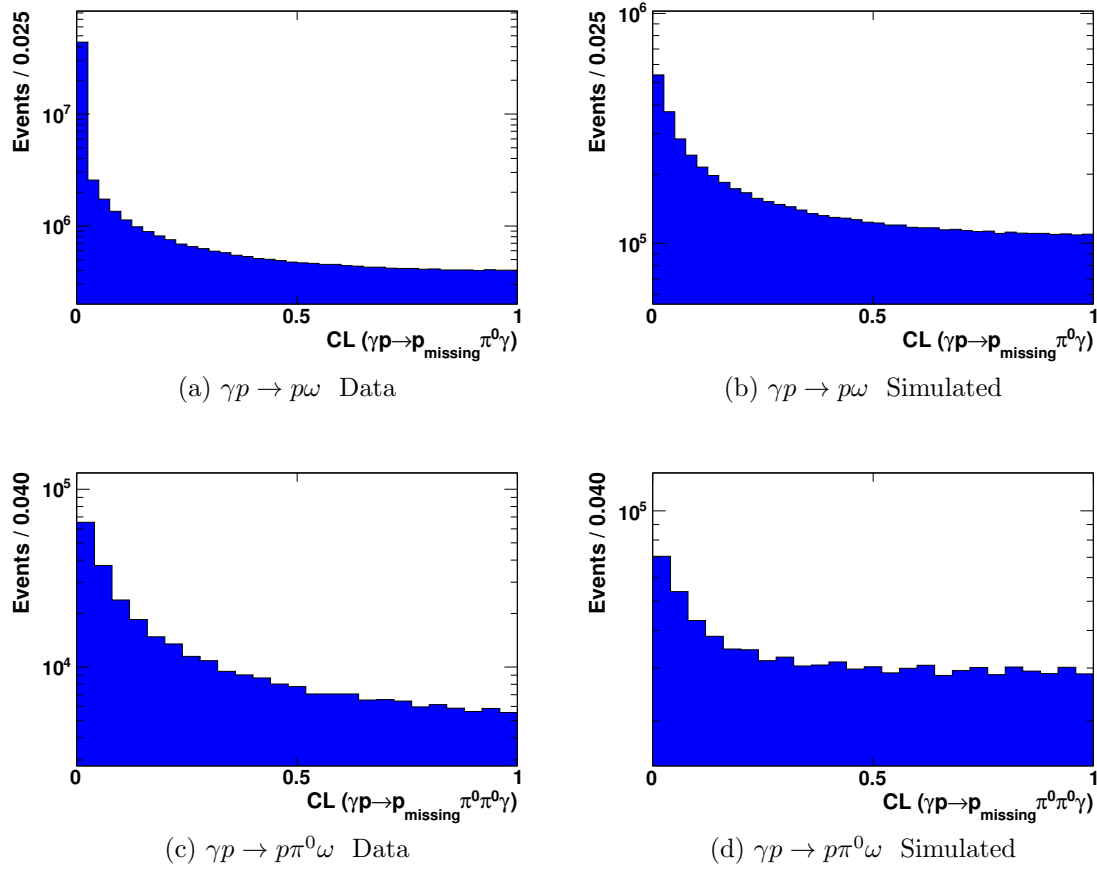
Figure 6.4: Confidence Level Distributions.

Overall, the values for mean and width (σ) vary from the ideal values, but are within the accepted uncertainty for this measurement.

A confidence level value is a number which indicates how well the measured values of an event match the corresponding values for an ideal event of the desired final state. The values range from 0 to 1, where 1 indicates the event's measured values exactly matched the desired final state. The distribution of confidence level values of a set of events which match the constraints should be flat. The distribution for signal events should be dictated completely by the distribution of the errors in measurement with respect to the quoted errors given in the covariance matrix C_y. If these errors are set correctly, these signal events are distributed evenly in the confidence level distribution. However, any background event or incorrectly reconstructed event should have a confidence level closer to zero due to its inability to match the constraints.

Kinematic fits were done on all experimentally measured and Monte Carlo simulated events which passed the timing cuts. The resultant confidence level distributions are shown in Figure 6.4. The resulting CL distributions for experimentally measured

60

data events (Figure 6.4 Left) and Monte Carlo simulated events (Figure 6.4 Right) are sufficiently flat for confidence level values above 0.6 to use for kinematic cuts. The large rise in the distribution of events for small confidence level (left side of each plot in Figure 6.4) is due to background events or events which were reconstructed incorrectly (e.g. wrong initial photon being isolated).

Confidence Level Cut. To correctly model the effect of a confidence level cut in the detector acceptance analysis, experimental data and Monte Carlo simulated events must be treated exactly the same way. To ensure a confidence level cut treats both types of events the same way, the confidence level distributions must behave the same way for these two types of events. According to the properties of the confidence level value, the region where these true $p\pi^0\gamma$ and $p\pi^0\pi^0\gamma$ events dominate the distribution are those close to 1. The confidence level distributions in Figure 6.4 for Monte Carlo simulated events and experimentally measured data are sufficiently similar for confidence level levels above about 0.6 to believe true $p\pi^0\gamma$ and $p\pi^0\pi^0\gamma$ events are being treated the same way.

The biggest advantage of using kinematic fitting is the reconstruction of the π^0 mesons among the detected photons. This identification is very useful later on in the opening angle cut (Section 6.2.4). However, the confidence level gives us a prime opportunity to reduce the number of unwanted background events while preserving as many signal events as possible. The confidence level distributions in Figure 6.4 show a large increase to the left of each plot, which correspond to a large number of background events. If a data reduction cut is defined using a low value of confidence level, a large fraction of the background events can be cut out of the analysis while keeping most the signal events. For an event to be kept in the analysis, the event had to have

$$CL_{p_{missing}\pi^0\gamma} > 0.005 \tag{6.7}$$

for the events to be reconstructed for the $\gamma p \rightarrow p\omega$ analysis and

$$CL_{p_{missing}\pi^0\pi^0\gamma} > 0.005 \tag{6.8}$$

for the events to be reconstructed for the $\gamma p \rightarrow p\pi^0\omega$ analysis. The effect of the remaining background events will be removed using the Q-factor fitting method.

6.2.4 Opening Angle Cut

When the ω meson decays to $\pi^0\gamma$, energy is left over after forming the π^0. This energy is realized as momentum. Therefore at the center-of-mass energies typical in this analysis, a large opening angle is formed between the π^0 meson and the photon in the center-of-mass frame. To illustrate this point, the π^0 and the photon were reconstructed from Monte Carlo simulated events and the opening angle ($\theta_{\pi^0,\gamma}$) in the center of mass frame is plotted versus the momentum of the resulting candidate ω meson ($|p_{c.m.}^\omega|$). The resulting distribution is plotted in Figure 6.5a. The same plot for the experimentally measured data events (Figure 6.5b) shows features which

differ from the simulated data. To determine where the extra contributions at high momentum and $\theta_{\pi^0,\gamma} \sim 150°$ are coming from, Monte Carlo simulated $p\pi^0$ events were generated and reconstructed using the same reconstruction and reaction selection as the $p\omega$ events. The distribution of events for these events are shown in Figure 6.5c. The distribution in Figure 6.5c has the same structure as the extra contributions in Figure 6.5b. Therefore, a sizable contribution from $p\pi^0$ events which were poorly reconstructed as $p\pi^0\gamma$ exists.

To minimize the $p\pi^0$ background events with values in the extra peak in Figure 6.5b, events which satisfy

$$|p_{c.m.}^{\omega}| \geq (-13.33\, \theta_{\pi^0,\gamma} + 2400) \text{ MeV}/c \tag{6.9}$$

are dropped from the $\gamma p \to p\omega$ analysis. The threshold for the cut in Equation 6.9 is shown in Figure 6.5 as a black line. All events with values above this line have been dropped from the $\gamma p \to p\omega$ analysis.

There are other background contributions which exist in the experimental data, but are not as easily removed using a similar type of cut. These other background types are further subtracted using the Q-factor background subtraction technique (Section 6.4.1).

The opening angle spectrum for the events selected for $\gamma p \to p\pi^0\omega$ are shown in Figure 6.6. The characteristic opening angle again can be seen in the distributions. But unlike the $\gamma p \to p\omega$ experimental data, there are no extra peak-like structures which differ from the simulated data. However we do see a different distribution of events away from the characteristic opening angle, but this is due to some background events. Rather than define a cut using opening angle values, we rely on the Q-factor background subtraction to remove the extra contributions. No opening angle cuts were applied in the $\gamma p \to p\pi^0\omega$ analysis.

6.2.5 Trigger Condition Cut

When a proton encounters the crystals of the TAPS detector, it can do one of two things. The proton can get stuck in the crystal or, if it has enough momentum, it can pass through the whole crystal. As the proton passes through the crystal, it transfers some of its kinetic energy to the crystal. If the proton gets stuck in the crystal, all the kinetic energy is transferred. As the proton interacts with the crystal, many different processes happen which do not happen when a photon interacts with the crystal. The protons interact with the nuclei in the crystal atoms to convert the kinetic energy in ways which are not modeled well in the Monte Carlo GEANT3 software.

The energy deposit of protons in this analysis are typically ignored. The proton's energy and momentum were reconstructed by the missing mass kinematic fit. However, the trigger (i.e. decision to record an event (Section 3.6.3)) also responds to protons. To correctly estimate the detector acceptance, the probability that a proton recorded an energy deposit above the LED-low and LED-high thresholds (Section

(a) $\gamma p \to p\omega$ Simulated Data Events

(b) $\gamma p \to p\omega$ Experimental Data Events

(c) $p\pi^0$ Simulated Events
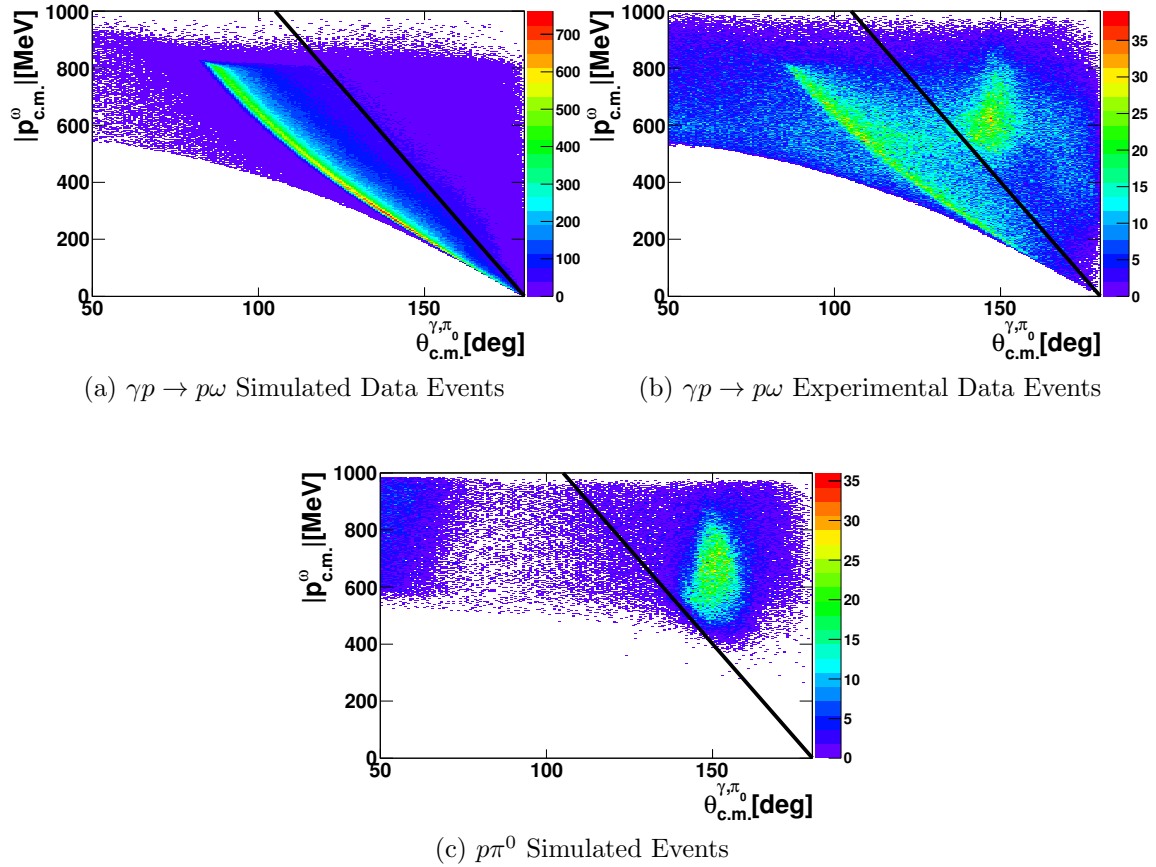
Figure 6.5: Opening Angle Spectrum for $\gamma p \to p\omega$ Events. All events in each plot were subjected to the confidence level cut in Equation 6.7. The π^0 meson and the photon were reconstructed by the kinematic fitter. The opening angle $(\theta_{\pi^0,\gamma})$ is measured in the center-of-mass frame. The black line in each plot is the cut threshold defined by Equation 6.9. All events with values above this line are eliminated from the analysis.

3.6.1) must be modeled correctly, for all proton momenta. The limitations of the simulation software causes the detector acceptance correction to have small errors from not being able to model the response of these trigger thresholds to protons. However when the energy of the initial photon rises above 1600 MeV, the higher momentum proton reliably triggers independently of the modeled energy.

This issue only occurs when Condition A is met in the trigger. Condition A requires at least two LED-low segments with each segment having at least one signal above the LED-low threshold. If one of these two signals is the proton, the simulation does not agree with the experiment (if initial photon energy is below 1600 MeV). Condition B requires at least one LED-high segment with a signal above the LED-

63

(a) $\gamma p \to p\pi^0\omega$ Data   (b) $\gamma p \to p\pi^0\omega$ Simulated
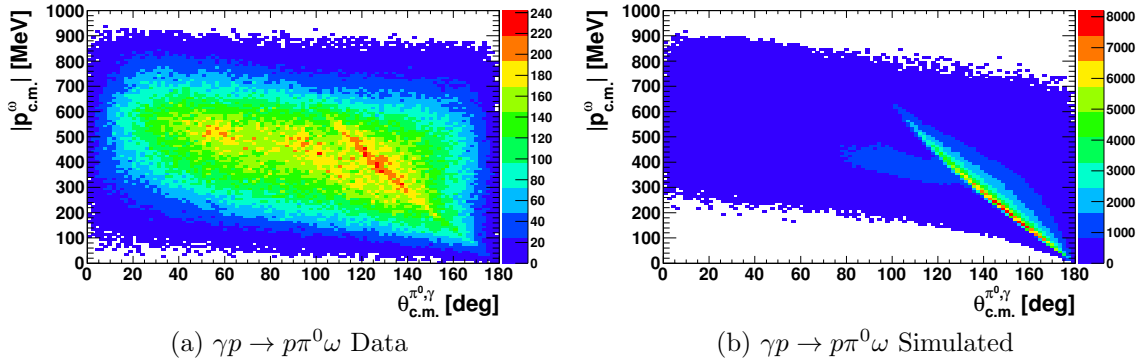
Figure 6.6: Opening Angle Spectrum for $\gamma p \to p\pi^0\omega$ Events. The π^0 meson and the photon were reconstructed by the kinematic fitter. The opening angle ($\theta_{\pi^0,\gamma}$) is measured in the center of mass frame.

high threshold. If this one signal is the proton, the proton has shown to trigger reliably enough to not affect the detector acceptance.

The kinematics of the reactions in this analysis are diverse enough to eliminate this issue without a loss in angular acceptance. All events with a proton reconstructed in the TAPS detector, fulfilling trigger condition A, no photons in TAPS above the LED high threshold (which would fulfill Condition B), and with an initial photon energy below 1600 MeV are eliminated from the analysis. Both experimentally measured and simulated events were subject to this cut. This cut was used in both the $\gamma p \to p\omega$ and $\gamma p \to p\pi^0\omega$ analyses.

6.3   Invariant Mass Spectrum After Initial Cuts

Figure 6.7 shows the ω invariant mass peaks occurring in the $\pi^0\gamma$ invariant mass distributions in the events remaining after the initial kinematic cuts discussed in Section 6.2. The experimental data plots (Figures 6.7a and 6.7c) still have a sizable amount of background underneath each peak. This data consists of other reactions which by chance have matched the selection for the signal events. For events selected for the $\gamma p \to p\pi^0\omega$ analysis, there also exists a combinatorial background which comes from the two different ways a $\pi^0\gamma$ combination can be made from $p\pi^0\pi^0\gamma$. At most, there can be only one combination which contributes to the peak. The other combination contributes to the background distribution.

This background could not be eliminated using the data reduction cuts, because those same cuts also cause signal events to be dropped from the analysis. In order to have enough signal to make an observable measurement required to isolate "missing" baryon resonances, a maximum amount of signal must be preserved in the data. The

(a) $\gamma p \to p\omega$ Data

(b) $\gamma p \to p\omega$ Simulated

(c) $\gamma p \to p\pi^0\omega$ Data

(d) $\gamma p \to p\pi^0\omega$ Simulated
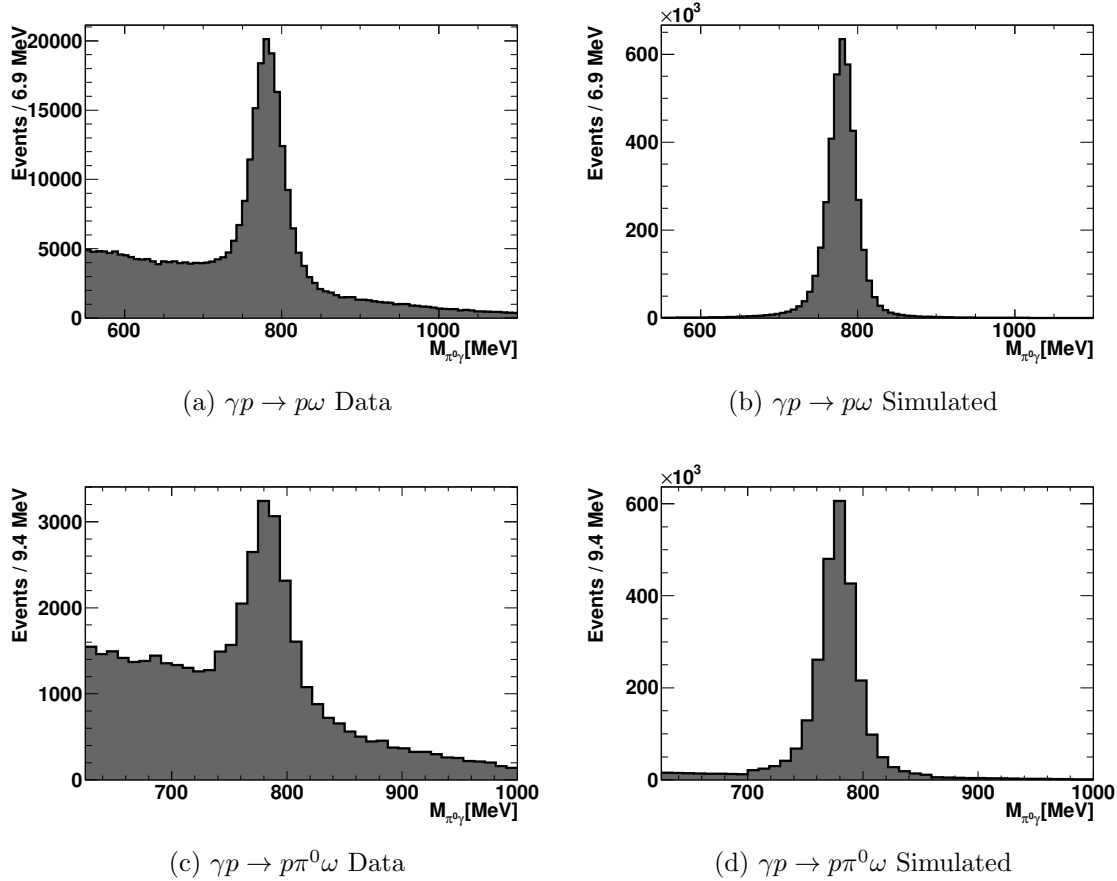
Figure 6.7: Invariant Mass Spectrum After Initial Cuts.   In the plots for the reaction $\gamma p \to p\pi^0\omega$, two contributions from each event are represented due the two combinations of $\pi^0\gamma$ obtained from the $p\pi^0\pi^0\gamma$ final state.

data reduction cuts were chosen such that a large fraction of background events were dropped from the analysis while keeping as many signal events as possible.

To finally isolate the effect of these signal events, we subtract the effect of the background events or, in other words, count the number of signal events in each peak in Figure 6.7 and apply that to the observable. To report a value for an observable in every kinematic bin, this counting/subtraction must be done in each kinematic bin. For this analysis, this is done by using the Q-factor method of background subtraction. A Q-factor is a value which defines the probability an event is a signal event. When doing the counting to measure an observable in a kinematic bin, the Q-factor value for each event in the kinematic bin is summed over. The method for defining this Q-factor is discussed in the next section.

Since Figure 6.7b has no visible background, no background subtraction was needed for the Monte Carlo simulated $\gamma p \to p\omega$ events. However, all other event

65

Table 6.2: Kinematic Variables used in the Q-factor Method. For definitions of symbols in this table, see Section 7.1.1.

Analysis	Kinematic Variables
$\gamma p \rightarrow p\omega$	$\sqrt{s}, \cos\theta_\omega^{c.m.}, \phi_\omega^{c.m.}$
$\gamma p \rightarrow p\pi^0\omega$	$\sqrt{s}, \cos\theta_\omega^{c.m.}, \phi_\omega^{c.m.}, M_{p\pi^0}, \cos\theta_{\pi^0}^*, \phi_{\pi^0}^*$

types were background subtracted and are discussed in the next section.

6.4 Event-based Background Subtraction (Q-factor Method)

As a result of the kinematic cuts detailed in Section 6.2, the contributions from $p\pi^0\gamma$ ($p\pi^0\pi^0\gamma$) final state events which were not $p\omega$ ($p\pi^0\omega$) final state events must be subtracted. These background contributions were subtracted using an event-based probabilistic weighting method outlined in [31] (Q-factor Method). The result of this method is to define a Q-factor for each event in an analysis. The Q-factor is the probability that an event is a signal event. To subtract the contribution of the background, the events in the analysis are weighted with this Q-factor.

This method has advantages which include

- preserving the possibility of an event-based interpretation analysis, and

- better systematic error characteristics in low statistics data sets.

An event based interpretation analysis is an analysis, like a partial wave analysis, where the data for an observable is considered event by event instead of grouping the data in a kinematic bin and considering them as a set. The improvement in systematic error characteristics come about because the number of events used in determining background contributions is not connected to the size of each kinematic bin in the analysis.

To define an event's Q-factor, the events were considered in the final state reaction's kinematic phase space. The kinematic variables defined for the Q-factor method processing are shown in Table 6.2. To deduce information about the behavior of signal and background distributions at a particular point in the kinematic phase space, the events closest to that point in kinematic phase space were used. The distance in a multi-dimensional space can be calculated between event A and event B by

$$D_{A,B} = \sqrt{\sum_i \left(\frac{\chi_i^A - \chi_i^B}{\sigma_i}\right)^2} \quad , \tag{6.10}$$

where i is the index of the kinematic variables in the kinematic phase space, χ is the kinematic variable and σ_i is the range of the kinematic variable. To illustrate

66

this, Figure 6.8 illustrates the nearest neighbor events close to a seed event (the event which the Q-factor will be defined for).
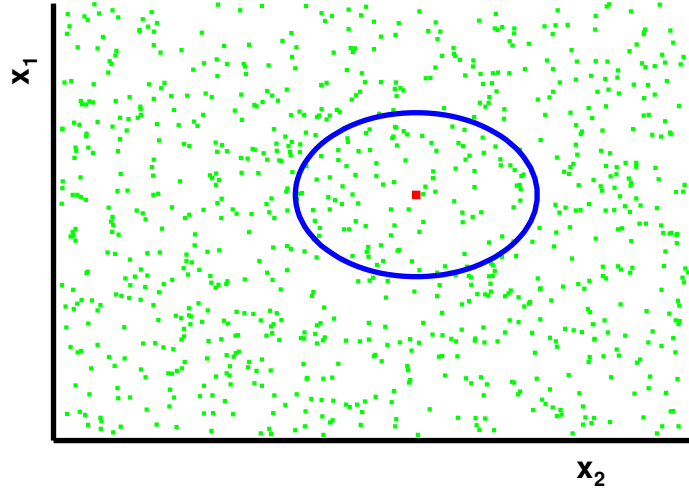
Figure 6.8: Q-factor Method Cartoon. x_1 and x_2 represent kinematic variables which define a kinematic phase space. The dots represent the position of events in the phase space. The ■ represents the seed event or the event for which a Q-factor is being defined for. The circle highlights the events which will be used to define the background and signal characteristics at the seed event's point in kinematic phase space (Nearest Neighbors).

To find the background and signal distributions for an event's point in phase space, the nearest neighbors were used to form an invariant mass distribution. Enough nearest neighbors should be used to ensure a good representation of the data (i.e. ensure a good fit of the data). In these analyses, the ω meson was used as the particle to identify in the invariant mass distributions. Figure 6.9 shows how a typical invariant mass distribution looks. The next step was to define the contributions of the signal and background events by fitting them to functions which describe their line shapes. The signal line shape was defined by a Voigt function. The Voigt function is a convolution of a Gaussian function, used to describe the peak width due to measurement uncertainties, and a Breit-Wigner function, used to describe the natural line shape of a resonance. The background function is a function which describes a smooth non-peaking distribution which lies underneath the peak. For these analyses, the total function combining the background ($B(x)$) and signal functions ($S(x)$) was defined as

$$f(x) = N \left[f_s S(x) + (1 - f_s) B(x) \right] \quad , \tag{6.11}$$

67

Figure 6.9: Q-factor Illustrated. The data in the plot are from the seed event's nearest neighbor events. The ━ is the fit of the total function (signal + background). The ▬▬▬ is the background function. s is the signal function value and b is the background functions value at the value of the seed event's invariant mass.

where N is a normalization constant and f_s is the signal fraction. The signal fraction is a parameter between 0 and 1 which defines the relative amplitude of the background and signal functions.

The fit procedure was done using the Roofit package [32] in the CERN ROOT software package. The fitting of parameters was done by using an unbinned maximum likelihood fit.

The Q-factor (Q) was defined as

$$Q = \frac{s(X)}{s(X) + b(X)} \quad , \tag{6.12}$$

where X is the seed event's invariant mass value, s is defined as

$$s(X) = f_s S(X) \quad , \tag{6.13}$$

b is defined as

$$b(X) = (1 - f_s)B(X) \quad , \tag{6.14}$$

and illustrated in Figure 6.9.

6.4.1 $\gamma p \to p\omega$ Background Subtraction

In Figure 6.7a, the experimentally measured data selected for $p\pi^0\gamma$ have a peak in the $\pi^0\gamma$ invariant mass corresponding to the ω meson. To isolate the contribution

68

(a) Low Energy Fit $E_\gamma \approx 1125$ MeV (b) High Energy Fit $E_\gamma \approx 2475$ MeV
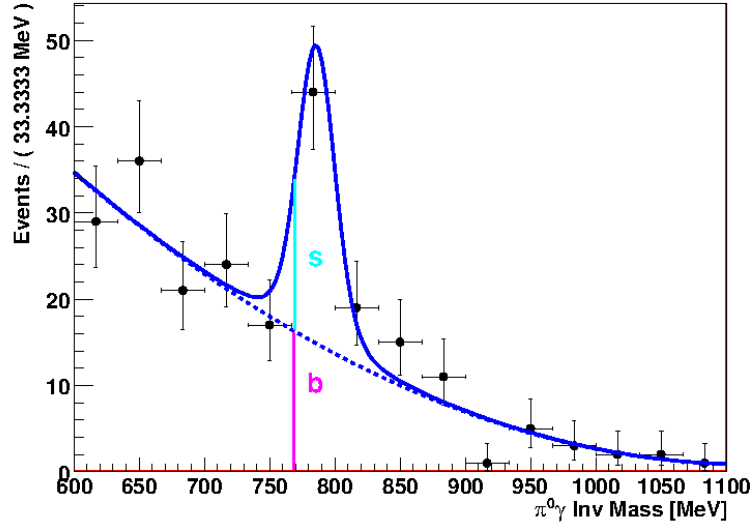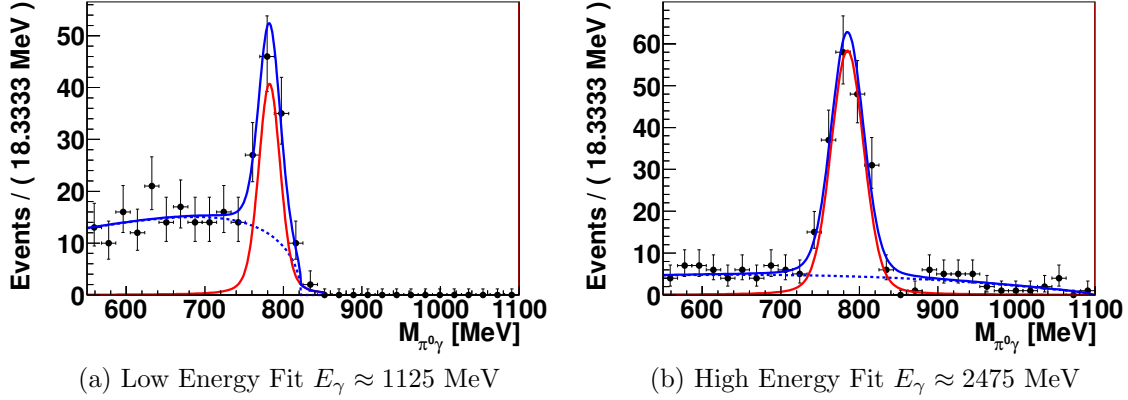
Figure 6.10: Q-factor Fit Examples for the $\gamma p \to p\omega$ Analysis. The data in the plot are from the seed event's nearest neighbor events. The ▬ is the fit of the total function (signal + background). The ▬ is the signal function. The ▬▬▬ is the background function.

from the $\gamma p \to p\omega$ reaction in the data set, the number of ω mesons was estimated in this peak by subtracting the background contributions. To define the nearest neighbors to each event, the kinematic variables for $\gamma p \to p\omega$ in Table 6.2 were used. In each fit, there were 300 nearest neighbors used to define the signal and background distributions. An important parameter to be chosen for Q-factor fitting is the number of nearest neighbors to be used in each fit. In this case, the ability of the fitting functions showed little dependence on the number of nearest neighbors. Therefore, 300 nearest neighbors were chosen to minimize the fit error while keeping the software run time to a reasonable amount of time.

The functions used to isolate the signal and background distributions are

- Background Function: Product of an Argus Function and a first order Chebychev function

- Signal Function: Voigt Function.

To get a good description of the background shape, an Argus function [33] is used to modify the Chebychev function to fit background at the edge of the phase space. The functional form of the Argus function is

$$f(x, m_0, c) = x \left(1 - \left(\frac{x}{m_0} \right)^2 \right)^{0.5} * \exp\left(c \left(1 - \left(\frac{x}{m_0} \right)^2 \right) \right) \quad , \qquad (6.15)$$

where m_0 is the parameter which defines the end of phase space and c is a curvature parameter and was fixed to $c = -1 \cdot 10^{-7}$. The m_0 parameter was initialized to the

largest $\pi^0\gamma$ invariant mass of the data to be fitted and was allowed to be changed ± 20 MeV from this value.

The Chebychev function was used to model the smooth shape of the background distribution away from the edge of phase space and is defined as

$$C(x) = C_0 + C_1 x \quad , \tag{6.16}$$

where x is the invariant mass. The zeroth order coefficient (C_0) was fixed to 1. The first order coefficient (C_1) was allowed to vary between -10 and 10 during the fit.

The Voigt function was initialized using known ω meson parameters from [1]. The peak position parameter for the Voigt function was initialized to 782 MeV and allowed to be changed during the fit ± 50 MeV. The σ parameter for the Gaussian width of the Voigt function is responsible for describing the measurement uncertainties and was initialized to 10 MeV and allowed to fit values between 7 - 50 MeV. The Breit-Wigner width parameter for the ω meson was fixed to 8.49 MeV [1] and was not allowed to be changed during the fit.

Fits for two energies are shown in Figure 6.10. Figure 6.10a shows how the allowable phase space at low initial photon energy was restricted. The $\pi^0\gamma$ invariant mass phase space stopped close to the value for the peak. To describe the end of phase space when it was close to the peak, the Argus function was essential. As the initial photon energy rose, the end of phase space moved away from the peak and resembled the fit in Figure 6.10b. Here the Argus is not needed and the Chebychev polynomial dominates.

The goodness of fit statistic (also known as the reduced χ^2) is a measure of how well each fit described the data. Figure 6.11 shows the spectrum of goodness of fit statistic values for every Q-factor fit in the analysis. The distribution shows a strong peak close to one in the data. This means the data distributions are on average well described by the fits.

The result of each Q-factor fit is a Q-factor. To form observables with the Q-factor, the contribution from each event was weighted with the Q-factor. A good example of this is to show the separation of background and signal in a $\pi^0\gamma$ invariant mass distribution. Figure 6.12 shows the $\pi^0\gamma$ invariant mass of all events selected by the cuts in Section 6.2 along with the background determined by using the Q-factor method of background subtraction. The background contribution was found by weighting each event with (Q-factor $- 1$) when filling the histogram. The shaded area shows a smooth description of the background and returns a believable separation of the two types of events. The continuity of the background description indicates the overall background separation worked well.
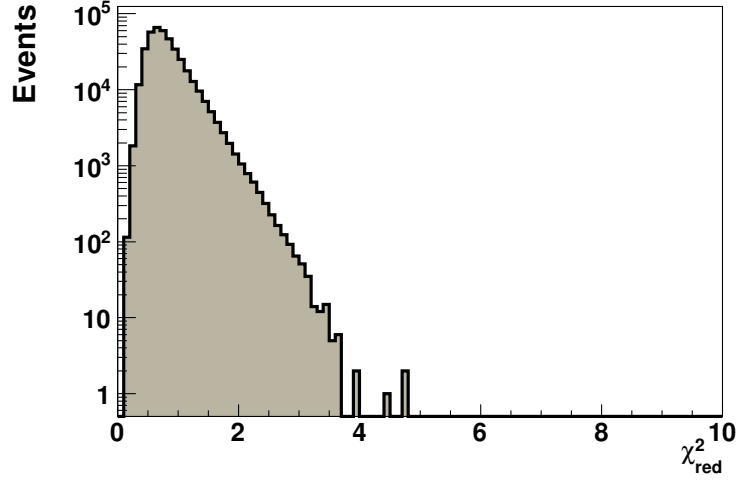
Figure 6.11: Q-factor Fitting Goodness of Fit Statistic for the $\gamma p \rightarrow p\omega$ Analysis. (experimental data events) $\chi^2_{reduced} = 1$ for a perfectly described distribution. Each value histogrammed represents one Q-factor fit.

Figure 6.12: Signal Background Separation ($\gamma p \rightarrow p\omega$). Invariant Mass of the $\pi^0\gamma$ System with Background Separation for $\gamma p \rightarrow p\omega$ selected experimentally measured events. The same events from Figure 6.7a are used in this plot. The shaded area is the background contribution determined by the Q-factor Method.

6.4.2 $\gamma p \to p\pi^0\omega$ Background Subtraction

The background subtraction for the $\gamma p \to p\pi^0\omega$ analysis was done for both the experimentally measured data (Figure 6.7c) and the Monte Carlo simulated data (Figure 6.7d). There were 150 nearest neighbors used in each Q-factor fit. The smaller number of nearest neighbors was used because of the more rapidly changing background shape. See Appendix B for more information on how the number of nearest neighbors was determined.

The functions used to isolate the signal and background distributions are

- Background Function: Second order Chebychev Function

- Signal Function: Voigt Function.

To account for the end of the $\pi^0\gamma$ invariant mass phase space, the fits are cutoff at the largest invariant mass value in each distribution.
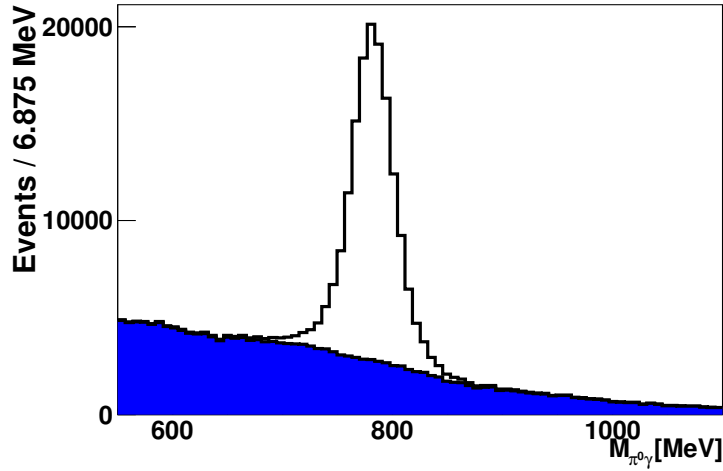
FITS TO EXPERIMENTALLY MEASURED DATA. The background function is a second order Chebychev function with the before-mentioned Voigt function for the line shape of the ω meson. Due to the slightly different background shape, the Argus function was not needed. The Chebychev function used for this analysis is

$$C(x) = 1 + C_1 x + C_2(2x - 1) \quad . \tag{6.17}$$

The Chebychev first order parameter (C_1) was initialized close to zero and allowed to be changed during the fit between -5 and 0.5. The Chebychev second order coefficient (C_2) is responsible for the deviation of the background function from linear and was allowed to take on a positive curvature ($0 - 10$) for the events below 1600 MeV in initial photon energy (E_γ). Above 1600 MeV, the curvature was fixed to zero and the first order coefficient was restricted to values between -0.2 and 0.1. The initialization and range parameters for the Voigt function are the same as for the $\gamma p \to p\omega$ analysis. The peak position parameters for the Voigt function were initialized using mean = 782 MeV and allowed to be fit ± 50 MeV. The σ parameter for the Voigt function is responsible for describing the measurement uncertainties and was initialized to 10 MeV and allowed to fit values between 7 - 50 MeV. The Breit-Wigner width parameter for the ω meson was fixed to 8.49 MeV [1] and was not allowed to be changed during the fit.

FITS TO MONTE CARLO SIMULATED DATA. The background distribution for simulated events consists of only combinatorial background. This combinatorial background comes from the two ways a $\pi^0\gamma$ combination can be obtained from an event with a $p\pi^0\pi^0\gamma$ final state. Therefore, the resultant distribution in Figure 6.7d has two contributions from each event. Since only one combination is the correct $\pi^0\gamma$ decay from the ω, the other combination contributes to a combinatorial background which must be subtracted. The invariant mass value of the combinatorial background is below the ω peak until the initial photon energy rises above 1550 MeV. Events with

an initial photon energy below 1550 MeV always have one combination with an invariant mass above 700 MeV (assigned a Q-factor of 1) and a combination with an invariant mass below 700 MeV (assigned a Q-factor of 0). Events with initial photon energy above 1550 MeV were subjected to a Q-factor fit.

The signal function is the same Voigt function. The background function is the Chebychev function defined as

$$C(x) = 1 + C_1 x \quad . \tag{6.18}$$

The first order coefficient (C_1) is restricted to values between -1 and 1. The signal function is the Voigt function with the same parameter limits as for the experimentally measured data.
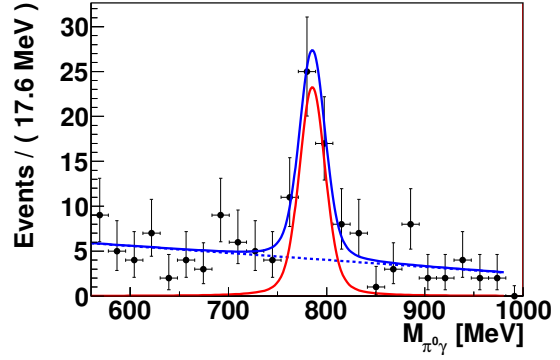
Figures 6.13 shows typical Q-factor fits used in the $\gamma p \to p\pi^0\omega$ analysis. The background shapes for the experimental data (Figures 6.13a and 6.13b) were linearly decreasing and made it easier to describe without the help of the Argus function. The fits were cut off at the edge of phase space (i.e. the largest value in each distribution). The simulated data fits (Figures 6.13c and 6.13d) show the small contributions of the combinatorial background which is described by the background function.

The overall quality of the fits to data are shown through the goodness-of-fit statistic which is plotted in Figure 6.14. Both distributions seem to peak close to one indicating that, on average, the data distribution was well described by the fits. The experimental data distribution (Figure 6.14a) seems to have a larger spread of values, but these deviations from one seem to be random. Overall, the fits describe the data well. The simulated fits shows a peak slightly smaller than one, but this is because the fits allowed more parameters to be fitted than the fitter needed to describe the data.

The background contribution (shaded area), calculated by weighting each event with (Q-factor $- 1$), is shown in Figure 6.15. The continuous description of the background seems to separate the signal and background events in a believable way. The simulated data distribution (Figure 6.15b) shows the relatively small contribution from the combinatorial background. Most of this type of background exists at invariant mass values below 600 MeV.
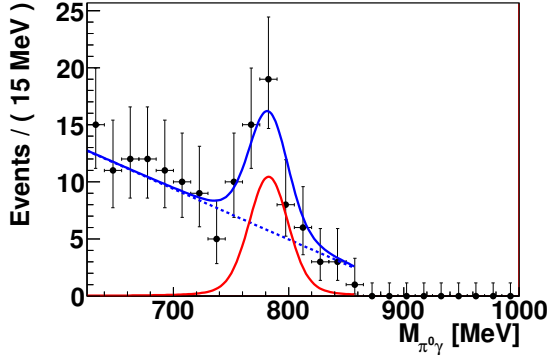
(a) Experiment Data Fit $E_\gamma \approx 1741$ MeV (b) Experiment Data Fit $E_\gamma \approx 2362$ MeV
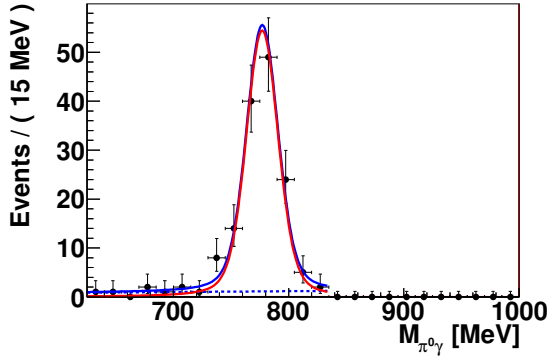
(c) Simulated Data Fit $E_\gamma \approx 1805$ MeV (d) Simulated Data Fit $E_\gamma \approx 2362$ MeV
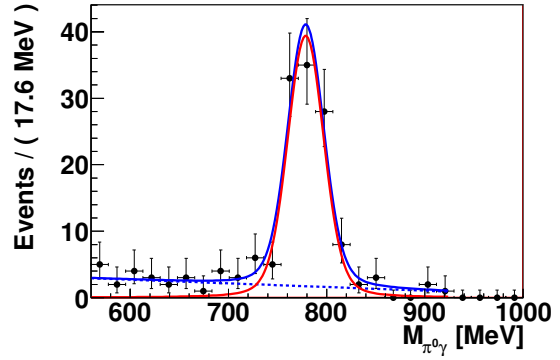
Figure 6.13: Q-factor Fit Examples for the $\gamma p \rightarrow p\pi^0\omega$ Analysis. The data in the plot are from the event's nearest neighbor events. The ▬ is the fit of the total function (signal + background). The ▬ is the signal function. The ▬▬ is the background function.

(a) Data Events   (b) Simulated Events
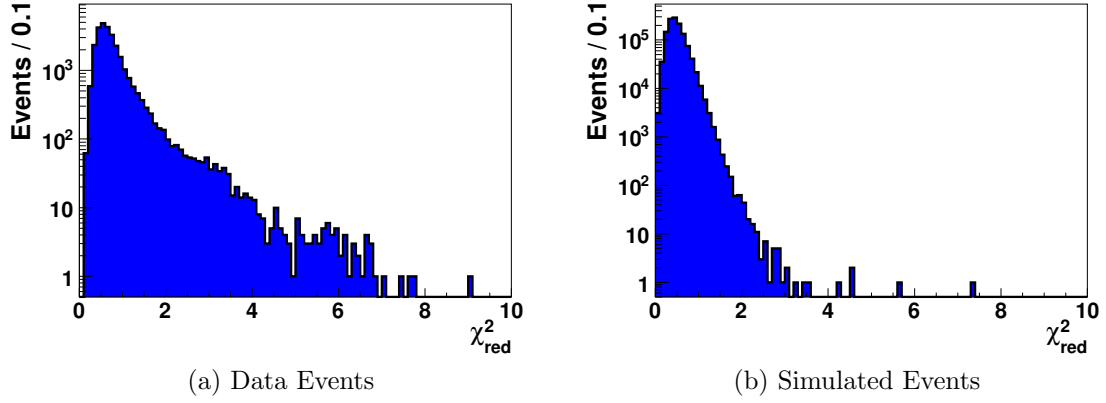
Figure 6.14: Q-factor Fitting Goodness of Fit Statistic for the $\gamma p \to p\pi^0\omega$ Analysis. (experimental data events) $\chi^2_{reduced} = 1$ for a perfectly described distribution.

(a) Experiment Data   (b) Simulated Data
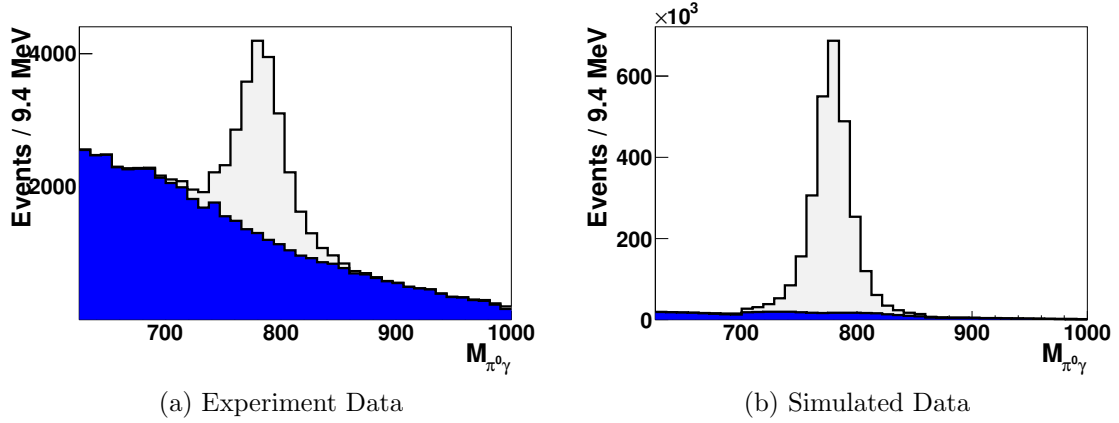
Figure 6.15: Signal Background Separation ($\gamma p \to p\pi^0\omega$). Invariant mass of the $\pi^0\gamma$ system with background separation for $\gamma p \to p\pi^0\omega$ selected events. The same events from Figure 6.7c and 6.7d are used in these plots. The shaded area is the background contribution determined by the Q-factor Method. The invariant mass of the $\pi^0\gamma$ combination is measured in MeV.

6.5 Background Composition

The background in Figures 6.12 and 6.15 are mainly events from a competing reaction which was mistaken for a signal event because the measured values of the event happened to match the values for a signal event. By either not detecting one of the photons or mistaking some other signal as a photon, reactions with a different number of final state photons can match the desired final state's number of detected particles.

6.5.1 $\gamma p \to p\omega$ Background

The final state which was selected for by the $\gamma p \to p\omega$ analysis is one charged particle (proton) and 3 uncharged particles (photons). To see the effect of competing reactions in the $\gamma p \to p\omega$ analysis, the experimental data were plotted using an invariant mass of all three photons versus the invariant mass of the two-photon combinations.

Figure 6.16a shows the distribution of experimentally measured events before Q-factor background subtraction. The vertical area of enhancement around 135 MeV is the contribution of the two-photon combination primarily decaying from π^0 mesons. A diagonal enhancement starting in the bottom left and continuing to the top right is the contributions of a $p\pi^0\eta$ event when one of the η meson photons is lost (from the two-photon decay). These enhancements indicate the dominance of $p\pi^0\pi^0$, $p\pi^0\eta$ and $p\pi^0$ events in the background. These contributions were not cut away using a data reduction cut because a cut in this distribution cut away too many signal events.

Figure 6.16b shows the same distribution after Q-factor background subtraction. This distribution shows a peak on the left side of the plot which corresponds to an ω meson with a π^0 in the final state, which is the signature of the desired final state. The extra horizontal enhancement to the right of the peak is the contribution of the other two-photon combination which did not come from the π^0 meson decay. This distribution shows a background free sample of $p\omega$ events.

6.5.2 $\gamma p \to p\pi^0\omega$ Background

The final state which was selected for by the $\gamma p \to p\pi^0\omega$ analysis is one charged particle (proton) and 5 uncharged particles (photons). The same $M_{\gamma\gamma}$ versus $M_{\gamma\gamma\gamma}$ distribution as the $\gamma p \to p\omega$ analysis was used to see the effect of the competing reactions which exist in the background contributions in the $\gamma p \to p\pi^0\omega$ analysis. In these distributions, there are 6 contributions from each event in the analysis. The considered final state configuration is $p\pi^0\pi^0\gamma$ and includes 2 $\pi^0\gamma$ combinations to obtain an ω meson (represented by $\gamma\gamma\gamma$) and 3 different ways to obtain a 2-photon combination from the 5 photons. Each π^0 meson decays to two photons.

Figure 6.17a shows the distribution of experimentally measured events before Q-factor background subtraction. Again we see the same sort of contributions from $p\pi^0\pi^0$, $p\pi^0\eta$ and $p\pi^0$ events in the background. The events with a true π^0 lie on a
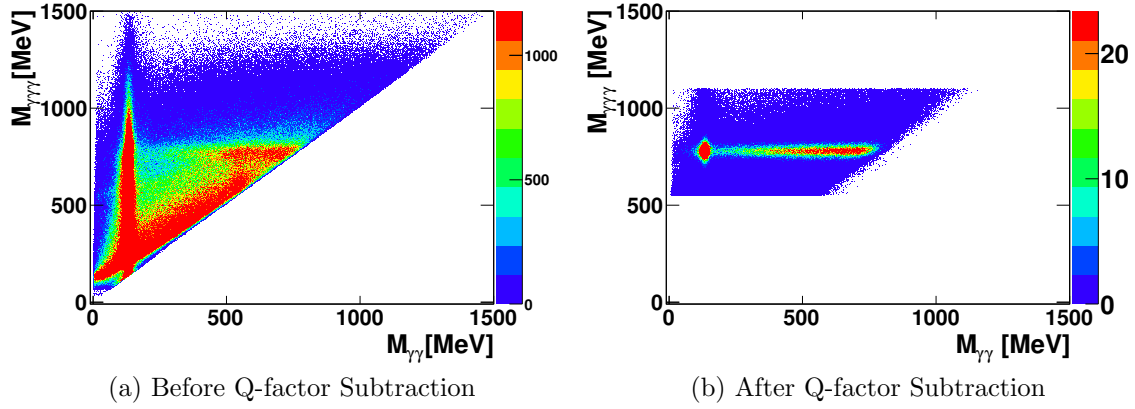
(a) Before Q-factor Subtraction   (b) After Q-factor Subtraction

Figure 6.16: Competing Reaction Contributions to the $\gamma p \to p\omega$ Background. The vertical axis is the invariant mass of all three detected photons. The horizontal axis is the invariant mass of each two-photon combination. There are three two-photon combinations for each event.

horizontal line at around 135 MeV in $M_{\gamma\gamma}$. Any $p\pi^0\eta$ with a missing η photon lies on the diagonal starting at low $M_{\gamma\gamma}$, low $M_{\gamma\gamma\gamma}$ and extending to high $M_{\gamma\gamma}$, high $M_{\gamma\gamma\gamma}$.

Figure 6.17b shows the distribution of events after Q-factor background subtraction. The peak at 780 MeV in $M_{\gamma\gamma\gamma}$ and 135 MeV in $M_{\gamma\gamma}$ are from the desired $\gamma p \to p\pi^0\omega$ events. There exists a reflection at higher $M_{\gamma\gamma}$ which is from the other contributions which did not correspond to the combination of photons to which the true ω meson decayed to. However, this contribution does exist close to the invariant mass of the η meson. Any possibility of which a final state with an η meson is involved is dealt with as a systematic uncertainty in the measurement and discussed in Section 8.4.

6.6   Reaction Selection Summary

Table 6.3 shows the statistics of the event reconstruction and selection for both analyses.

There are 4 types of data which are used in this analysis. They are :

- **Signal Events** - These events are experimentally measured data which pass all the data reduction cuts and are ultimately isolated using Q-factor background subtraction.

- **Timing Background Events** - These events are experimentally measured data which pass all the data reduction cuts, except for the Tagger Timing cut. These events are ultimately isolated using Q-factor background subtraction.

(a) Before Q-factor Subtraction   (b) After Q-factor Subtraction
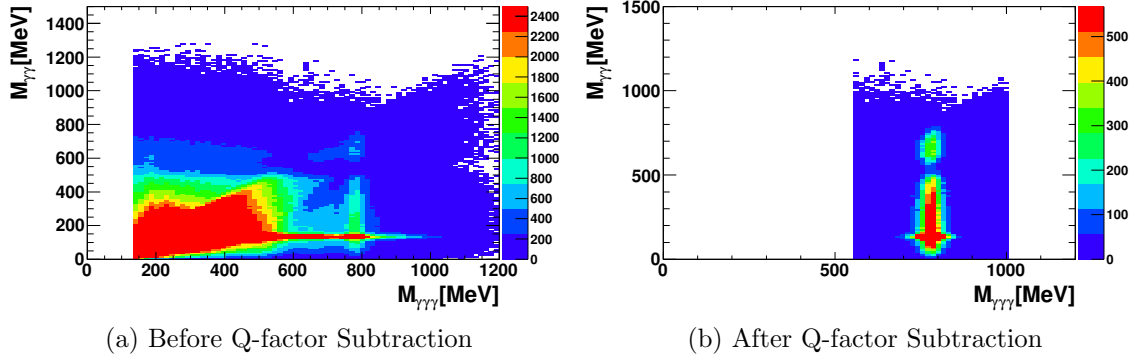
Figure 6.17: Competing Reaction Contributions to the $\gamma p \to p\pi^0\omega$ Background. The horizontal axis is the invariant mass of all three detected photons. The vertical axis is the invariant mass of each two-photon combination. There are three two-photon combinations for each event. These axes are opposite from the $\gamma p \to p\omega$ histograms in Figure 6.16.

Table 6.3: Total Analysis Statistics. The # of events isolated is a sum of the Q-factors for all events. Reconstructed simulated data are the generated data events subjected to all reconstruction and reaction selection criteria. The timing background are events which pass event selection criteria but have initial photon time outside of the timing window (Section 6.2.1).

Data Type	# of Q-factor fits	# of events isolated
$\gamma p \to p\omega$ analysis		
Experimentally Measured Data		
Signal	403,678	128,135
Timing Background	27,659	2,721
Simulated Data		
Reconstructed	0	4,036,360
Generated		27,251,000
$\gamma p \to p\pi^0\omega$ analysis		
Experimentally Measured Data		
Signal	64,455	15,805
Timing Background	4582	585
Simulated Data		
Reconstructed	2,749,729	2,682,220
Generated		20,376,593

The tagger timing requirements for these events are defined in Section 6.2.1

78

and are outside the tagger timing range for signal events.

- **Generated Simulated Events** - These events were simulated using the Monte Carlo GEANT3 software.

- **Reconstructed Simulated Events** - These events are the generated simulated events which were reconstructed in the modeled experimental setup. These events passed all the same data reduction cuts as the signal events. In the $\gamma p \rightarrow p \pi^0 \omega$ analysis, these events were also subjected to Q-factor background subtraction.

The number of experimentally isolated events, N_{data}, is defined as

$$N_{data} = N_{sig} - N_{TB} \quad , \tag{6.19}$$

where N_{sig} is the number of signal events and N_{TB} is the number of timing background events. The Q-factor background separation for the timing background events is shown in Figure 6.18.

(a) $\gamma p \rightarrow p \omega$ (b) $\gamma p \rightarrow p \pi^0 \omega$
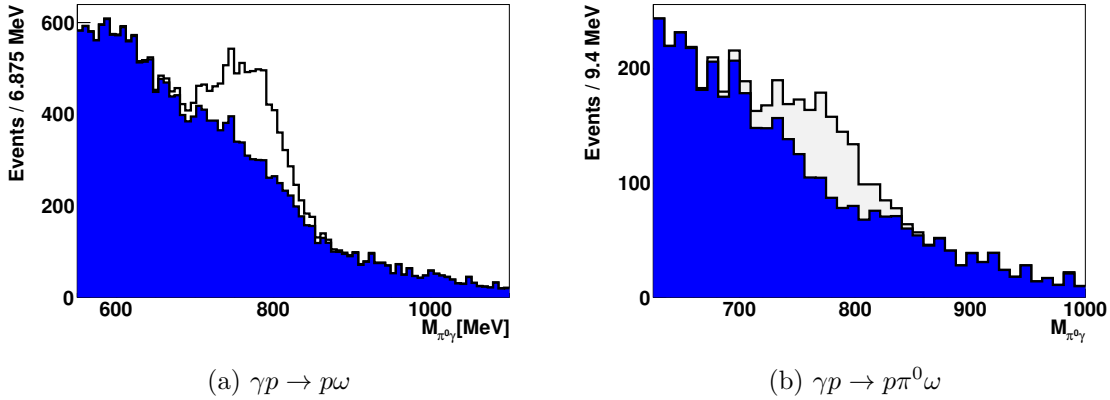
Figure 6.18: Timing Background Invariant Mass Distribution. Events were selected using the same selection criteria as events used in Figure 6.7, but had initial photon timing information outside the timing window. The background (shaded area) was determined using the Q-factor method. The invariant mass $M_{\pi^0\gamma}$ is measured in MeV in both plots.

6.7 Polarized Data Reaction Selection

The data runs used for the extraction of the polarized spin-density matrix elements were recorded in March 2003 and May 2003 with a linearly polarized photon beam incident upon a liquid hydrogen target. The run conditions for these data were

Table 6.4: List of Conditions for Triggering (Polarized Data).

Condition A	Two LED-low segments registering at least one hit above the LED-low threshold.
Condition B	One LED-high segment registering at least one hit above the LED-high threshold and at least **two** cluster in FACE.

very similar to the unpolarized data already discussed. However, one of the trigger conditions listed in Section 3.6.3 was different. The trigger conditions for these data are listed in Table 6.4. Trigger condition B was changed to emphasize reactions with more photons in the final state.

The reconstruction was almost exactly the same for the polarized $\gamma p \to p\omega$ analysis as the unpolarized data set. The change in trigger conditions allowed the omission of the trigger cut described in Section 6.2.5. The background subtraction was done by the Q-factor method described in Section 6.4.1 in exactly the same way. The resulting background separation is shown in Figure 6.19. A summary of the data sets used in the polarized SDME analysis is shown in Table 6.5.

The average degree of polarization for events in each energy bin is shown in Figure 6.20. The coherent edge listed in Table 6.5 defines at what initial photon energy the discontinuity in the degree of polarization exists in this plot.

(a) 1350 MeV Data   (b) 1600 MeV Data
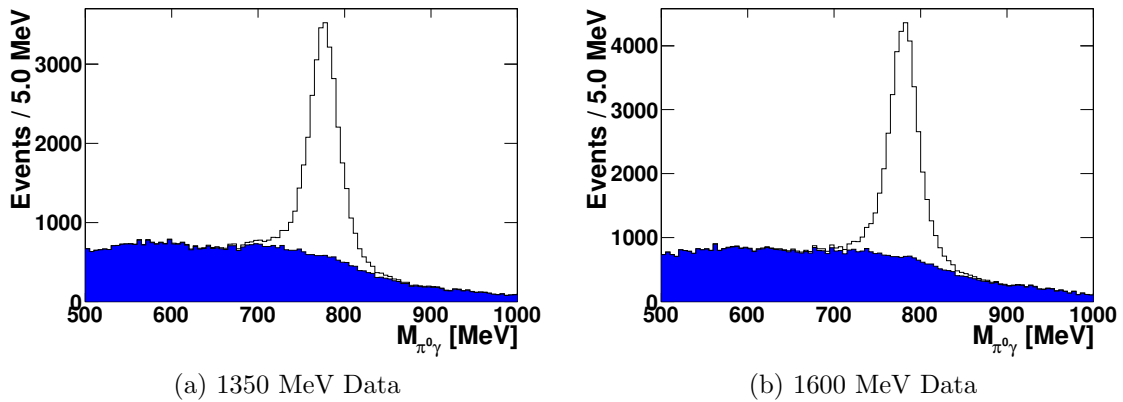
Figure 6.19: Polarized Data Background Separation. Experimentally measured signal events from polarized data runs. Each plot is labeled with its coherent edge energy.
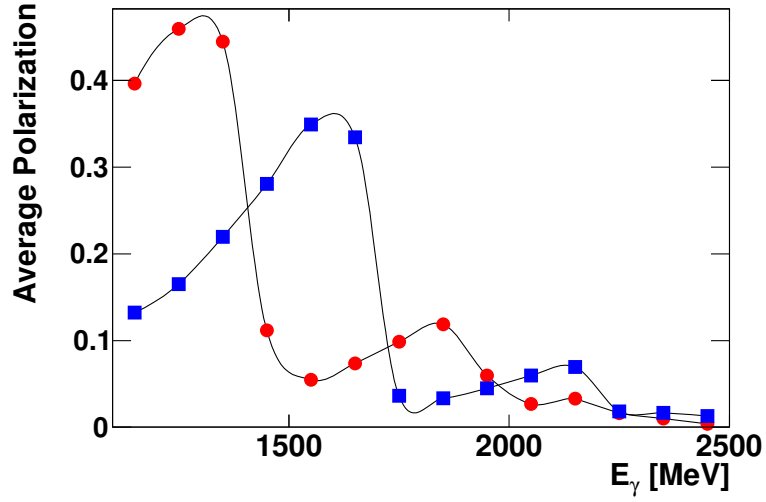
Figure 6.20: Polarized Data Degree of Polarization.   The fraction of photon with the desired linear polarization for the events in each dataset. The March 2003 (1350 MeV coherent edge) data is represented with a ●. The May 2003 (1600 MeV coherent edge) data is represented with a ■.

Table 6.5: Polarized Data Runs.   Data events observed is approximately the number of events isolated after Q-factor fitting.

Dates	Coherent Edge Energy	Data Events Observed
March 2003	1350 MeV	27,000
May 2003	1600 MeV	33,000

CHAPTER 7

MEASUREMENT FORMALISM

7.1 Differential Cross Section Measurement

To account for experimental issues, the differential cross section formula in Equation 1.3 must be modified. The differential cross sections for the $\gamma p \to p\omega$ and $\gamma p \to p\pi^0\omega$ reactions in this analysis are measured by

$$\frac{d\sigma}{dX_i} = \frac{N_{data}}{\mathcal{A} \, \mathcal{F} \, \rho_t^A \, BR \, \Delta X_i} \quad , \tag{7.1}$$

where X_i are kinematic variables (Section 7.1.1), N_{data} are the number of experimentally measured data events found in the kinematic range ΔX_i (Section 6.6), $\mathcal{A}$ is the acceptance correction (Section 7.1.4), $\mathcal{F}$ is the photon flux (Section 7.1.3), ρ_t^A is the target area density factor (Section 7.1.3), BR is the branching ratio for the final state's decay to the particles which were experimentally detected, and ΔX_i is the width of the kinematic bin the differential cross section is measured in.

The branching ratio used is calculated from the data shown in Table 6.1 from [1]. The branching ratio for the $\gamma p \to p\omega$ reaction is

$$BR^{\gamma p \to p\omega} = BR^{\pi^0 \to \gamma\gamma} \cdot BR^{\omega \to \pi^0\gamma} = 0.08815 \pm 0.004253 \tag{7.2}$$

and the branching ratio for the $\gamma p \to p\pi^0\omega$ reaction is

$$BR^{\gamma p \to p\pi^0\omega} = BR^{\pi^0 \to \gamma\gamma} \cdot BR^{\pi^0 \to \gamma\gamma} \cdot BR^{\omega \to \pi^0\gamma} = 0.08711 \pm 0.005132 \quad . \tag{7.3}$$

7.1.1 Kinematic Variables

The variables the differential cross section is measured in are discussed in this section. For many reasons, the differential cross section variables have been chosen to be comparable to previous measurements as much as possible.

7.1.2 $\gamma p \to p\omega$ Kinematic Variables

The variables a differential cross section (at constant energy) can be binned in for a two body final state ($p\omega$) are limited to one independent variable through energy

and momentum conservation and the invariance of the final state's azimuthal angle. The choices for the variable can be either a function of the polar angle of a final state particle or the mandelstam-t variable.

The variable chosen for this analysis is the cosine of the polar angle of ω meson in the center-of-mass frame, i.e. $\cos\theta^\omega_{c.m.}$. The width of each bin in this variable was dictated by the shape of the differential cross sections. The 18 bins in the range $(-1 \leq \cos\theta^\omega_{c.m.} \leq 0.8)$ have a bin width of 0.1, while the 6 bins in the range $\cos\theta^\omega_{c.m.} > 0.8$ have a width of 0.033.

An alternate variable which was chosen for this analysis is the polar angle of ω meson in the center-of-mass frame, i.e. $\theta^\omega_{c.m.}$. This variable was binned in 20 angular bins with a bin width of 0.05π radians. This alternate variable emphasizes the forward and backward angles much more than the $\cos\theta^\omega_{c.m.}$ variable.

The energy variable of these differential cross sections are defined as the energy of the initial state photon in the lab frame. The differential cross sections are binned in 50 MeV wide bins from 1100 MeV to 2500 MeV in initial state photon energy. 28 energy bins are reported in all.

$\gamma p \to p\pi^0\omega$ **Kinematic Variables.** The kinematic variables for a differential cross section in the case of a three body final state ($p\pi^0\omega$) are much more complicated than the two body final state considered in the $\gamma p \to p\omega$ analysis. The number of independent kinematic variables the data is binned in increases. The number of kinematic variables is related to the number of variables needed to describe a momentum in three-dimensional space. In this case, the number of total kinematic variables (at constant energy) is 9 (3 particles · 3 variables to describe the momentum). However, not all of these variables are independent. Using the momentum and energy conservation, there are 4 relations which can be defined to relate these kinematic variables. Therefore, there are 5 independent kinematic variables. However, the reaction can be defined such that the final state is invariant in the azimuthal angle, defined by the initial particles. This invariance reduces the total number of independent variables needed to fully describe this reaction to 4.

There are many possibilities for defining these four variables. However in this analysis, a quasi two body scheme is adopted and illustrated in Figure 7.1. To describe this scheme, we define three particles with labels a, b_1, and b_2. The k and a vectors define the reaction plane. The decay plane is defined by the momentum vectors of b_1 and b_2. An ideal kinematic variable to use to study the contribution of intermediate hadronic resonances is an invariant mass combining two of the particles ($M_{b_1b_2}$). The variable used to describe particle a is the cosine of the angle between the momentum of the a particle and the momentum of the incoming photon (k) (e.g. $\cos^a_{c.m.}$) and is measured in the center-of-mass frame. The last two variables describe the propagation directions of particles b_1 and b_2 in their rest frame. The first angle is defined as the cosine of the polar angle between the direction opposite the direction of travel of particle a and the direction of travel of particle b_1 (i.e. $\cos\theta^*$). The second angle (ϕ^*) is the angle between the two planes, reaction plane and decay plane. The four
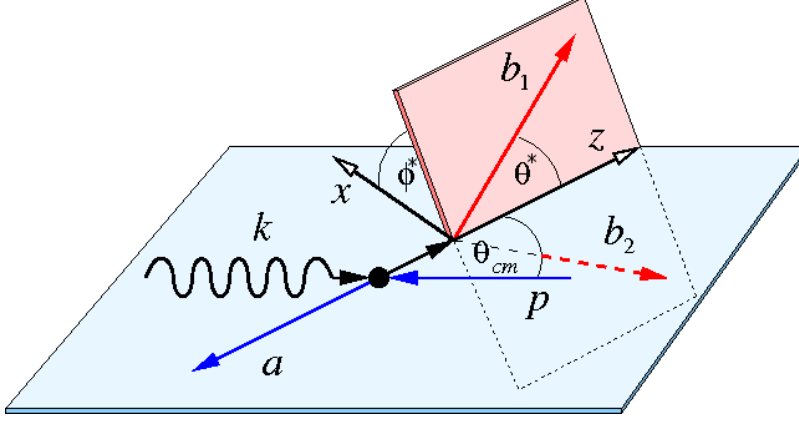
Figure 7.1: $\gamma p \to p\pi^0\omega$ Kinematic Variables. The particles are p, k, a, b_1, and b_2. Particles k and p are the initial state photon and proton, respectively, and are shown in the reaction's center-of-mass frame. Particle a is the final state particle dealt with in the center-of-mass frame of the whole reaction. Final state particles b_1 and b_2 are boosted into their own center-of-mass frame. The angular kinematic variables are $\theta_{c.m.}$, $\theta^\star$, and $\phi^\star$. The plane containing a,k, and p is referred to as the reaction plane. The decay plane and is defined by b_1 and b_2.

Table 7.1: $\gamma p \to p\pi^0\omega$ Kinematic Variable Set Definitions. a, b_1, and b_2 are defined in Figure 7.1.

Name	a	b_1	b_2	Variable List
$\omega_{c.m.}$	ω	π^0	p	$\cos\theta^\omega_{c.m.}, M_{p\pi^0}, \cos\theta^*_{\pi^0}, \phi^*_{\pi^0}$
$\pi^0_{c.m.}$	π^0	p	ω	$\cos\theta^{\pi^0}_{c.m.}, M_{p\omega}, \cos\theta^*_p, \phi^*_p$
$p_{c.m.}$	p	ω	π^0	$\cos\theta^p_{c.m.}, M_{\pi^0\omega}, \cos\theta^*_\omega, \phi^*_\omega$

kinematic variables used to define the observables for the $\gamma p \to p\pi^0\omega$ analysis are $\cos^a_{c.m.}$, $M_{b_1 b_2}$, $\cos\theta^*$, and ϕ^*.

Table 7.1 shows the definitions for each of the three kinematic variable sets used to measure the differential cross sections for $\gamma p \to p\pi^0\omega$. The particles are assigned to each particle label in a circular manner and will help with studying the uncertainties involved in binning in each kinematic variable set. Each set is named to provide a reference when reporting differential cross sections.

The binning in each kinematic variable is the same for all three kinematic variable sets in Table 7.1 and is shown in Table 7.2. The invariant mass variable $M_{b_1 b_2}$ has a variable width due to the available phase space at each energy. The bin limits are set according to the kinematically available range. The ϕ^* variable has only 1 bin due to the lack of statistics. The ΔX_i factor in Equation 7.1 is a product of the bin width factors in Table 7.2.

Table 7.2: $\gamma p \to p\pi^0\omega$ Variable Binning. The same number of bins are used for all three kinematic variable sets listed in Table 7.1. E_γ refers to the energy of the initial state photon.

Kinematic Variable	# of Bins	Bin Width
E_γ	25	50 MeV
$\cos\theta_{c.m.}$	10	0.2
$M_{b_1 b_2}$	10	variable
$\cos\theta^\star$	5	0.4
$\phi^\star$	1	360°

The energy binning of the differential cross sections for the $\gamma p \to p\pi^0\omega$ analysis is in 50 MeV wide bins from threshold up to 2.5 GeV in initial photon energy (Table 7.2).

7.1.3 Normalization

The normalization factors in the cross section are the factors accounting for the total number of initial state interactions having the chance to become the desired final state during the total data taking time of the experiment. The normalization is a product of the photon flux and the target area density.

Photon Flux. The photon flux factor $\mathcal{F}$ in Equation 7.1 is a count of the number of photons incident on the target during data taking. To find the correct number of photons, the formula

$$\mathcal{F} = N_{scaler}^{fiber} \cdot \alpha \cdot P_\gamma \tag{7.4}$$

is used, where N_{scaler}^{fiber} is the number of *free* hits in the tagger fibers, α is a factor accounting for the way photons are reconstructed from the *free* tagger fiber hits, and P_γ is the factor accounting for the fraction of photons actually traversing the target.

The N_{scaler}^{fiber} factor is the total number of hits recorded in the tagger fibers. This factor was measured by using a minimum bias trigger to accumulate fiber hits (scaler events) at a rate of 1 Hz during data taking. The minimum bias trigger recorded any hit in a fiber in the tagging hodoscope. The scaler events were then corrected for the lifetime of the experiment. This factor is independent of any hadronic triggering.

The α factor accounts for how the fiber hits are used to reconstruct photons in the tagger. This factor is a ratio of reconstructed photons to tagger fiber hits.

The P_γ factor is a measure of how many photons recorded at the tagger actually travel through the target. This factor is a ratio of photons passing through the target to total photons reconstructed in the tagger hodoscope. If the photons do not travel exactly down the beamline, the photons could miss the target. Special data taking runs called *Tagger-or* runs were used to compare hits in the tagger fibers with the hits in the γ veto detector (Figure 3.1). The γ veto detector was positioned
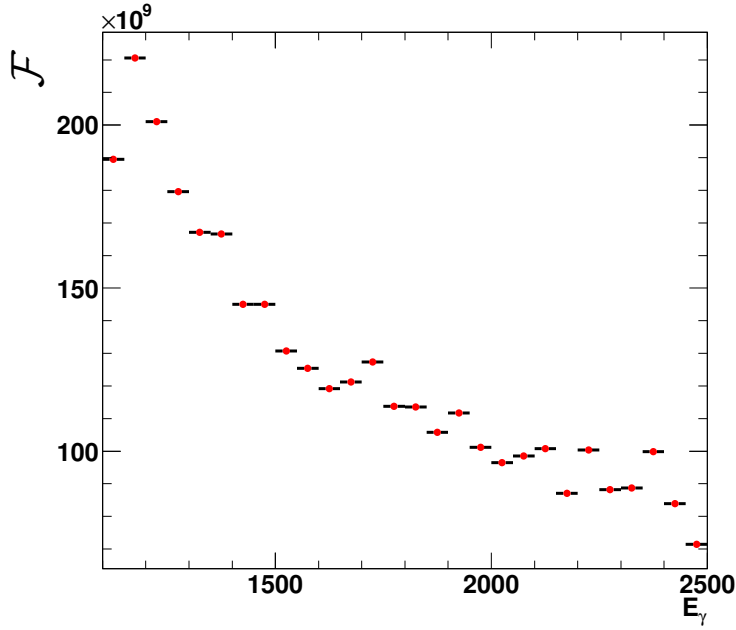
Figure 7.2: Photon Flux. The number of photons which were determined to traverse the target during the whole lifetime of the experiment. These factors were used for both $\gamma p \to p\omega$ and $\gamma p \to p\pi^0\omega$ analyses. The initial photon energy E_γ is measured in MeV.

downstream of the target. By using coincident hits in the γ veto detector and the tagger fibers, the fraction of photons traveling through the target was found to be $P_\gamma = 0.638 \pm 0.003_{stat} \pm 0.05_{sys}$, where *stat* indicates the statistical error and *sys* indicates the systematic error. The stability of this measurement was checked by analyzing Tagger-or runs at different incoming photon/electron rates.

Figure 7.2 shows the photon flux factors used in both analyses reported in this thesis. The inverse relationship between photon energy and the photon flux factors is due to the cross section for bremstrahlung radiation.

Target Area Density. The target area density ρ_t^A is the product of the density of protons in the liquid hydrogen target cell and the length of the target ($l_t = 5.275$ cm) and is calculated by

$$\rho_t^A = 2\,\frac{\rho(H_2)\,N_A\,l_t}{M_{mol}(H_2)} \quad , \tag{7.5}$$

where $\rho(H_2)$ is the mass density of liquid hydrogen ($\rho(H_2) = 0.0708$ g/cm³), N_A is Avogadro's number, $M_{mol}(H_2)$ is the molar mass of liquid hydrogen ($M_{mol}(H_2) = 2.015588$ g/mol), and the 2 is the number of protons in H_2. The final value used in

86

the analysis for both $\gamma p \to p\omega$ and $\gamma p \to p\pi^0\omega$ analyses is

$$\rho_t^A = (2.231 \pm 0.042) \cdot 10^{-7} \; \mu b^{-1} \quad . \tag{7.6}$$

7.1.4 Acceptance Correction

The detection of particle energies and/or momenta is a complex task which is never perfect. Even the most perfectly designed detector and analysis cannot detect every particle during an experiment. Just by having support structures to support the weight of the detector, the detection of a particle can be obscured. Therefore when making a measurement, the fraction of particles which were not detected must be estimated. Using this information, the number of desired signal events which were detected can be corrected to estimate how many events there actually were. This fraction is called the detector acceptance, $\mathcal{A}$.

$\gamma p \to p\omega$ and $\gamma p \to p\pi^0\omega$ events were simulated using the Monte Carlo simulation package described in Section 6.1. To find the fraction of events which would have been reconstructed, the simulated events were subjected to the same reconstruction and reaction selection as the experimentally measured events. These reconstructed events were compared to the originally generated events. The ratio of reconstructed Monte Carlo events N_{rec} to generated Monte Carlo events N_{gen} defines the detector acceptance, i.e.

$$\mathcal{A} = \frac{N_{rec}}{N_{gen}} \tag{7.7}$$

and is done in each kinematic bin.

$\gamma p \to p\omega$ **Acceptance Correction.** The acceptance correction factor for each kinematic bin is shown in Figure 7.3. The probability of detecting the ω meson when it goes in the most forward angles ($\cos \theta_\omega^{c.m.} \approx 1$) is around 30%. This rather large acceptance in this area is one of the reasons why this analysis for the reaction $\gamma p \to p\omega$ is an improvement over previous measurements (Section 2.1). The ability to have enough statistics in this region will be useful in isolating baryon resonance contributions from meson exchange diagram contributions.

$\gamma p \to p\pi^0\omega$ **Acceptance Correction.** The acceptance correction for the $\gamma p \to p\pi^0\omega$ analysis is much more complicated to show. There are three different acceptance corrections corresponding to the three different kinematic variable sets the differential cross section can be defined in. For each kinematic variable set, the factors are binned in 5 dimensions[1].

The distribution of acceptance correction factors are shown in Figure 7.4. Each value binned in these plots represents the acceptance for an individual kinematic bin. The average acceptance for this analysis is approximately 15%.

Appendix A shows and discusses the $\gamma p \to p\pi^0\omega$ acceptance correction in more detail.

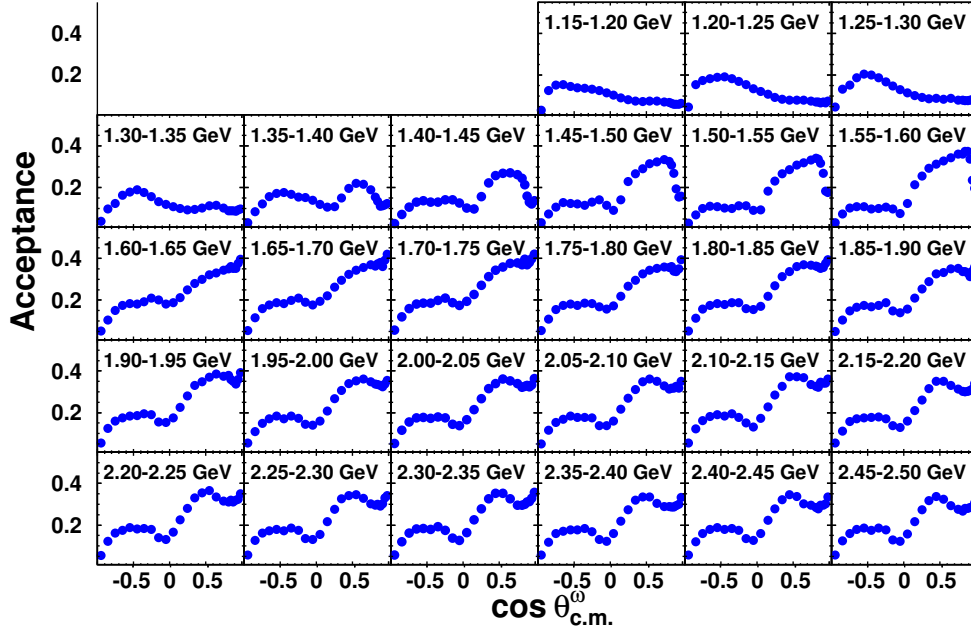[1] kinematic variables and initial photon energy

Figure 7.3: $\gamma p \rightarrow p\omega$ Acceptance. Each plot is labeled with its range in initial photon energy. The values were estimated by using Equation 7.7.

7.2 Spin-Density Matrix Elements

Additional observables which are available to be measured in the production of ω mesons are the elements of the spin-density matrix (SDME). These observables can be used in conjunction with the differential cross sections to obtain information about the spin dynamics of the reaction. The SDMEs are only measurable from a decaying particle which has non-zero spin, and cannot be measured for spin zero particles like the π^0 meson. SDMEs are a measure of how often each spin polarization of the ω is produced and can be used to help separate contributions which produce ω mesons with different spin polarization.

In this section, the spin-density matrix elements are reviewed. The method of extracting these observables from the decay distributions are presented.

Following the definitions in [10] and [34], the SDMEs (ρ_{ij}) are defined as [2]

$$\rho_{ij} = \frac{1}{N} \mathcal{M}_{i\,\lambda_\gamma} \rho_{\lambda_\gamma \lambda'_\gamma}(\gamma) \mathcal{M}^*_{j\,\lambda'_\gamma} \quad, \tag{7.8}$$

where i and j is the spin polarization of the ω meson used to define $\mathcal{M}$, and $\rho(\gamma)$ is the spin-density matrix for the initial photon. The normalization N is defined as

$$N = \frac{1}{2} \sum_{i,\lambda_\gamma} |M_{i\,\lambda_\gamma}|^2 \quad. \tag{7.9}$$

---

[2]All other indexes suppressed.

(a) $\omega_{c.m.}$ Binning

(b) $\pi^0_{c.m.}$ Binning
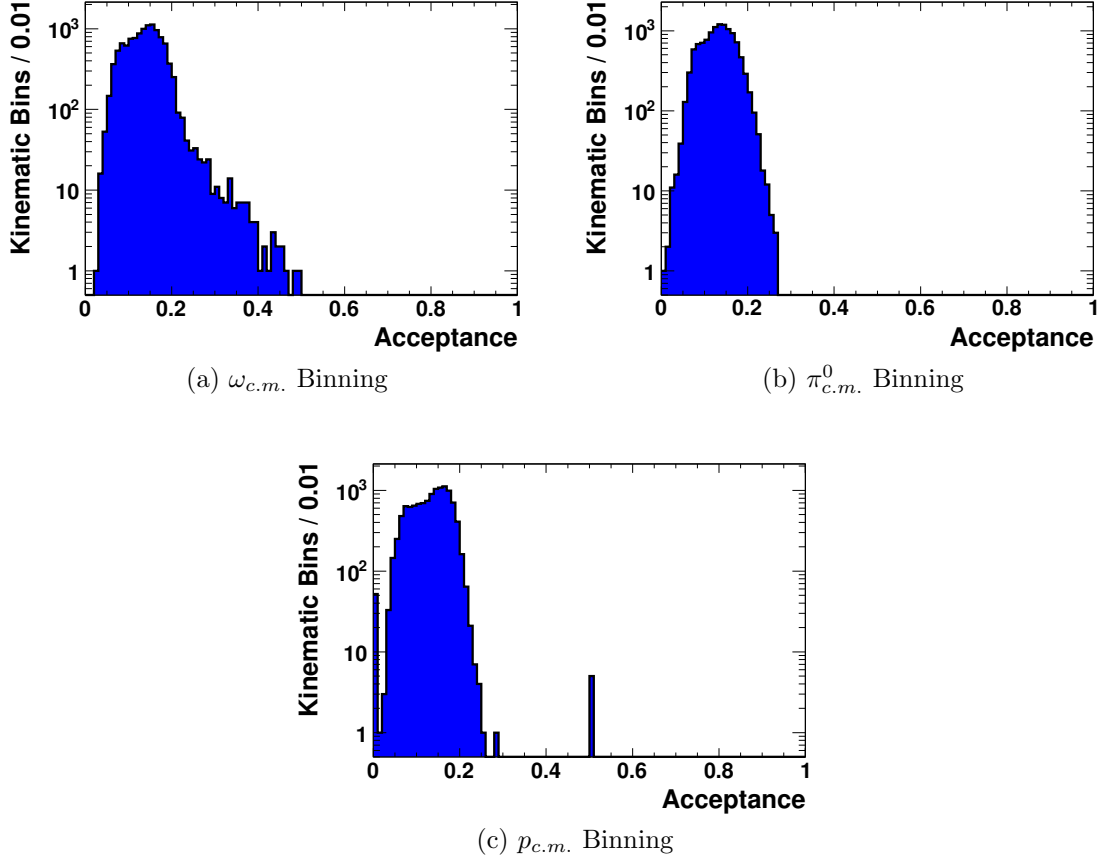

(c) $p_{c.m.}$ Binning

Figure 7.4: $\gamma p \rightarrow p\pi^0\omega$ Acceptance Correction Factor Distribution. The values were calculated by using Equation 7.7. The title for each plot refers to the kinematic variable set (Table 7.1) used to define the differential cross section. The values in these distributions are the individual acceptance factors for each kinematic bin.

The photon density matrix is defined as

$$\rho(\gamma) = \frac{1}{2}(I_\gamma + \sigma \cdot \vec{P}_\gamma) \quad , \tag{7.10}$$

where I_γ is the identity matrix, σ are the Pauli spin matrices, and $\vec{P}_\gamma$ is the polarization vector of the photon. For a linearly polarized photons, the polarization vector becomes $\vec{P}_\gamma = P_\gamma(-\cos 2\Phi_{pol}, -\sin 2\Phi_{pol}, 0)$, where Φ_{pol} is the angle between the photon polarization vector and the production plane[3] and is illustrated in Figure 7.5.

---

[3]defined by the final state proton and ω meson

89

Since the ω meson is a spin-1 particle, the possible spin polarizations are -1, 0 , 1. Therefore, the unpolarized spin-density matrix has the form

$$\rho^0 = \begin{pmatrix} \rho^0_{-1\,-1} & \rho^0_{0\,-1} & \rho^0_{1\,-1} \\ \rho^0_{-1\,0} & \rho^0_{0\,0} & \rho^0_{1\,0} \\ \rho^0_{-1\,1} & \rho^0_{0\,1} & \rho^0_{1\,1} \end{pmatrix} \quad . \tag{7.11}$$

However, the matrix ρ^0 must be hermitian, must respect parity conservation and must be normalized according to Equation 7.8. Therefore, the matrix reduces to [10]

$$\rho^0 = \begin{pmatrix} \frac{1}{2}(1 - \rho^0_{00}) & Re\rho^0_{10} + iIm\rho^0_{10} & Re\rho^0_{1\,-1} \\ & \rho^0_{0\,0} & -Re\rho^0_{10} + iIm\rho^0_{10} \\ & & \frac{1}{2}(1 - \rho^0_{00}) \end{pmatrix} \quad , \tag{7.12}$$

where the bottom left half of the matrix can be obtained by hermitian conjugation. Therefore, the spin-density matrix can be defined by measuring 4 numbers, ρ^0_{00}, $Re\rho^0_{10}$, $iIm\rho^0_{10}$, and $Re\rho^0_{1\,-1}$.

The angular distribution of the decay products involved in the $\omega \to \pi^0 \gamma$ decay with an unpolarized photon beam can be cast in the form [34]

$$\begin{aligned} W^0(\theta_d, \phi_d, \rho^0) &= \frac{3}{8\pi}(\sin^2\theta_d\rho^0_{00} + \left(1 + \cos^2\theta_d\right)\rho^0_{11} \\ &\quad + \sin^2\theta_d\cos 2\phi_d\rho^0_{1-1} + \sqrt{2}\sin 2\theta_d\cos\phi_d Re\rho^0_{10}) \quad , \end{aligned} \tag{7.13}$$

where θ_d and ϕ_d are the angles of the decay photon measured in the reference frame where the ω is at rest. The ρ^0_{11} matrix element is not an independent measurement and is equal to $\frac{1}{2}(1 - \rho^0_{00})$ and is related to the normalization used in Equation 7.8. This equation only contains three of the four numbers needed to define the whole spin-density matrix and means the matrix is not fully measurable with this method. However, the measured SDMEs will help in constraining the values in an interpretation analysis.

For measurements with a linearly polarized photon beam, the polarized spin-density matrices are reduced to [10]

$$\rho^1 = \begin{pmatrix} \rho^1_{11} & Re\rho^1_{10} + iIm\rho^1_{10} & Re\rho^1_{1-1} \\ & \rho^1_{00} & -Re\rho^1_{10} + iIm\rho^1_{10} \\ & & \rho^1_{11} \end{pmatrix} \tag{7.14}$$

and

$$\rho^2 = \begin{pmatrix} \rho^2_{11} & Re\rho^2_{10} + iIm\rho^2_{10} & Re\rho^2_{1-1} \\ & 0 & Re\rho^2_{10} - iIm\rho^2_{10} \\ & & \rho^2_{11} \end{pmatrix} \quad , \tag{7.15}$$

where the bottom left half of each matrix can be obtained by hermitian conjugation. The angular distribution of decay products can be cast into the form [10]

$$\begin{aligned} W^L(\cos\theta_d, \phi_d, \Phi_{pol}, \rho) &= W^0(\theta_d, \phi_d, \rho^0) - P_\gamma\cos 2\Phi_{pol}W^1(\theta_d, \phi_d, \rho^1) \\ &\quad - P_\gamma\sin 2\Phi_{pol}W^2(\theta_d, \phi_d, \rho^2) \quad , \end{aligned} \tag{7.16}$$
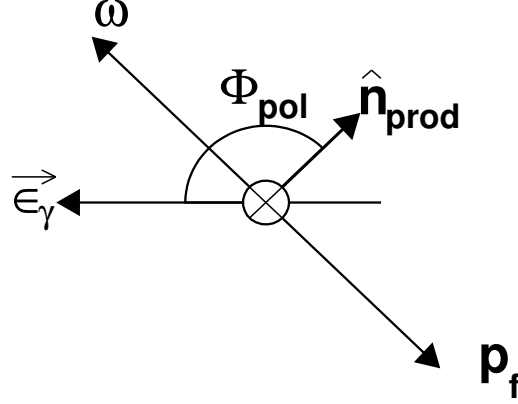
90

Figure 7.5: Production Polarization Angle. The beam of initial photons is into the page at the $\otimes$ symbol. The ω and p_f vectors indicate the direction of propagation of the final state particles. The $\vec{\epsilon_\gamma}$ vector is the direction of polarization of the initial state photon. The unit vector $\hat{n}_{prod}$ is the vector normal to the production plane, which is defined by the final state particles. The angle Φ_{pol} is the angle between the polarization vector, $\vec{\epsilon_\gamma}$, and the normal vector, $\hat{n}_{prod}$.

where Φ_{pol} is the angle between the photon polarization vector and the production plane, [34]

$$
\begin{aligned}
W^1(\theta_d, \phi_d, \rho^1) \;=\; & \frac{3}{8\pi}(\sin^2\theta_d\rho^1_{00} + \left(1 + \cos^2\theta_d\right)\rho^1_{11} \\
& + \sin^2\theta_d\cos 2\phi_d\rho^1_{1-1} + \sqrt{2}\sin 2\theta_d\cos\phi_d Re\rho^1_{10}) \quad, \quad (7.17)
\end{aligned}
$$

and

$$
W^2(\theta_d, \phi_d, \rho^2) \;=\; \frac{3}{8\pi}(\sin^2\theta_d\sin 2\phi_d Im\rho^2_{1-1} + \sqrt{2}\sin 2\theta_d\sin\phi_d Im\rho^2_{10}) \quad.(7.18)
$$

Notice many of the matrix elements in Equations 7.14 and 7.15 are not shown in Equation 7.16 and therefore not measurable with this method.

There are many coordinate systems in which θ_d and ϕ_d can be measured in. The direction of the z-axis is the defining parameter in each system. The popular systems to choose are [10]

- Helicity system - z-axis is chosen to be in the same direction as the ω meson in the overall center-of-mass frame,

- Adair system - z-axis is chosen to be in the same direction as the initial photon in the overall center-of-mass frame, and

91

- Gottfried-Jackson system - z-axis is chosen to be in the same direction as the initial photon in the rest frame of the ω meson.

In each system, the y-axis is defined to be $\hat{k} \times \hat{q}$, where $\hat{k}$ is a unit vector in the direction of the initial photon in the center-of-mass frame, $\hat{q}$ is a unit vector in the direction of travel of the ω meson in the center-of-mass frame and $\times$ is the vector cross product. The x-axis is defined by $\hat{y} \times \hat{z}$.

To extract the spin-density matrix elements, the data is filled into angular distributions which are a function of $\cos\theta_d$, ϕ_d. When extracting the linearly polarized SDMEs, the angular distribution is also a function of the angle Φ_{pol}. The angular distribution bin values are formed by

$$W = \frac{A}{\Delta X_i} \frac{N_{data}}{\mathcal{A}_{\omega \to \pi^0 \gamma}} \quad , \tag{7.19}$$

where N_{data} is the number of experimentally measured data events defined in Section 6.6, $\mathcal{A}_{\omega \to \pi^0 \gamma}$ is the detector acceptance (Section 7.1.4), A is the normalization to normalize the whole distribution to unity, and ΔX_i is the bin width of the $\cos\theta_d$ and ϕ_d variables. Finally, these distributions can be fitted using either Equation 7.13 for unpolarized data or Equation 7.16 for linearly polarized data.

CHAPTER 8

MEASUREMENT UNCERTAINTIES

The reporting of any experimentally measured value should always be accompanied by an estimated uncertainty. Two types of uncertainties accompany each reported value in this work: statistical[1] and systematic. The statistical uncertainty scales with the number of events used to measure each data point and is a measure of how precise the measurement is. All other errors are called systematic uncertainties. The systematic uncertainty is a measure of how accurate the measurement is.

Statistical uncertainties and systematic uncertainties are reported as separate values for each data point. The individual uncertainties from different sources are combined in quadrature to propagate them to the final values.

This section deals exclusively with the uncertainties in the differential cross sections. Since the cross section is an absolute measurement, the uncertainties in this type of measurement must be studied carefully. The uncertainties for the spin-density matrix elements use the same uncertainties.

8.1 Statistical Uncertainty

The statistical errors for these analyses come purely from the number of events used and any random errors associated with the target density (ρ_t^A) and branching fraction (BR) factors in Equation 7.1. The statistical error from events used in forming a value is obtained by

$$\sigma^2 = \sum_i w_i^2 \quad , \tag{8.1}$$

where σ is the uncertainty, i is the index of all the events used in forming the value, and w_i is the weight factor associated with the event i. This treatment stems from assuming a normal distribution. The weight factor w for any experimentally measured event or simulated $\gamma p \to p\pi^0 \omega$ event, which were subjected to Q-factor fitting, is equal the the Q-factor. For simulated $\gamma p \to p\omega$ events, no Q-factor fitting was done. Therefore for these events, $w = 1$.

---

[1]also called random error

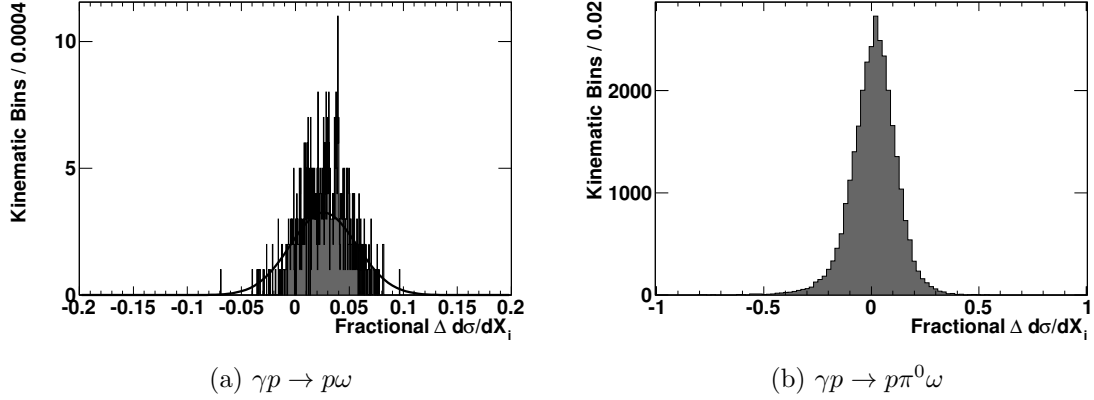(a) $\gamma p \to p\omega$ (b) $\gamma p \to p\pi^0\omega$

Figure 8.1: Target Shift Fractional Change. Each value binned in each plot represents one kinematic bin in the differential cross section measurement. The number of bins in the $\gamma p \to p\pi^0\omega$ analysis is much larger than in the $\gamma p \to p\omega$ analysis, because of the increased number of kinematic bins in the $\gamma p \to p\pi^0\omega$ analysis.

8.2 Simulation Systematic Uncertainty

Although the Monte Carlo simulation described in Section 6.1 models the CBELSA/TAPS experiment well, small errors can make a difference in the final reported measurements. This section describes the uncertainties in the simulation of the experiment.

The uncertainty from the Monte Carlo simulations themselves has been estimated to be 5.7% and is based on an analysis done in [35] and is in addition to other uncertainties mentioned in this section.

8.2.1 Target Shift Systematic Uncertainty

The placement of the target within the experimental setup is critical to the reconstruction of angles in the analysis. The uncertainty in the measurement of the position of the target was estimated to be ± 1.5 mm. To see what effect a simple misplacement of the target by this much would mean in the final differential cross sections, the target was moved upstream 1.5 mm in the Monte Carlo simulation and the differential cross section results remeasured.

Figure 8.1 shows the fractional difference between the target shifted differential cross sections and the corresponding final differential cross sections. For both analyses, the fractional change for each point is taken as the systematic uncertainty due to a possible target shift. The larger distribution of uncertainties for the $\gamma p \to p\pi^0\omega$ analysis is in part due statistical fluctuations.

94

8.2.2 Confidence Level Cut Systematic Uncertainty

The confidence level cuts, described in Section 6.2.3, use the results from kinematic fitting to cut away events from the analysis which are not signal events, but inevitably cuts away signal events as well. This cut is done for both the experimentally measured and simulated events at the same value. The main source of uncertainty in this parameter comes from the kinematic fit not distributing the signal events the same way for experimentally measured events and simulated events. The ratio of the signal events in each event type could change which would change the value of the final data point. Essentially, this uncertainty is an indicator of how well the kinematic fitter works and how well the simulation models the experiment.

To decide how much uncertainty is created by choosing the confidence level cut, the differential cross sections for each analysis were reformed by using several different choices of confidence level cut. Figures 8.2 and 8.3 show the fractional change in choosing the different confidence level cuts compared to the $CL < 0.005$ confidence level cut.

There are two sources of difference contributing to the value of each fractional change in Figures 8.2 and 8.3. The first source is the difference due to the confidence level cut. The second source is a statistical uncertainty due to the different number of events used to measure each compared data point. The value which is needed to estimate the confidence level uncertainty is only part of the whole difference. Therefore to separate the two types of uncertainties, the confidence level uncertainty is assumed to be a constant value over all kinematic bins and the statistical uncertainty follows a Gaussian distribution. So to extract the confidence level uncertainty, we define the mean value of the Gaussian distribution to be the confidence level uncertainty.

By comparing the values for each comparison, the overall value for the systematic uncertainty due to confidence level cut for the $\gamma p \to p\omega$ analysis is assumed to be less than 1.0%. The systematic uncertainty due to confidence level cut for the $\gamma p \to p\pi^0\omega$ analysis is assumed to be less than 3.0%. These uncertainties were applied to each kinematic bin.

8.3 Procedural Uncertainties

This section describes the uncertainties which come purely from procedures used in the analysis. These uncertainties estimate the effect each choice of parameter or analysis method has on the final data points.

8.3.1 Acceptance Correction Systematic Uncertainty ($\gamma p \to p\pi^0\omega$ only)

The acceptance correction is the factor which corrects the number of signal events for the fraction of events which were not observed. The binning of the acceptance correction (Section 7.1.4) can have an effect on the final differential cross section
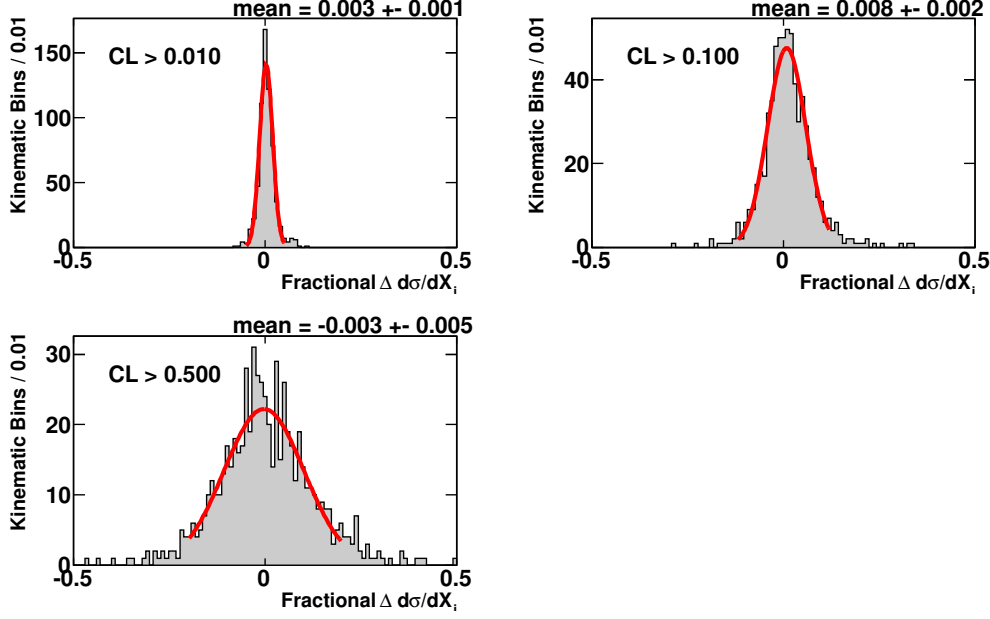
Figure 8.2: $\gamma p \rightarrow p\omega$ Confidence Level Fractional Changes. Each plot is labeled with the confidence level cut which was compared to the CL < 0.005 cut. The line is a Gaussian function with the fitted mean labeled on each plot. In this figure, CL means the confidence level of the $\gamma p \rightarrow p_{missing}\pi^0\gamma$ hypothesis.

measurement. Since this factor occurs in the denominator of Equation 7.1, the act of integrating over kinematic variables can have an effect on the final answer if the acceptance correction varies largely from constant.

The binning in the $\gamma p \rightarrow p\pi^0\omega$ analysis is restricted by the number of experimentally measured events isolated in each kinematic bin. If the kinematic bins are defined too small, the bin will not have enough experimentally measured events to report a value with a reasonable systematic error. However if the bin is defined too large, an acceptance correction with large deviations from constant in the bin can cause the measured value to deviate from the true value.

To explore the uncertainty created by defining one bin in the ϕ^* variable, the angle between the reaction plane and the decay plane, for all kinematic variable sets (Table 7.2), the differential cross section is measured again by increasing the binning in the ϕ^* variable from 1 to 4. This, in effect, splits each kinematic bin in the analysis into 4 separate bins. The differential cross sections were measured in each of these kinematic bins. To compare these altered cross sections to the original cross sections using only one bin in ϕ^*, each of the 4 new bins which represented the kinematic volume of the original kinematic bin were integrated over. This integration produced a new differential cross section data point which corresponds to the same binning as the original differential cross section point but is measured using a finer binning. The
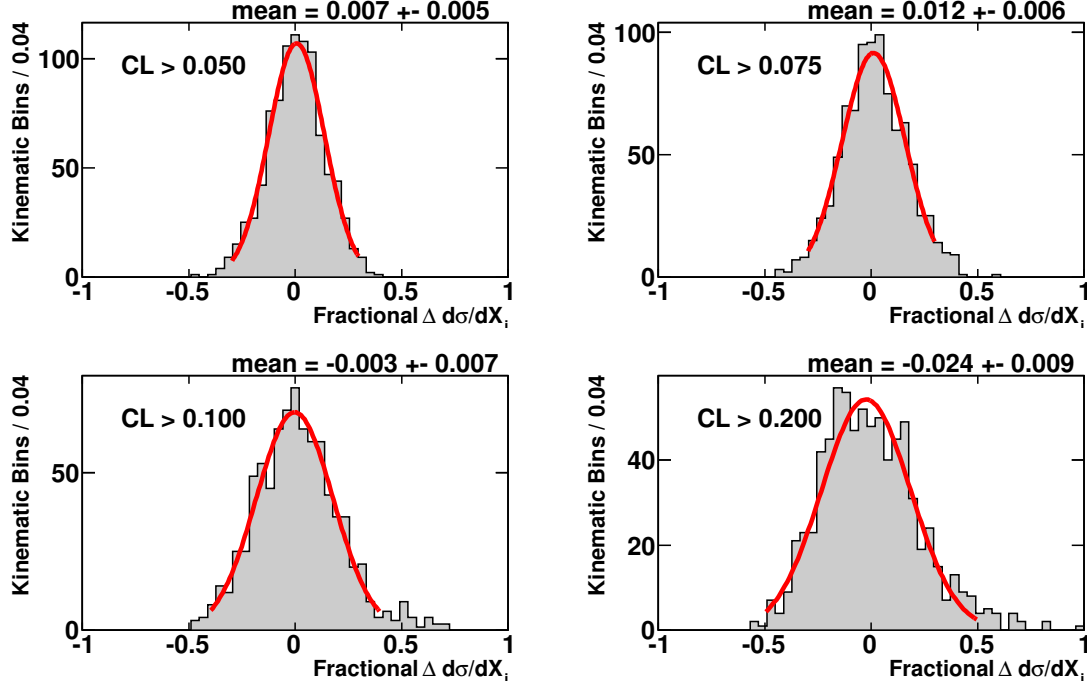
Figure 8.3: $\gamma p \to p\pi^0\omega$ Confidence Level Fractional Changes. Each plot is labeled with the confidence level cut that was compared to the CL < 0.005 cut. The line is a Gaussian function with the fitted mean labeled on each plot. In this figure, CL means the confidence level of the $\gamma p \to p_{missing}\pi^0\pi^0\gamma$ hypothesis.

fractional change is calculated as

$$\Delta_{Fractional} = \frac{\sigma_{altered} - \sigma_{final}}{\sigma_{final}} \quad , \tag{8.2}$$

where $\sigma_{altered}$ is the differential cross section with the altered parameters.

The difference between these two differential cross section points measured in the same kinematic variable values is, in part, due to the kinematic binning change. However since there is a different number of events used to measure each differential cross section in the results measured with finer binning, an additional statistical uncertainty is included in the difference. To separate these two uncertainties, we assume the fractional acceptance correction change is a constant across all kinematic bins and fit the distribution of values with a Gaussian function, which models the statistical uncertainty. The mean of the Gaussian function is the average change due to the acceptance correction binning.

The distribution of the fractional changes in the differential cross section for each kinematic bin is shown in Figure 8.4. The kinematic variable sets are treated and plotted separately. To separate the statistical uncertainty from the acceptance correction uncertainty, the distributions were fitted to a Gaussian function from -0.2

(a) $\omega_{c.m.}$ Binning

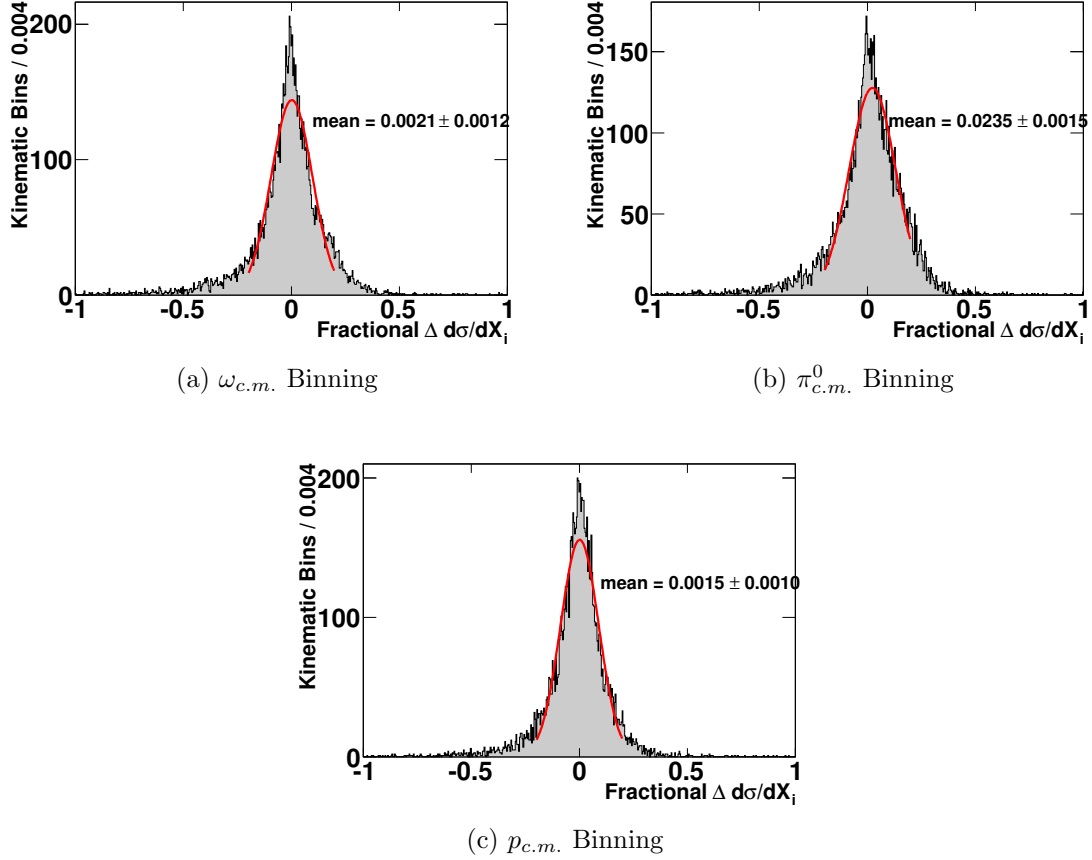(b) $\pi^0_{c.m.}$ Binning

(c) $p_{c.m.}$ Binning

Figure 8.4: $\gamma p \rightarrow p\pi^0\omega$ Acceptance Correction Fractional Change. Each plot is labeled with the name of a kinematic variable set defined in Table 7.1. The fitted mean of the Gaussian function fitted to the distribution from -0.2 to 0.2 is labeled on each plot. Each binned value represents one kinematic bin in the final differential cross sections.

to 0.2. The mean difference for each kinematic variable set is labeled on each plot in Figure 8.4. The quoted mean was used as a systematic uncertainty due to acceptance correction binning for all kinematic bins defined in that kinematic variable set. The acceptance correction uncertainty for the $\omega_{c.m.}$ and $p_{c.m.}$ kinematic binnings are smaller than 0.5% and insignificant. However, the $\pi^0_{c.m.}$ kinematic binning shows a much larger acceptance correction uncertainty of approximately 2% and is likely due to a acceptance which differs largely from constant in the ϕ^* kinematic variable.

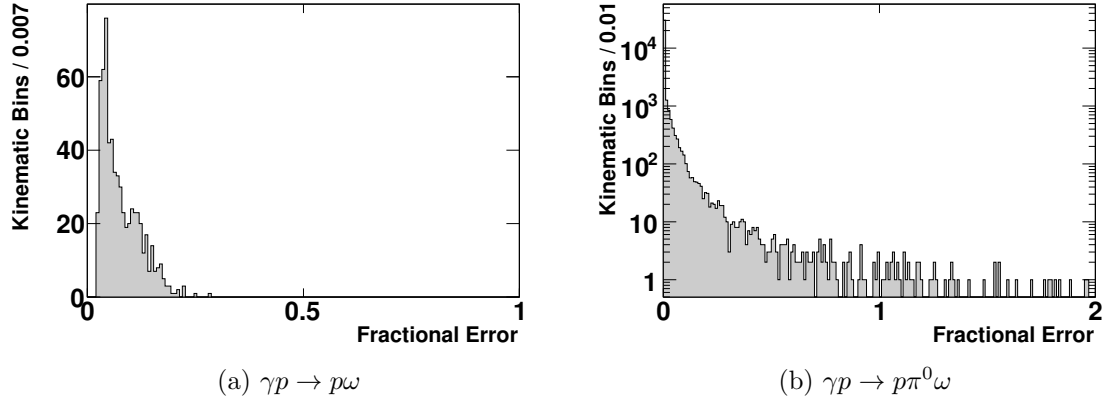(a) $\gamma p \to p\omega$ (b) $\gamma p \to p\pi^0\omega$

Figure 8.5: Q-factor Systematic Uncertainty. Each value is the fractional uncertainty of a reported differential cross section point. The $\gamma p \to p\pi^0\omega$ plot has been filled with ratios from all three kinematic binnings. Each value histogrammed represents one kinematic bin in the differential cross section.

8.3.2   Q-factor Fitting Systematic Uncertainty

Each fit used in the Q-factor method of background subtraction (Section 6.4) estimates an uncertainty for each parameter in the fit. When these uncertainties are propagated to the Q-factor, the resulting uncertainty will provide an estimate of how well determined the Q-factor itself is. Since the error of each parameter is linked to how well the fitting function describes the data, the uncertainty of the parameters is also an estimate of how well the fit does at modeling the invariant mass distribution. The method of propagating the error of the parameters to the uncertainty of each point in the differential cross section is taken from [31].

To propagate the error of the fit parameters to the Q-factor error ($\sqrt{\sigma_Q^2}$), the formula

$$\sigma_Q^2 = \sum_{ij} \frac{\delta Q}{\delta \alpha_i} \left(C_\alpha\right)_{ij} \frac{\delta Q}{\delta \alpha_j} \tag{8.3}$$

is used, where α_i is a fit parameter with index i and C_α is the covariance matrix which contains the errors of each fit parameter. The covariance matrix is calculated by and obtained from the RooFit fit package [32] used for fitting.

The propagation of these Q-factor errors to an uncertainty in the differential cross section point is calculated by

$$\sigma_y = \sum_{lk} \sqrt{\sigma_{Q_l}^2}\, \rho_{lk} \sqrt{\sigma_{Q_k}^2} \quad , \tag{8.4}$$

99

where $\sqrt{\sigma_{Q_l}^2}$ is the Q-factor error for an event with index l and ρ_{lk} is the correlation factor between events with index l and k. The correlation factor is calculated by

$$\rho_{lk} = \frac{N_{common}}{N_{nn}} \quad , \tag{8.5}$$

where N_{nn} is the number of nearest neighbors used in Q-factor fitting and N_{common} is the number of those nearest neighbors which were used in both events l and k. The relative systematic uncertainty due to Q-factor fitting is shown in the two plots in Figure 8.5.

The Q-factor fitting uncertainties for the $\gamma p \rightarrow p\omega$ analysis are generally below 25% and are relatively small. However, the uncertainties for the $\gamma p \rightarrow p\pi^0\omega$ analysis have a much larger range of values. This is due to the small statistics in some kinematic bins in this analysis which affects both the ratio in the fraction but also the quality of the fit. If the fit covers too much phase space in the kinematic variables, the fit quality becomes poor. These larger values indicate there are a few kinematic bins in this analysis which are not sensitive to the physics of this reaction. These bins, however, do serve a purpose in that the error sets an upper bound to the value of the differential cross section at that point in phase space. Therefore, these data points are reported as is. A large portion of the kinematic bins do have very good sensitivity and in addition to the bins with large errors are still useful for an interpretation analysis.

8.3.3 Photon Flux Systematic Uncertainty

The photon flux is the factor which normalizes the differential cross section to the number of photons which had the chance to become the sought after reaction. The uncertainty in the number of photons passing through the target during the whole data taking period is assumed to be dominated by P_γ (Section 7.1.3). P_γ is the factor which corrects for the photons which were detected in the tagger scintillator fibers but missed the target. The systematic error for P_γ was reported by the analysis in [25] to be 7.8% for this dataset, but to ensure all the uncertainty is included, the systematic error for the photon flux is assumed to be 10% [25].

8.4 Background Contributions

The last uncertainty is to estimate how much of the competing reactions is still in the signal. Even after all the cuts and background subtraction, these event could still be contributing.

The background reactions $\gamma p \rightarrow p\pi^0$, $\gamma p \rightarrow p\eta$, $\gamma p \rightarrow p\pi^0\pi^0$, and $\gamma p \rightarrow \pi^0\eta$ were simulated using the Monte Carlo software described in Section 6.1. These events were subjected to the same reconstruction and reaction selection procedures as the experimentally measured data events, including Q-factor background subtraction. The resulting reconstructed events (N_{rec}) were compared to the generated events

(N_{gen}) to obtain a probability for each background reaction to contribute to the final differential cross section as a function of the analysis's final state kinematic variables (P_{BKG}), i.e.

$$P_{BKG} = \frac{N_{rec}}{N_{gen}} \quad . \tag{8.6}$$

To define how many events were generated in each bin, the total number of events generated in each initial photon energy bin where equally distributed over the kinematic bins in that energy bin.

The number of background reaction events in a kinematic bin (N_{BKG}) can be deduced by

$$N_{BKG} = \frac{\sigma_{Tot}}{N_{bins}} \, P_{BKG} \, \mathcal{F} \, \mathcal{T} \, BR \quad , \tag{8.7}$$

where $\mathcal{F}$ is the photon flux, $\mathcal{T}$ is the target area density, BR is the branching ratio describing the decay to the considered final state, and $\frac{\sigma_{Tot}}{N_{bins}}$ is the total cross section averaged over the kinematic bins. The total cross sections were obtained from [25, 36, 37, 38] respectively.

Due to the averaging, this factor cannot be applied to the final cross section directly, therefore we define an additional systematic uncertainty. A fractional uncertainty for each point in the differential cross section due to each background reaction is defined as

$$\sqrt{\sigma_{BKG}^2} = \frac{N_{BKG}}{N_{data}} \quad , \tag{8.8}$$

where N_{data} is the number of experimentally measured events used to form the reported differential cross section.

Reactions with final states which decay to a number of photons that differ from this analysis by one are considered. The likelihood for either mistakenly reconstructing an unphysical photon or failing to reconstruct a real photon are the greatest.

The statistics and reaction topology used in each background reaction simulation is listed in Table 8.1. The estimated fractional uncertainties for background reaction contributions are shown in Figure 8.6 for the $\gamma p \rightarrow p\omega$ analysis.

The fractional uncertainty for the single meson background reactions are very small. However, the values for the two double meson reactions are on the order of 2-4%. Since these values are only estimates, the values are not used to modify the differential cross section values. These uncertainties were propagated point by point to the systematic uncertainty for the $\gamma p \rightarrow p\omega$ analysis.

In Table 8.1, the number of reconstructed events for the background reactions are smaller than the number of kinematic bins (12,500) in the $\gamma p \rightarrow p\pi^0\omega$ analysis. Therefore, estimating a background uncertainty for each kinematic bin is not possible. Due to the very small reconstruction efficiency of these reactions, the uncertainty analysis is estimated in each energy bin only. The background fraction in Figure 8.7 was estimated using Equations 8.7 and 8.8. Since this was done for each energy bin ignoring kinematic bins, all values are a sum over the kinematic bins and $N_{bins} = 1$.

Table 8.1: Background Reaction Uncertainty Analysis Statistics. Events generated is the number of events generated by the Monte Carlo simulation package. Events reconstructed is the number of generated events which were isolated as signal events after data reduction and Q-factor background subtraction.

Background Reaction	Decay Photons	Generated	Reconstructed
$\gamma p \to p\omega$ analysis (Detected Final State: 3 photons)			
$\gamma p \to p\pi^0$	2	3,800,000	3
$\gamma p \to p\eta$	2	4,000,000	148
$\gamma p \to p\pi^0\pi^0$	4	5,333,333	7592
$\gamma p \to p\pi^0\eta$	4	2,666,666	6884
$\gamma p \to p\pi^0\omega$ analysis (Detected Final State: 5 photons)			
$\gamma p \to p\eta$	6	4,000,000	26
$\gamma p \to p\pi^0\pi^0$	4	5,333,333	648
$\gamma p \to p\pi^0\eta$	4	2,666,666	34

These values are the fraction of detected experimentally measured events which could have been from each background reaction.

The values are smaller than 1% and do not indicate a large contamination from these reactions. The systematic uncertainty for each energy bin was applied to all kinematic bins with the same energy binning.

8.5   Summary

Figure 8.8 shows a summary of all uncertainties. The two types of uncertainties are presented separately and are also reported separately when presenting the data. Each data point histogrammed represents one kinematic bin in each analysis and has been calculated by adding all the errors in this section in quadrature.

The statistical uncertainties are essentially a measure of how much statistics goes into measuring each data point and also how precise the differential cross section values are. The statistical uncertainties for the $\gamma p \to p\omega$ analysis in Figure 8.8a show values below 25%. Due to the kinematic coverage and binning, this uncertainty is small enough to allow an interpretation analysis to isolate baryon resonances. The statistical uncertainties for the $\gamma p \to p\pi^0\omega$ analysis are much larger in comparison however. These larger errors are due to the relatively small number of experimentally measured $\gamma p \to p\pi^0\omega$ events in each kinematic bin. The kinematic binning was chosen this way to stretch the statistics as far as possible to allow a proper detector acceptance analysis. As will be seen in the results section, these uncertainties can be greatly reduced by integrating over kinematic bins. The statistical uncertainties are small enough and the kinematic coverage good enough to allow an interpretation analysis which can be performed on data points over almost the whole kinematic phase
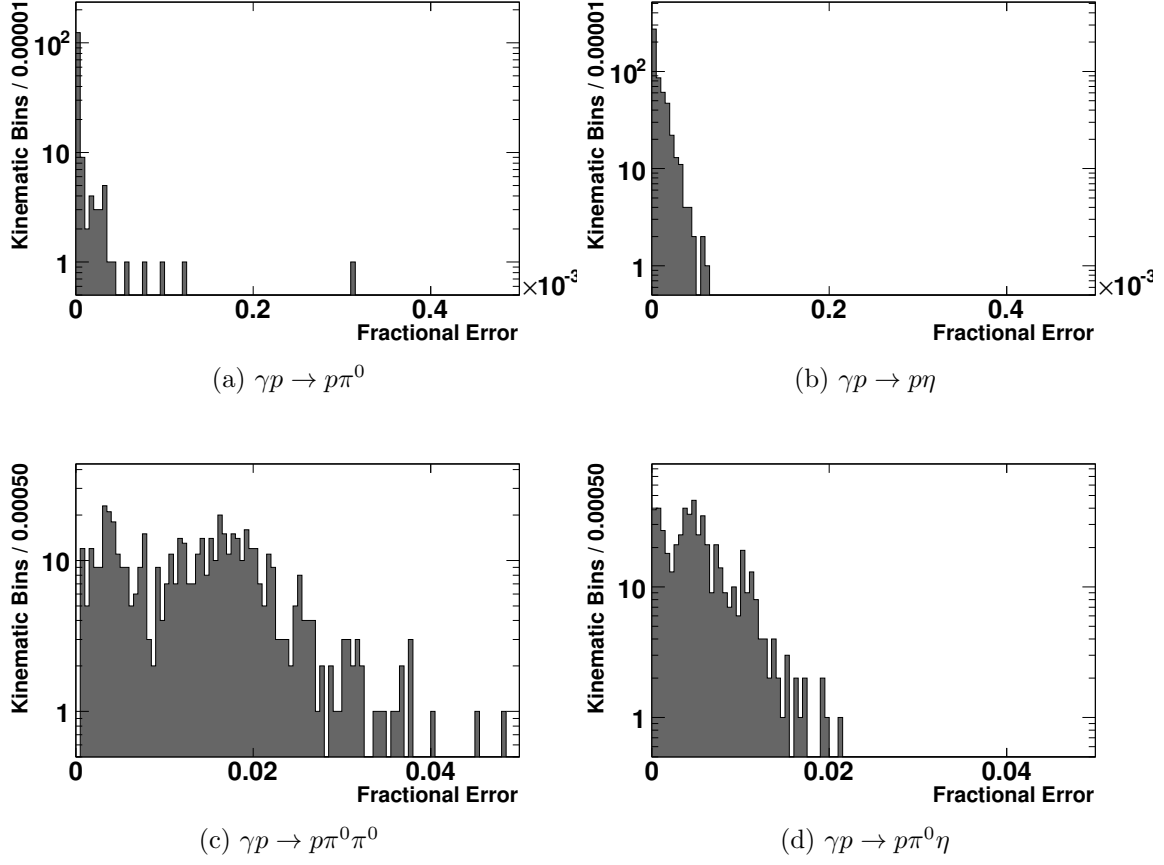
(a) $\gamma p \to p\pi^0$

(b) $\gamma p \to p\eta$

(c) $\gamma p \to p\pi^0\pi^0$

(d) $\gamma p \to p\pi^0\eta$

Figure 8.6: $\gamma p \to p\omega$ Background Reaction Uncertainty. Each plot is the fraction of the experimentally measured events which could have been from each background reaction in each kinematic bin.

space. The extra peaks between 0.5 and 1.0 in Figure 8.8c come from kinematic bins with very low statistics which cause rounding errors in the uncertainty calculation to occur.
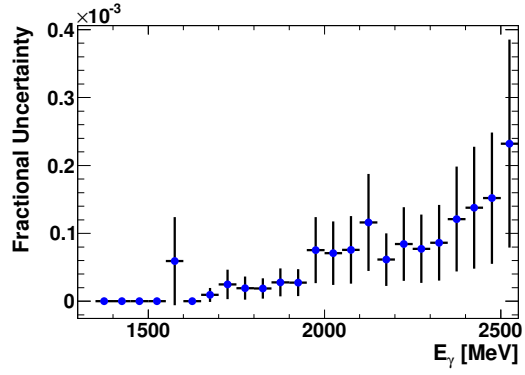
The systematic uncertainties are a measure of how accurate the differential cross section values are. By estimating the effect of possible errors, the values for the systematic uncertainty were estimated. The total systematic uncertainty for both analyses seem to average around 15% and are relatively small.
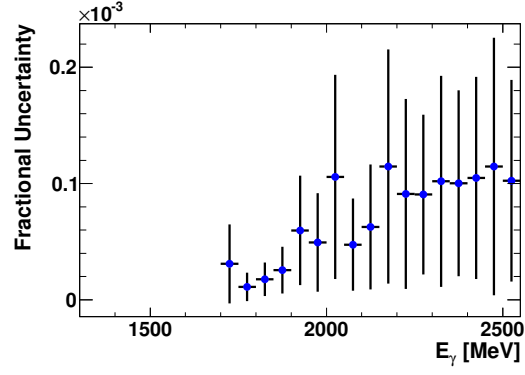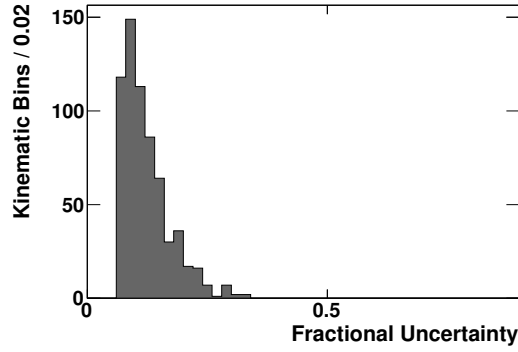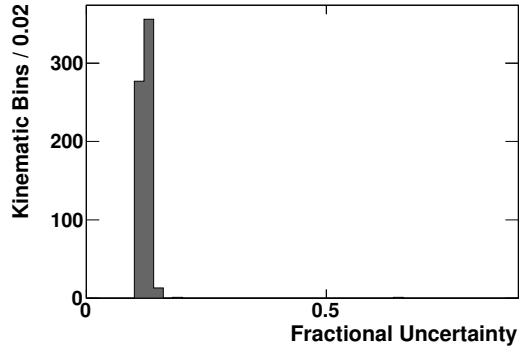
(a) $\gamma p \to p\eta$
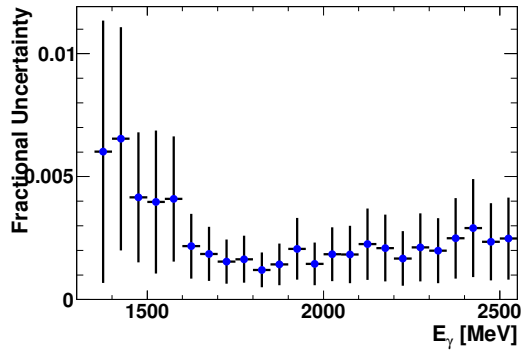
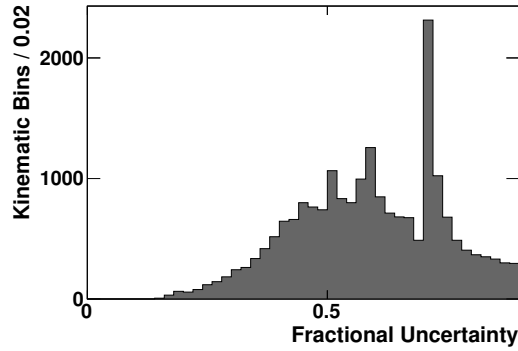(b) $\gamma p \to p\pi^0\pi^0$

(c) $\gamma p \to p\pi^0\eta$

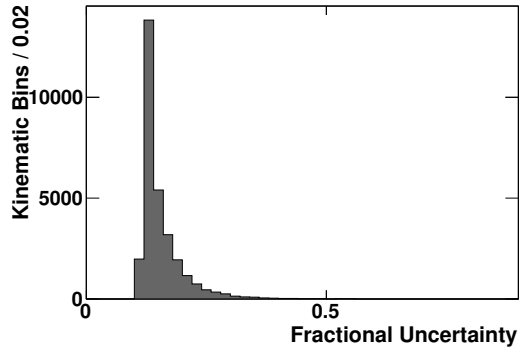Figure 8.7: $\gamma p \to p\pi^0\omega$ Background Reaction Uncertainty.

(a) $\gamma p \rightarrow p\omega$ Statistical

(b) $\gamma p \rightarrow p\omega$ Systematic

(c) $\gamma p \rightarrow p\pi^0\omega$ Statistical

(d) $\gamma p \rightarrow p\pi^0\omega$ Systematic

Figure 8.8: Summary of Uncertainty Values. Each value histogrammed represents one kinematic bin in the differential cross section. The extra peaks between 0.5 and 1.0 in (c) come from kinematic bins with very low statistics which cause rounding errors in the uncertainty calculation to occur.

CHAPTER 9

RESULTS

After a large effort to reconstruct each event and select the correct final state reaction, the experimentally measured and simulated events were used to measure physical observables. For the $\gamma p \rightarrow p\omega$ analysis, the differential cross sections and spin-density matrix elements are presented. For the $\gamma p \rightarrow p\pi^0\omega$ analysis, the differential cross sections presented as projections of select kinematic variables are shown. These observables have been subjected to an uncertainty analysis (Chapter 8) and these estimated uncertainties have been shown in each plot in this chapter.

These observables will be used in interpretation analyses to isolate the contributing baryon resonances. The differential cross sections for each analysis and the spin-density matrix elements for the $\gamma p \rightarrow p\omega$ reaction have been presented with full angular coverage and with an energy binning small enough to facilitate an interpretation analysis which will hopefully enable the isolation of the "missing" baryon resonances. The spin-density matrix elements will be used to separate processes and baryon resonances which produce an ω meson with different spin polarizations.

For all plots and discussions in this chapter, the units used are those where the speed of light c is set to $c = 1$. This means energy, momentum, and mass have the same units, electron volts (eV).

9.1 $\quad \gamma p \rightarrow p\omega$ Cross Sections

Figure 9.1 shows the final differential cross sections for the reaction $\gamma p \rightarrow p\omega$ measured at the CBELSA/TAPS experiment binned in $\cos\theta^\omega_{c.m.}$. The data are binned in 50 MeV wide energy bins from 1.15 to 2.5 GeV in initial photon energy. For $-1.0 < \cos\theta^\omega_{c.m.} < 0.8$, the angular bin width is 0.1. To show the differential cross section's strong forward angle peak, for points in the range $0.8 < \cos\theta^\omega_{c.m.} < 1.0$, the data are binned in 0.033 wide angle bins. The vertical bars on each point is the statistical uncertainty only. The systematic uncertainty is shown as a grey band at the bottom of each plot.

The low energy part of the cross sections shows a distribution which is mostly symmetric around $\cos\theta^\omega_{c.m.} = 0$ and consistent with baryon resonance production. At
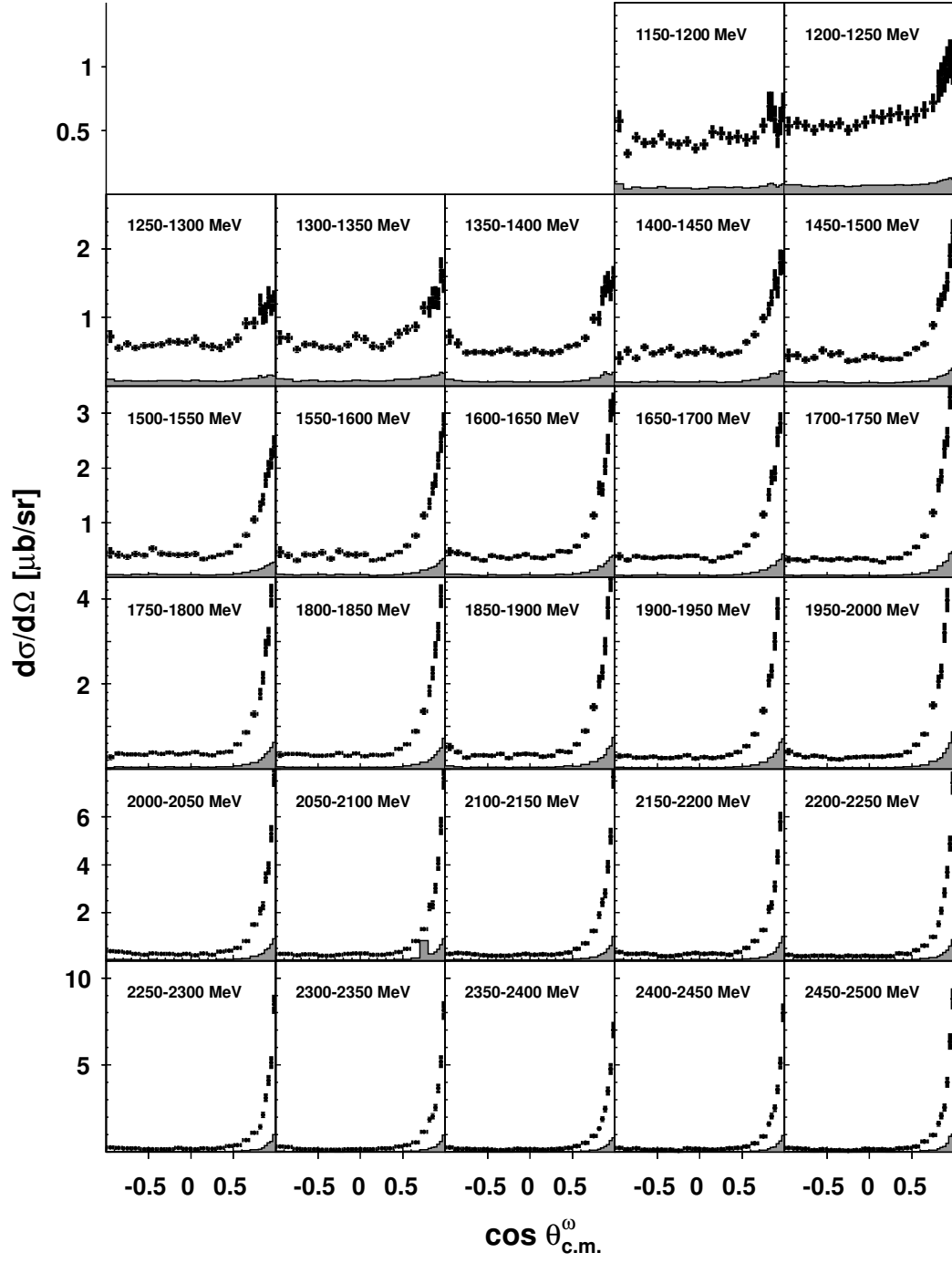
Figure 9.1: $\gamma p \to p\omega$ Differential Cross Sections versus $\cos\theta^{\omega}_{c.m.}$. Measured at the CBELSA/TAPS experiment. Each plot is labeled with its range in initial photon energy. The statistical error is shown as vertical bars on each data point and the systematic error is shown as a grey shaded area at the bottom of each plot.

107

Figure 9.2: $\gamma p \rightarrow p\omega$ Differential Cross Sections versus $\theta^{\omega}_{c.m.}$. Measured at the CBELSA/TAPS experiment. Each plot is labeled with its range in initial photon energy. The statistical error is shown as vertical bars on each data point and the systematic error is shown as a grey shaded area at the bottom of each plot.
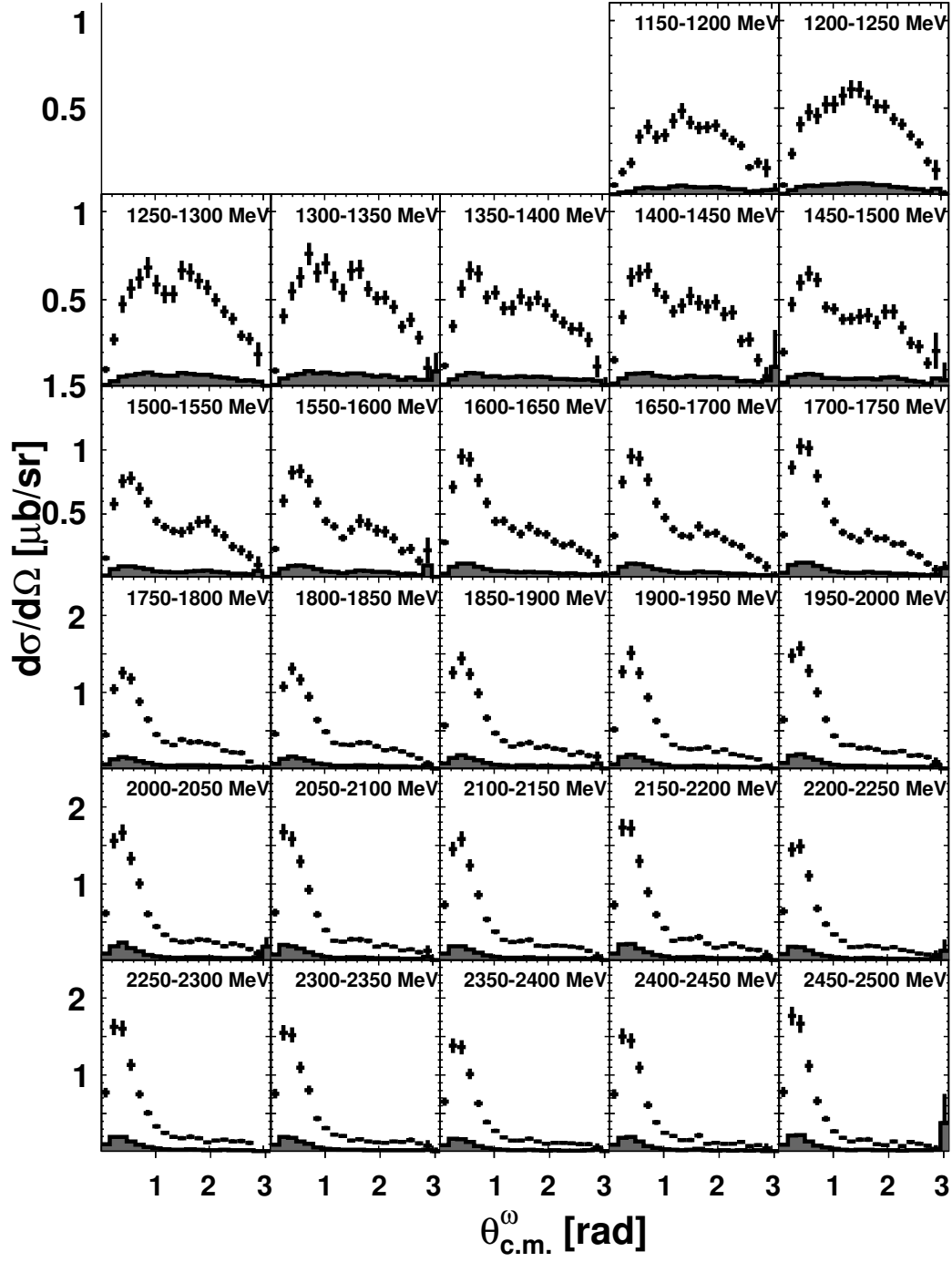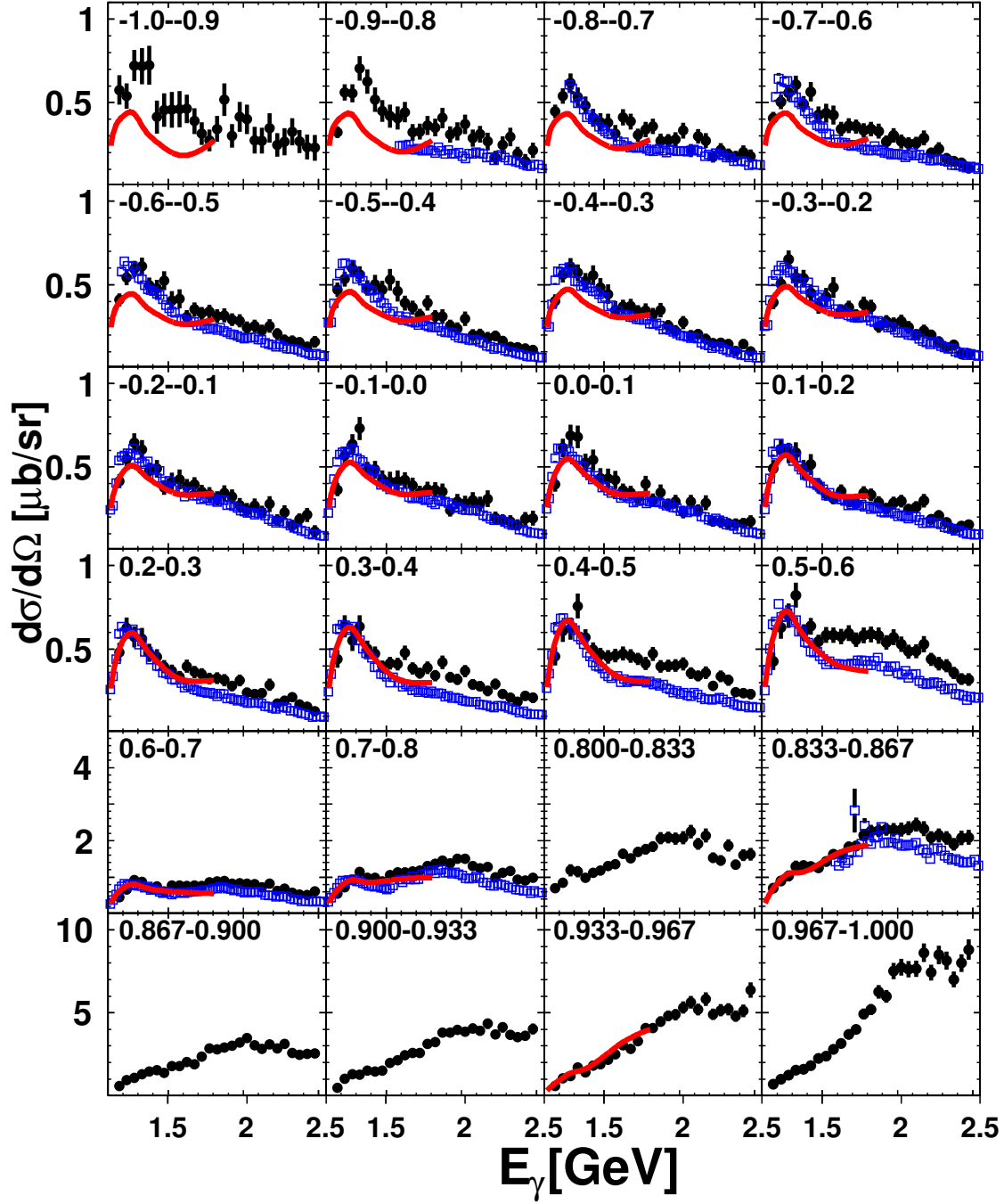
108

Figure 9.3: $\gamma p \rightarrow p\omega$ Excitation Functions. Measured at the CBELSA/TAPS experiment ($\bullet$). For comparison, the CLAS differential cross sections published in [14] are represented with a ($\square$). A coupled channel fit on data which included the SAPHIR differential cross sections [15] by the Gießen group published in [12] is represented with a (——).

higher energies, the differential cross sections show the forward angle rise (right side of each plot) which suggests a t-channel meson exchange. The backward angle portion of each plot does not show any significant increase indicating that a u-channel baryon exchange is not dominant.

Figure 9.2 shows the differential cross sections for the reaction $\gamma p \rightarrow p\omega$ measured by this analysis binned in $\theta^\omega_{c.m.}$. These results were derived from a separate analysis based on the same data. The same uncertainties and Q-factors were used in the two measurements but these measurements were treated separately otherwise. The data are binned in 50 MeV wide energy bins from 1.15 to 2.5 GeV in initial photon energy. The 20 angular bins for each energy had a width of 0.05π radians. The vertical bars on each point represent the statistical uncertainty only. The systematic uncertainty is shown as a grey band at the bottom of each plot.

The cross section decrease at the most forward angles are not a feature of the experiment but of the physics of this reaction. These measurements show the forward peak which is only visible when the data is binned finely in the forward angles. This forward peak is a feature of the t-channel meson exchange and can be used to fully characterize the strength of that process. This shows the advantage of these measurements have over previous measurements.

To facilitate comparison, the same differential cross section data have been shown as excitation functions in Figure 9.3 along with the CLAS differential cross sections published in [14]. The two measurements seem to have the same overall shape but the difference seems to be energy dependent. The only factor which is constant in an angular distribution and changes with energy is the photon flux normalization. Therefore this discrepancy suggests the problem arises from the photon flux normalization. However, there is little evidence to suggest which data set has the correct photon flux determination.

Figure 9.3 also shows the results from a coupled-channel effective Lagrangian analysis performed by the Gießen group and was published in 2005 [12]. This analysis included baryon resonances with spin up to 5/2 and was based on available data from πN scattering and γN scattering from the final states πN, $2\pi N$, ηN and ωN. Data with an initial photon energy range from the pion production threshold up to 2 GeV were analyzed. The only ω photoproduction data used in this fit were the SAPHIR differential cross sections and spin-density matrix elements. This fit shows how the backward angle fit underestimates the data from both experiments shown in this plot. This backward underestimation is from the SAPHIR differential cross section. By including the new data in this fit, the fit would be improved. This comparison shows how these types of analyses would be improved by using the newer data.

Since the differential cross sections do not have any acceptance holes, the total cross section shown in Figure 9.4 is formed by integration. The threshold peak in the total cross section shows the effect of the resonance production suggested by the low-energy, mostly symmetric angular distribution in the differential cross section. The high energy part of the total cross section shows a very broad peak. However, this peak is too broad to be associated with resonance production and indicates
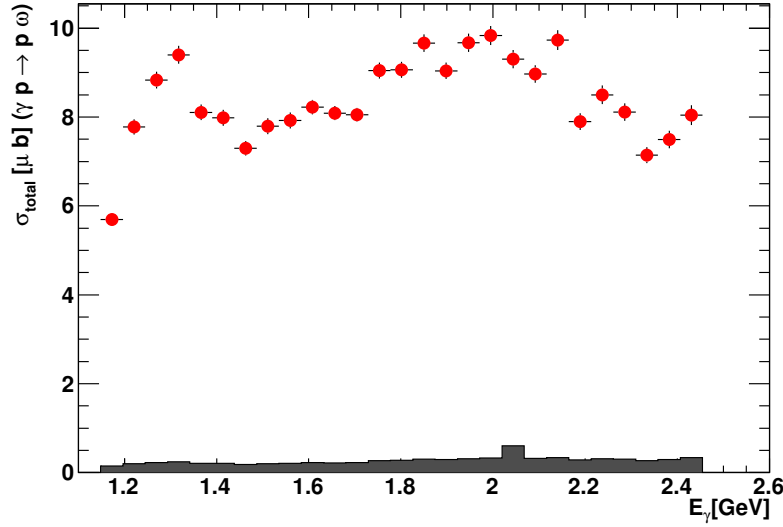
Figure 9.4: $\gamma p \to p\omega$ Total Cross Section. Measured at the CBELSA/TAPS experiment. The statistical error is shown as vertical bars on each data point and the systematic error is shown as a grey shaded area at the bottom of each plot.

that baryon resonance production is not the only process contributing. From the corresponding forward angle rise in the differential cross sections, this broad peak is probably an effect from the combination of t-channel meson exchange diagrams and baryon resonance production.

The low energy baryon resonance peak ($E_\gamma \sim 1700$ MeV) has been described by two separate interpretation analyses, the Gießen analysis [12] shown in Figure 9.3 and a partial wave analysis done just on the CLAS measurements [13], with the sub-threshold baryon resonance N(1680)$\frac{5}{2}^+$, a well established baryon resonance. However, each analysis differs on which other baryon resonance contributes. The inclusion of the differential cross sections in this section will help in pinning down the other contributions to the resonance peak by adding more data points in the forward scattering angles. These forward angle data points will help distinguish the resonance contributions from the growing meson exchange which could be ambiguous in the fit.

9.2 $\gamma p \to p\pi^0\omega$ Cross Sections

The differential cross sections have been measured for each kinematic binning defined in Table 7.2 and for the number of bins defined in Table 7.2. However, a multi-dimensional distribution is difficult to show. To emphasize some of the more interesting features in the differential cross sections, the plots in this section are focused on the variables which show the effects of the intermediate processes. These

variables are the $\cos\theta_{c.m.}$ variable (Section 9.2.1) and the $M_{b_1 b_2}$ invariant mass variable (Section 9.2.2).

To produce the plots shown in this section, all other kinematic variables have been integrated over. The uncertainties from each differential cross section point have been propagated to the plots. The integration provides a picture of the differential cross section which emphasizes the major features which can be expressed using each variable. For example, the cosine theta differential cross sections for a particle are useful for seeing the type of process in which that particle is produced in most of the time. An example of this, using an analogy to the $\gamma p \to p\omega$ differential cross sections, is if the cosine theta differential cross section for the ω meson, $\cos\theta^\omega_{c.m.}$, shows a forward angle rise, then that particle is involved in meson exchange (Figure 1.4d). The invariant mass differential cross sections are useful for identifying hadron resonances which dominantly decay to each pair of particles. For example, the invariant mass differential cross section binned in the invariant mass of the $p\pi^0$ system can show mass peaks belonging to baryon resonances decaying to $p\pi^0$.

9.2.1   Cosine Theta Differential Cross Sections

Figures 9.5, 9.6, and 9.7 show the differential cross section as a function of the cosine of the polar angle measured in the center-of-mass frame. This variable can be used to suggest the dominant processes contributing to the final state.

Figure 9.5 shows a forward angle rise in the $\cos\theta^\omega_{c.m.}$ differential cross sections which suggests meson exchange contributes strongly just as in the $\gamma p \to p\omega$ differential cross sections. However this meson exchange (Figure 1.4d) produces a baryon resonance which decays to $p\pi^0$. This resonance could be any resonance with isospin $I = 3/2$ or $1/2$.

Figure 9.6 shows constant differential cross section distributions when shown as a function of $\cos\theta^{\pi^0}_{c.m.}$. This symmetric distribution indicate the production of resonances. Combined with the shape of the $\cos\theta^\omega_{c.m.}$ differential cross sections, this again suggests meson exchange processes dominate. Since the $\Delta(1232)\frac{3}{2}^+$ resonance is usually seen decaying to $p\pi^0$, the shape is most likely dominated by this meson exchange with the π^0 meson being exchanged to create the $\Delta(1232)\frac{3}{2}^+$, which decays to $p\pi^0$.

Figure 9.7 shows the angular distribution of the scattered proton. This distribution is relatively flat in the low energy region ($E_\gamma < 1850$ MeV) suggesting the proton is mostly coming from baryon decays. At energies above $E_\gamma = 1850$ MeV, the distribution develops a backward rise. This backward rise indicates the proton is involved in a meson exchange (Figure 1.4f).

9.2.2   Invariant Mass Differential Cross Sections

The invariant mass differential cross sections can show peaks which indicate resonances which exist in the intermediate decays. However due to interference effects,
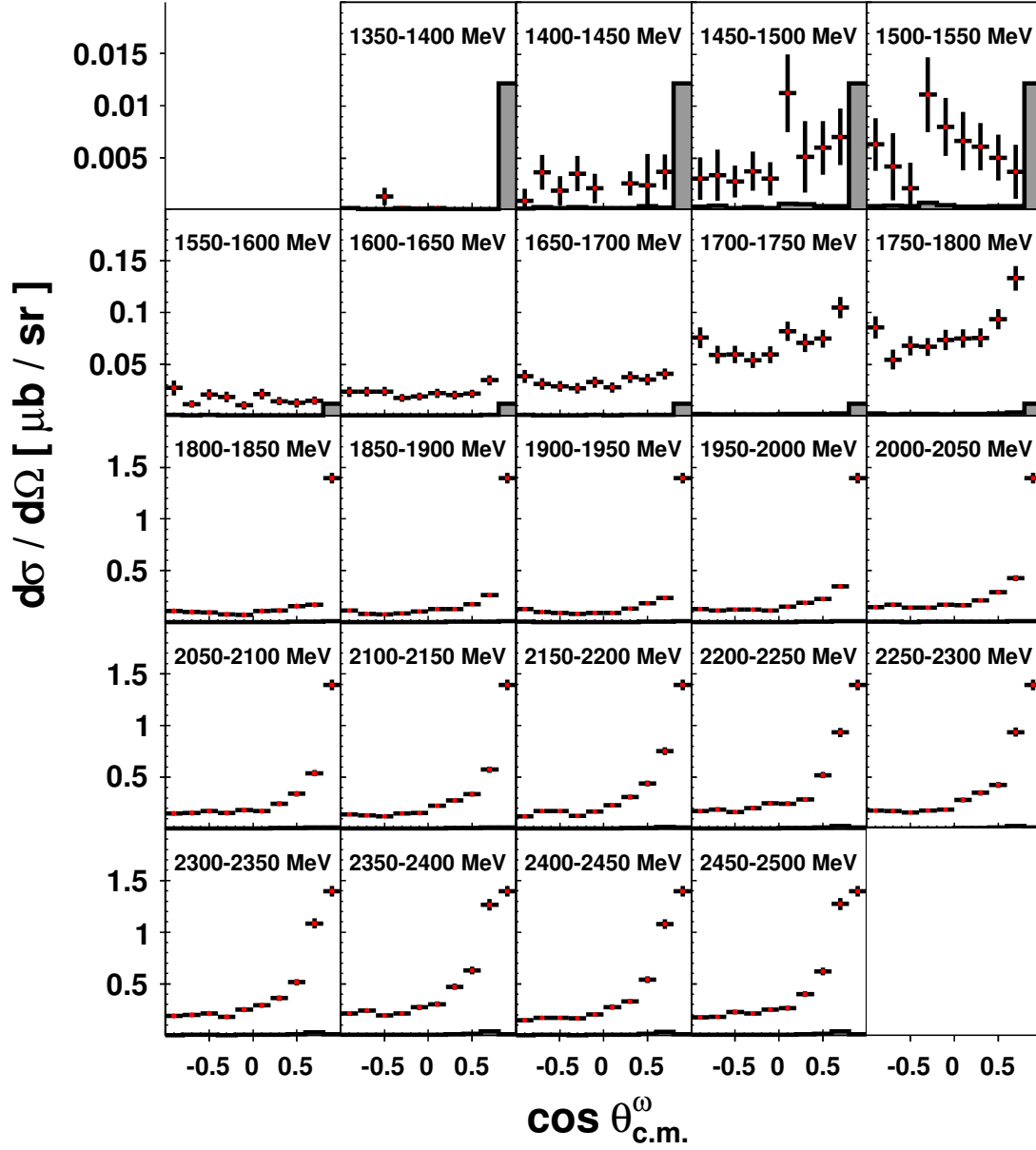
Figure 9.5: $\gamma p \rightarrow p\pi^0\omega$ $\cos\theta^\omega_{c.m.}$ Differential Cross Sections. Measured at the CBELSA/TAPS experiment defined in the $\omega_{c.m.}$ kinematic variable set. Each plot is labeled with its range in initial photon energy. The statistical error is shown as vertical bars on each data point and the systematic error is shown as a grey shaded area at the bottom of each plot.
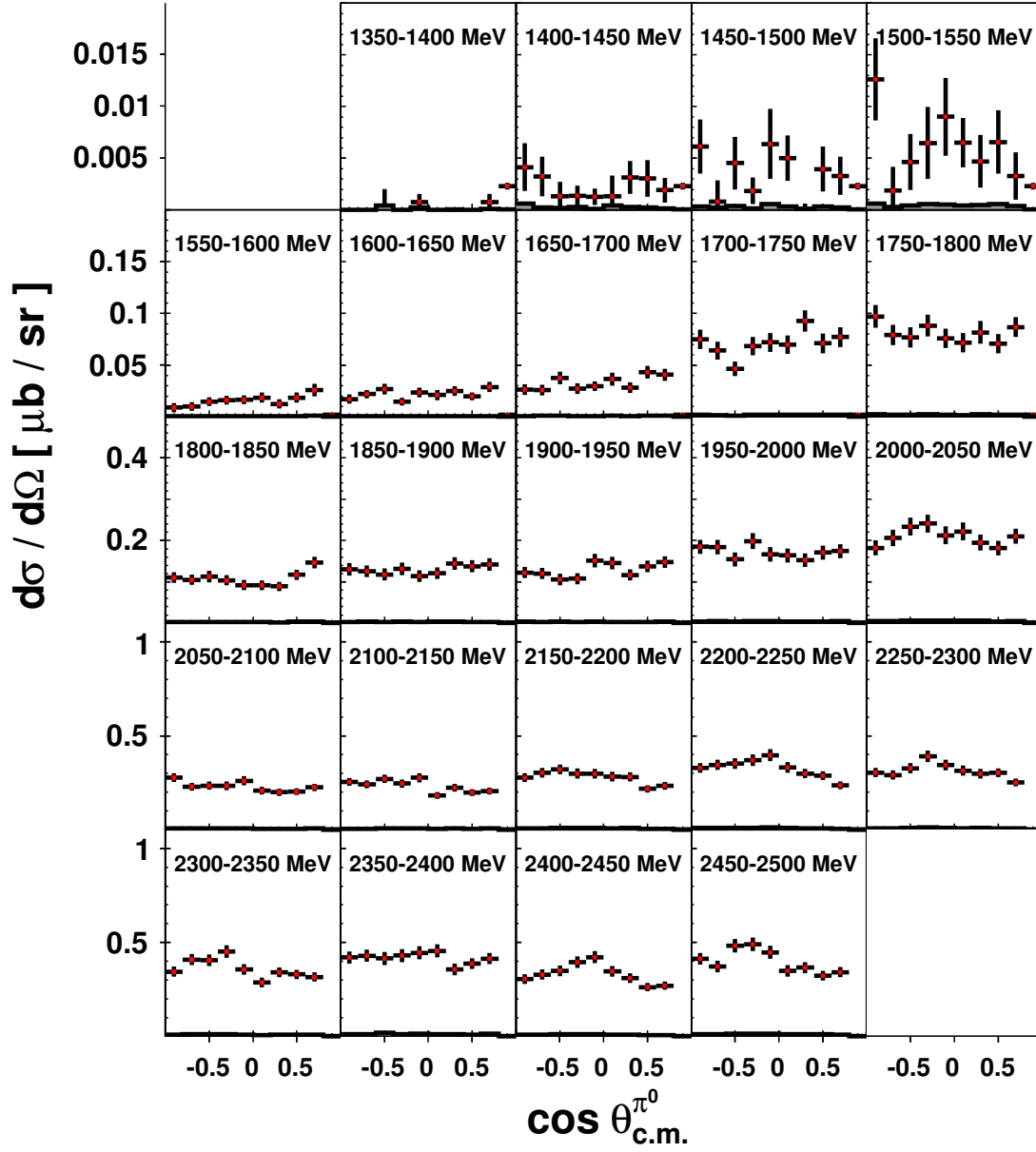
Figure 9.6: $\gamma p \rightarrow p\pi^0\omega \; \cos\theta_{c.m.}^{\pi^0}$ Differential Cross Sections. Measured at the CBELSA/TAPS experiment defined in the $\pi^0_{c.m.}$ kinematic variable set. Each plot is labeled with its range in initial photon energy. The statistical error is shown as vertical bars on each data point and the systematic error is shown as a grey shaded area at the bottom of each plot.

Figure 9.7: $\gamma p \rightarrow p\pi^0\omega$ $\cos\theta^p_{c.m.}$ Differential Cross Sections. Measured at the CBELSA/TAPS experiment defined in the $p_{c.m.}$ kinematic variable set. Each plot is labeled with its range in initial photon energy. The statistical error is shown as vertical bars on each data point and the systematic error is shown as a grey shaded area at the bottom of each plot.
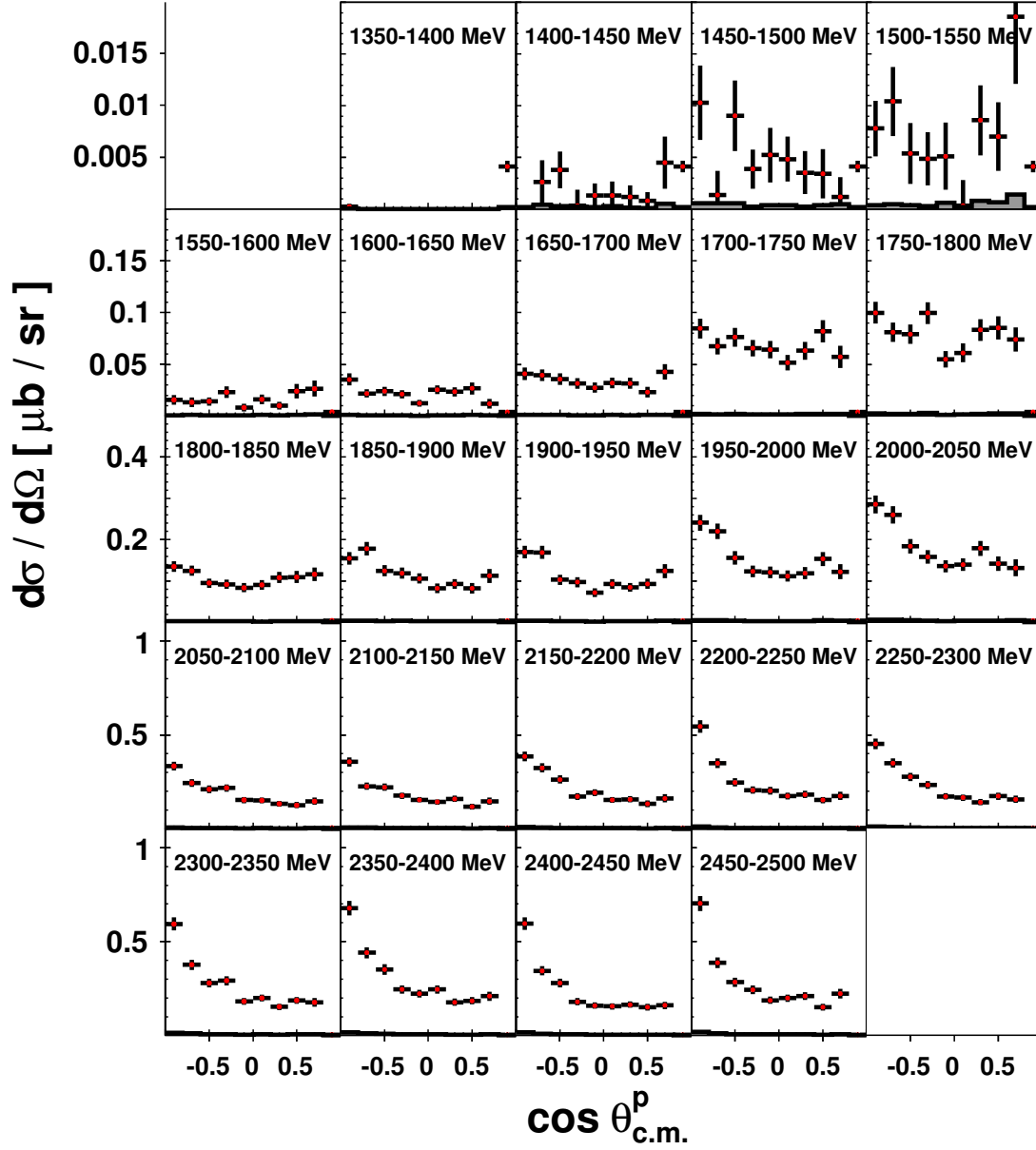
not all the contributing resonances exhibit a peak structure. The peaks seen in these plots are the resonances which dominate the reaction at those kinematic variable values. It is likely more hadron resonances contribute to this reaction than are obvious in these plots.

Each invariant mass differential cross section shown in this section belongs to the same kinematic binning as a cosine theta differential cross section in the previous section. Since we are describing the $\gamma p \to p\pi^0\omega$ reaction, the cross sections binned in $M_{b_1 b_2}$ invariant mass and the $\cos\theta_{c.m.}^a$ angle, where b_1, b_2, and a are all different particles, are projections describing the same differential cross section. For example, the differential cross sections binned in $M_{p\pi^0}$ shown in Figure 9.8 and in the cosine theta differential cross sections binned in $\cos\theta_{c.m.}^\omega$ shown in Figure 9.5 describe the same differential cross section binned with the kinematic binning denoted with $\omega_{c.m.}$.

Figure 9.8 shows the $p\pi^0$ invariant mass differential cross sections with a resonance peak around 1200 MeV in mass. The size and position of this peak suggests the $\Delta(1232)\frac{3}{2}^+$ resonance is involved relatively often in this final state. When combined with the strength of the meson exchange process suggested in the $\cos\theta_{c.m.}^\omega$ differential cross sections (Figure 9.5) and the large $p\pi^0$ decay fraction of the $\Delta(1232)\frac{3}{2}^+$ resonance, the process described by Figure 1.4d with the π^0 meson as the exchange particle and the $\Delta(1232)\frac{3}{2}^+$ as the baryon resonance must happen a large fraction of the time.

The $p\omega$ invariant mass differential cross sections are shown in Figure 9.9. These distributions also suggest at least one resonance at around 1700 MeV in mass and likely correspond to the same baryon resonances seen in the $\gamma p \to p\omega$ cross sections in the previous section.

Figure 9.10 does not show any dominant peaks in the $\pi^0\omega$ invariant mass differential cross sections. However at around 1200 MeV in mass, the $b_1(1235)$ meson should be seen and corresponds to a small ripple in these distributions. Around the same incoming photon energy where the $b_1(1235)$ meson begins to be produced, the differential cross section binned in $\cos\theta_{c.m.}^p$ (Figure 9.7) shows a backward rise. These two occurrences *could* be due to a meson exchange like in Figure 1.4f. A more sophisticated analysis must be performed to confirm this hypothesis however.

9.2.3 Total Cross Section

The total cross section for the $\gamma p \to p\pi^0\omega$ analysis (■) is measured by integrating over all the kinematic bins for each energy bin and is shown in Figure 9.11. This distribution shows a smooth increase and is similar in overall shape to the total cross section reported by the CB-ELSA collaboration in [16] (●). The new data significantly improve the energy resolution of the total cross section with much smaller uncertainty. The data presented are useful for an interpretation analysis to isolate the "missing" baryon resonances above 1800 MeV in mass ($E_\gamma \sim 2060$ MeV).
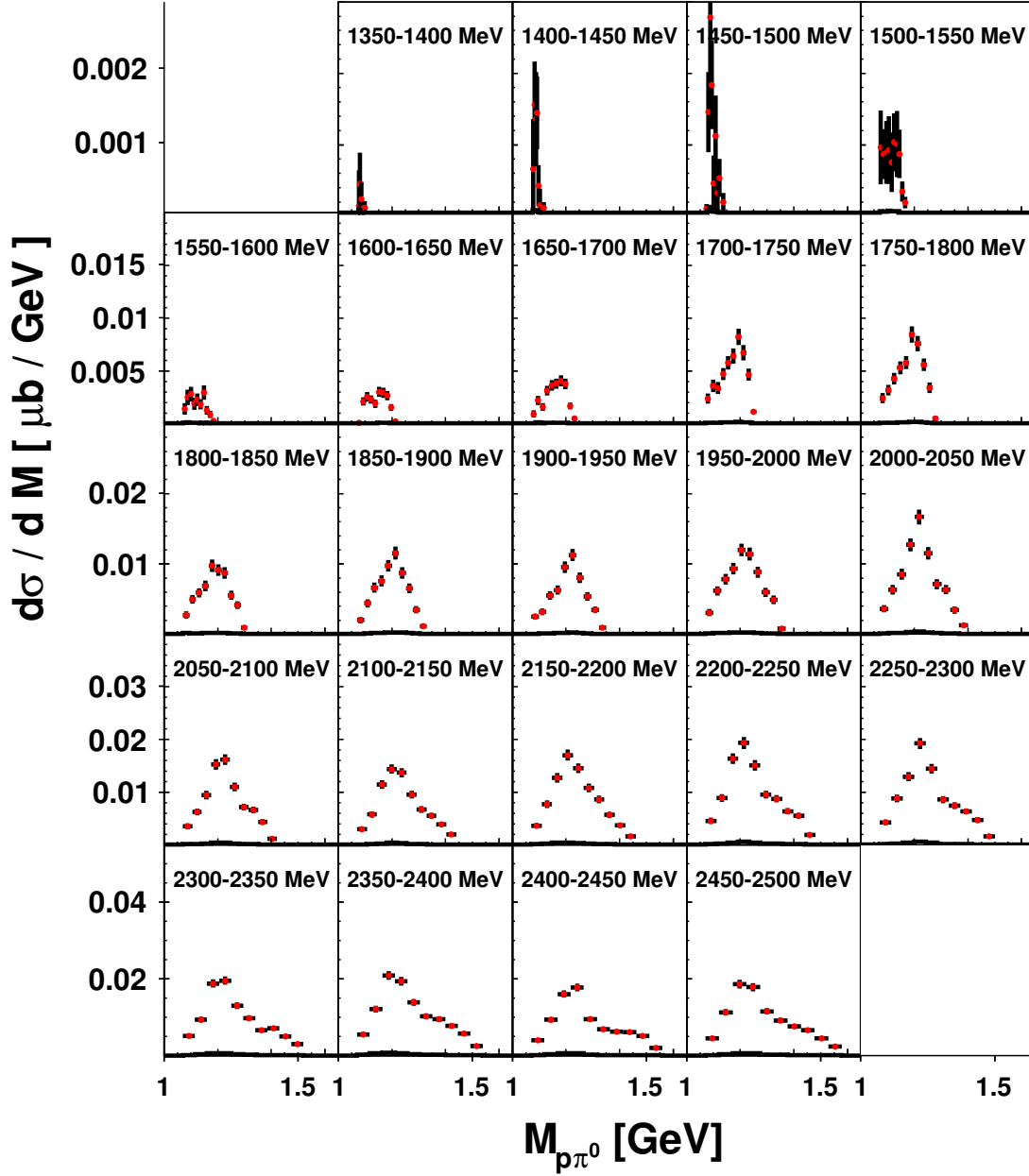
Figure 9.8: $\gamma p \rightarrow p\pi^0\omega$ $M_{p\pi^0}$ Differential Cross Sections. Measured at the CBELSA/TAPS experiment defined in the $\omega_{c.m.}$ kinematic variable set. Each plot is labeled with its range in initial photon energy. The statistical error is shown as vertical bars on each data point and the systematic error is shown as a grey shaded area at the bottom of each plot.

Figure 9.9: $\gamma p \rightarrow p\pi^0\omega$ $M_{p\omega}$ Differential Cross Sections. Measured at the CBELSA/TAPS experiment defined in the $\pi^0_{c.m.}$ kinematic variable set. Each plot is labeled with its range in initial photon energy. The statistical error is shown as vertical bars on each data point and the systematic error is shown as a grey shaded area at the bottom of each plot.
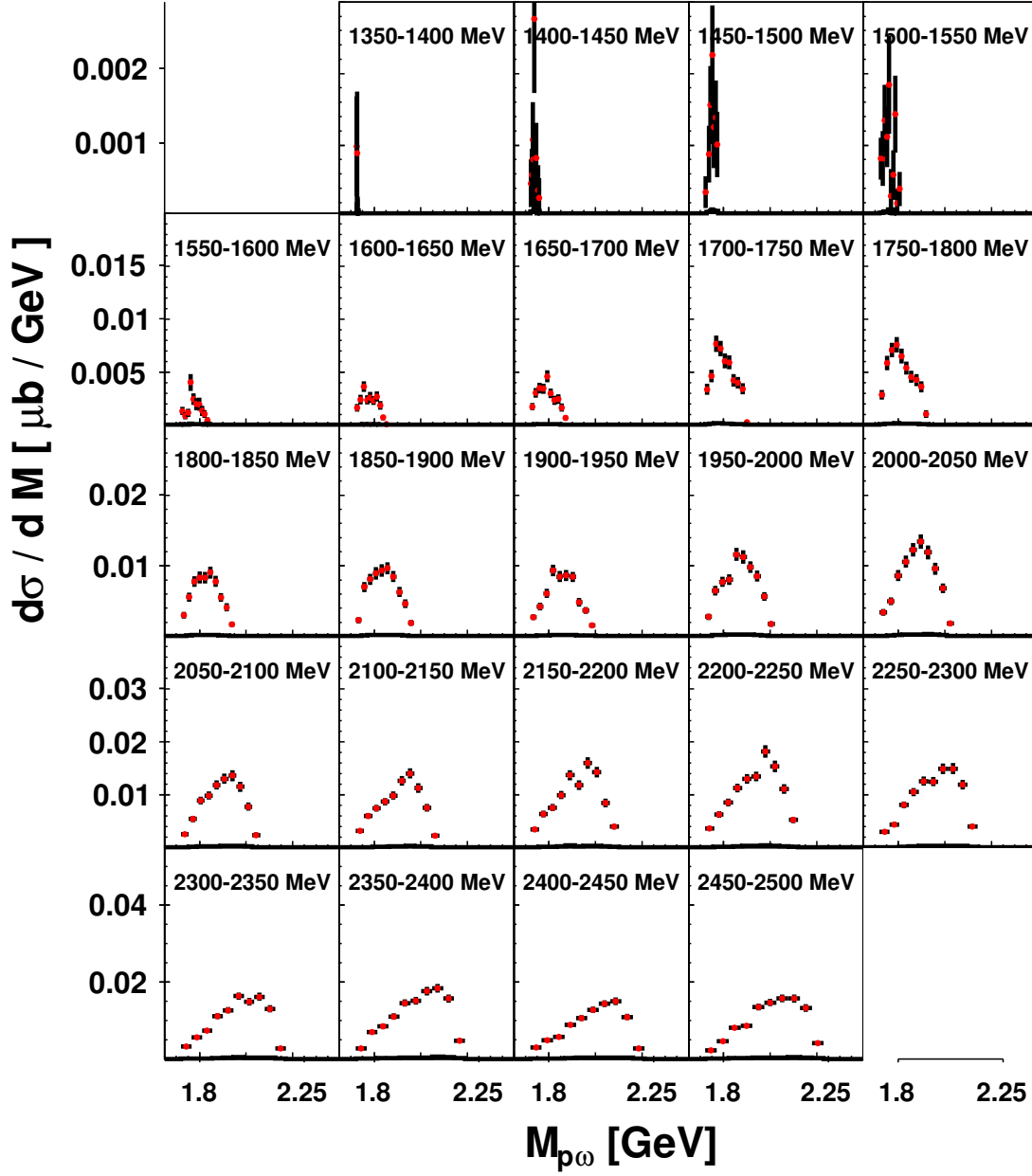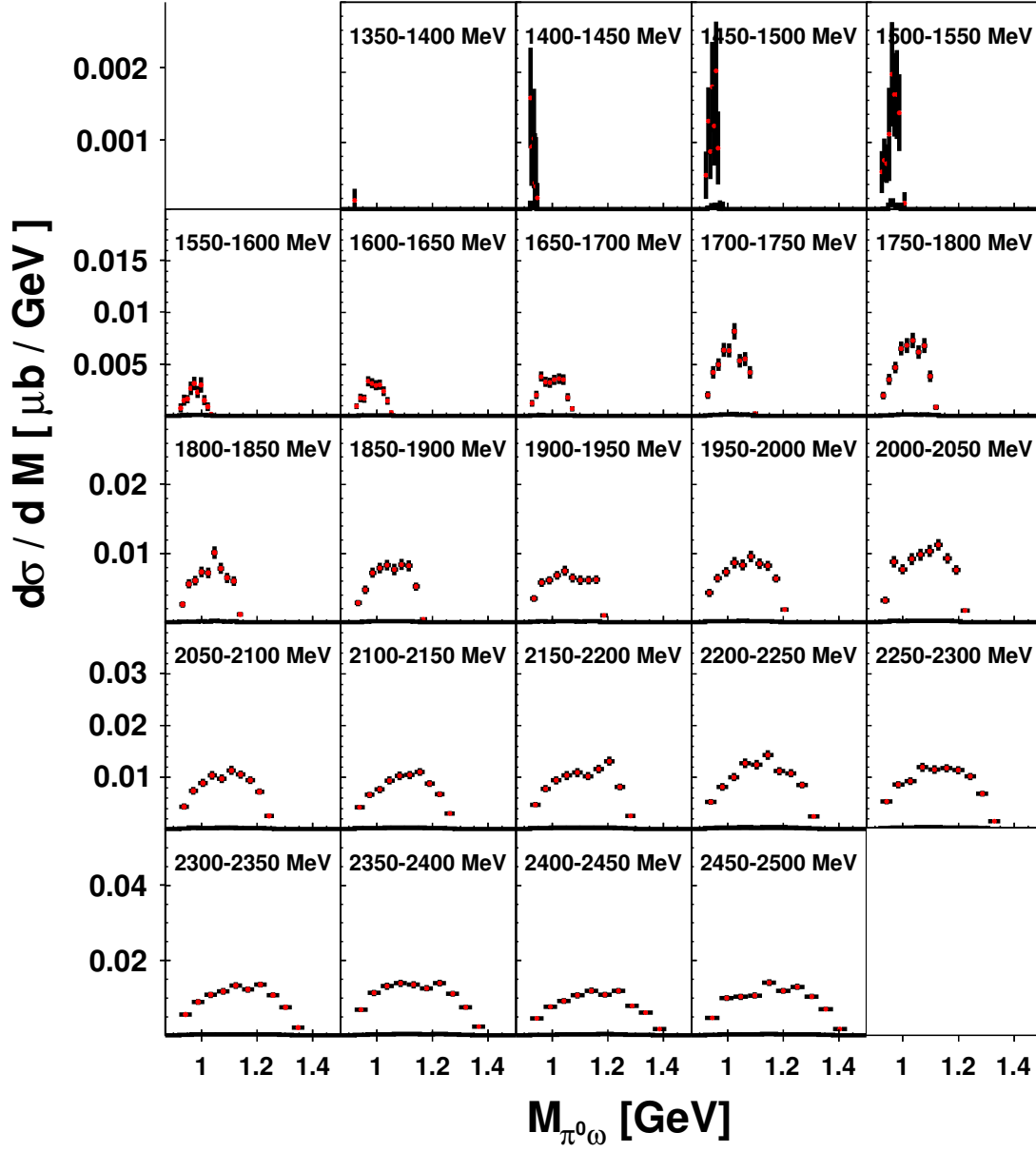
Figure 9.10: $\gamma p \rightarrow p\pi^0\omega$ $M_{\pi^0\omega}$ Differential Cross Sections. Measured at the CBELSA/TAPS experiment defined in the $p_{c.m.}$ kinematic variable set. Each plot is labeled with its range in initial photon energy. The statistical error is shown as vertical bars on each data point and the systematic error is shown as a grey shaded area at the bottom of each plot.

Figure 9.11: $\gamma p \rightarrow p\pi^0\omega$ Total Cross Section. Measured at the CBELSA/TAPS experiment (■). The statistical error is shown as vertical bars on each data point and the systematic 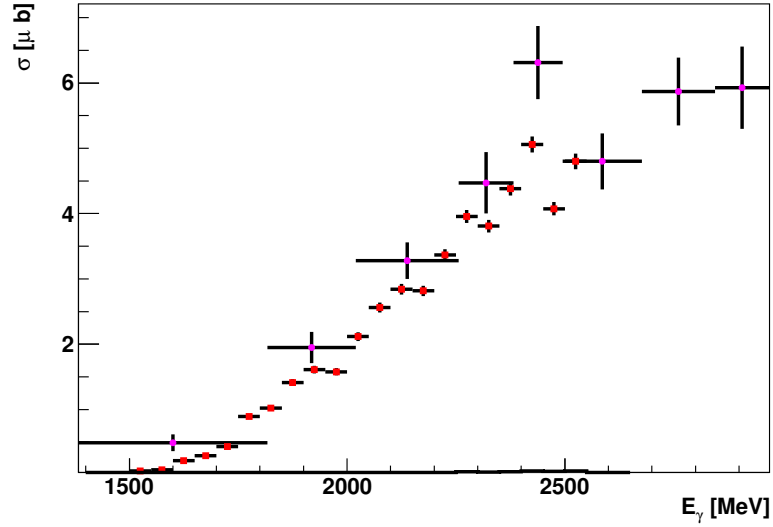error is shown as a shaded area at the bottom of each plot. The total cross section measured by the CB-ELSA collaboration in [16] are represented with a (●) with the statistical uncertainties represented as vertical bars on each point.

9.3 $\gamma p \rightarrow p\omega$ Spin-Density Matrix Elements

Additional information about the processes leading to this final state can be obtained by analyzing the decay products of the ω meson. The density of the spin quantizations of the ω meson in the overall amplitude can be extracted by analyzing the angular distribution of the decay products. The unpolarized spin-density matrix elements (SDME) are discussed and shown in Section 9.3.1. The linearly polarized SDMEs, ρ_{00}^1 and ρ_{11}^1, are discussed and shown in Section 9.3.2.

9.3.1 Unpolarized Spin-Density Matrix Elements

The angular decay distributions of the decay products as a function of the unpolarized spin density matrix elements (ρ^0) is given by Equation 7.13. The coordinate systems in which these angles are measured in this analysis are the helicity, Gottfried-Jackson and Adair coodinate systems (defined in Section 7.2).

The events used in this analysis are the same exact events used for the $\gamma p \rightarrow p\omega$ differential cross sections. The events were separated into 100 MeV wide energy bins measured in initial photon energy from 1200 MeV to 2500 MeV and into two $\cos\theta_{c.m.}^\omega$ bins. The events in each of these bins were filled into an angular distribution
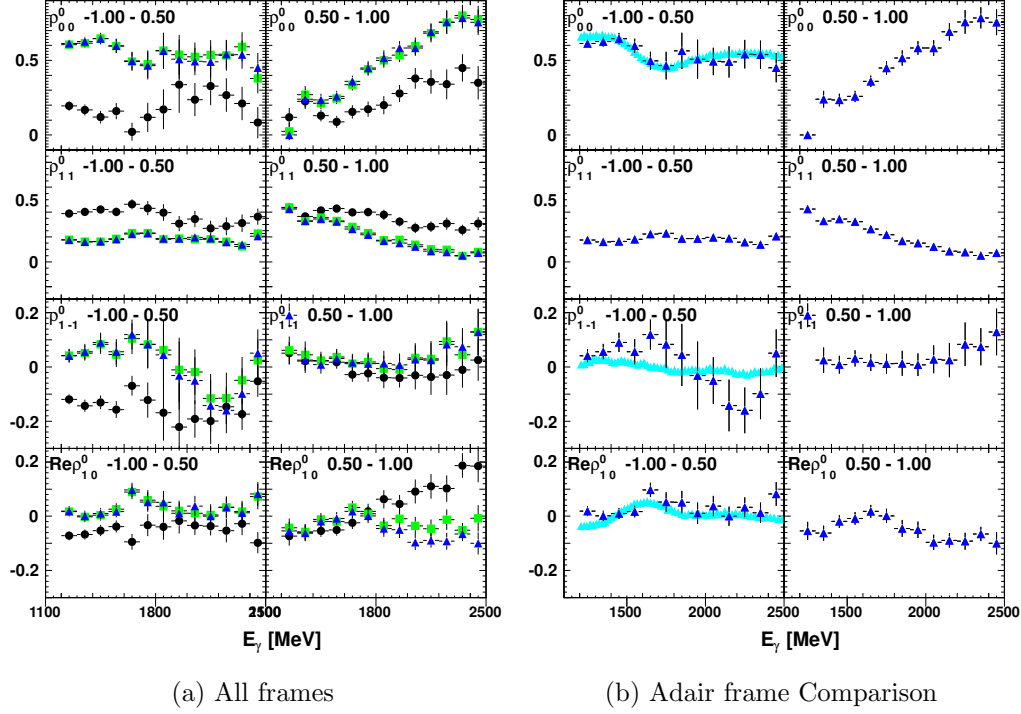
Figure 9.12: $\gamma p \to p\omega$ Unpolarized Spin Density Matrix Elements. (a) The SDMEs for all three frames are shown. (b) The SDMEs for the Adair frame are shown for comparison. The SDMEs measured from this analysis are shown in the helicity system (●), Gottfried-Jackson system (■), and Adair system (▲). The SDMEs in the Adair system from CLAS (□) are shown in (b) and are an average over the corresponding angular range. Each plot shows the spin density matrix element name along with its range in cosine of the polar angle of the ω in the center-of-mass frame.

which had 6 $\cos\theta_d$ bins and 8 ϕ_d bins, the decay angles of the final state photon in the $\omega \to \pi^0\gamma$ decay.

The Q-factor values were used when filling the angular distributions with the experimentally measured events. The bins were filled according to Equation 7.19. For each bin in these distributions, the Q-factor fit uncertainties (Section 8.3.2) and Monte Carlo simulation uncertainties (Section 8.2) were propagated to the uncertainty for each bin.

To extract the spin-density matrix elements (SDMEs), the angular distributions are fitted using a χ^2 minimization fit. The ρ^0_{00} was restricted to values between 0 and 1. The rest of the SDMEs were restricted to between -1 and 1.

The spin density matrix elements (SDMEs) extracted from the events selected for the $\gamma p \to p\omega$ analysis are shown in Figure 9.12a. The uncertainties associated with each point are shown as vertical bars and are the result of the propagation of

the uncertainties of each bin in the angular distribution to the parameters by the χ^2 minimization fit.

The Gottfried-Jackson system and the Adair system each have its z-axis defined by the momentum direction of the incoming photon. The difference being which reference frame that momentum is measured in. The Adair system z-axis is defined in the center-of-mass frame. The Gottfried-Jackson system z-axis is defined in the rest frame of the ω meson. If the momentum of the ω meson in the center-of-mass frame is close to zero, then these two systems are nearly the same. Therefore, the SDMEs for these two systems should be roughly the same for measurements done close to the threshold. As the momentum of the ω momentum in the direction perpendicular to the momentum of the initial photon grows, these measurements could diverge. The similarity of the Gottfried-Jackson system data and Adair system data at low incoming photon energies is due to the low momentum of the ω meson in the center-of-mass frame transverse to the momentum of the initial photon.

For comparison to earlier measurements, Figure 9.12b shows the CLAS spin density matrix elements published in [14] (□) along with the data from this analysis extracted in the Adair system (▲). Since the CLAS data have much better statistics than these data, the CLAS data were averaged over the same angular range. The CLAS data do not extend all the way to the most forward angles. Therefore, the CLAS data were not presented for comparison in the forward angles. The agreement with the CLAS data is very good and suggests the discrepancies shown in the differential cross sections (Figure 9.3) are not present in this comparison. Since there is no photon flux normalization involved in the determination of the spin density matrix elements, the discrepancy in the cross section is likely due to photon flux normalization.

The areas where the reported data improves the world database is in its angular coverage and its extraction from the radiative decay. These data have fairly good energy resolution while also being sensitive to the distribution in the most forward angular range. The extraction of these data from the radiative decay provides an independent check of the previously measured data through an alternate channel.

9.3.2 Polarized Spin-Density Matrix Elements

The events from each of the two polarized data sets were treated separately and separated into the same energy and $\cos\theta^{\omega}_{c.m.}$ bins as the unpolarized SDMEs. To extract the polarized SDMEs, the angle between the polarization vector of the initial photon and the production plane[1] (Φ_{pol}) must be defined and added to the angular distribution. If this angle is ignored and treated the same way as the unpolarized data, the unpolarized SDMEs can be extracted. To ensure the acceptance is the same and these data are consistent with the unpolarized data, the unpolarized SDMEs were extracted using exactly the same procedure as in Section 9.3.1.

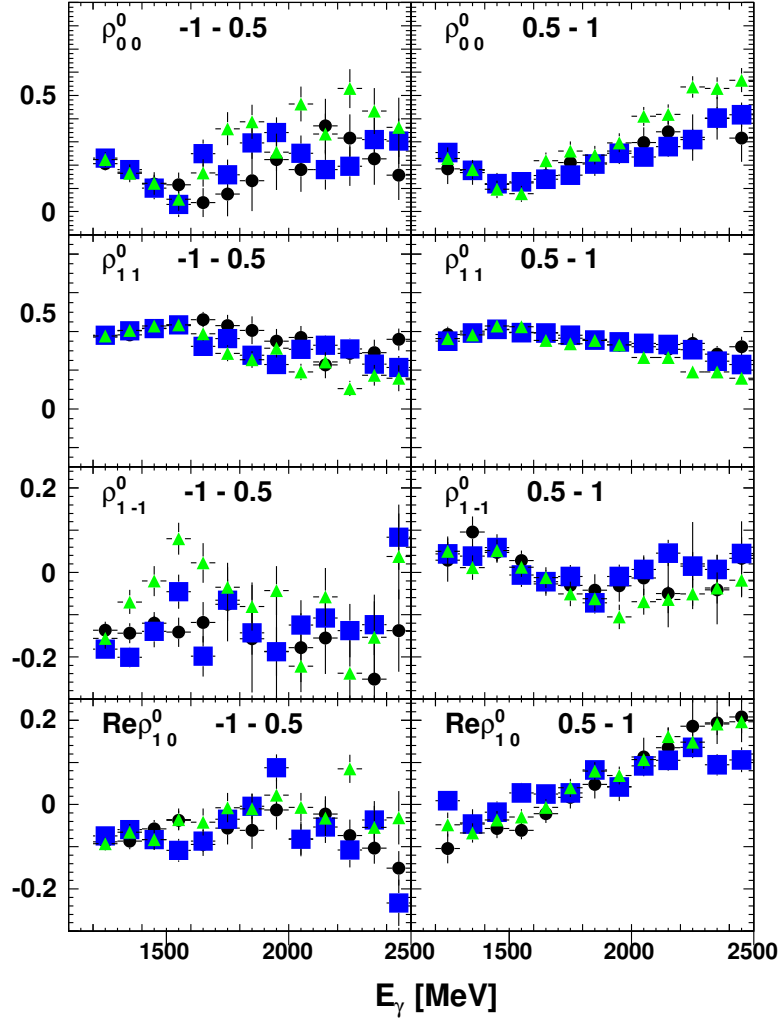[1] defined by the final state proton and the ω meson

Figure 9.13: Unpolarized Spin-Density Matrix Elements Crosscheck with Polarized Data. These SDMEs are defined in the helicity system. The unpolarized SDMEs extracted from the unpolarized data (●), March 2003 polarized data (■), and May 2003 polarized data (▲). Each plot shows the spin density matrix element name along with its range in cosine of the polar angle of the ω in the center-of-mass frame.

The unpolarized SDMEs extracted in the helicity system are plotted in Figure 9.13. The comparison of SDMEs extracted from the polarized datasets (■,▲) and the unpolarized dataset (●) shows a fair agreement within statistical uncertainties. The polarized data sets have significantly fewer events than the unpolarized data set. The smaller statistics resulted in increased statistical fluctuations in the extracted SDMEs from the polarized data sets. However, in the low energy region ($E_\gamma < 1700$ MeV) the agreement is decent.
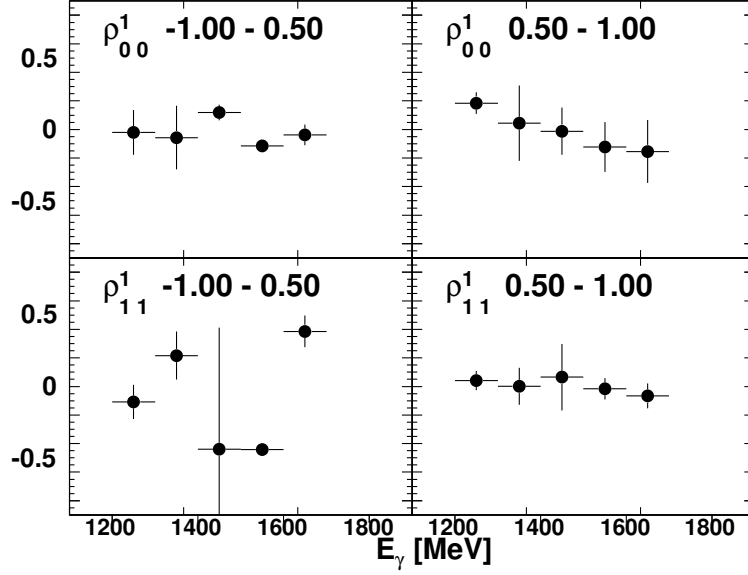
Figure 9.14: Polarized Spin-Density Matrix Elements in the Helicity System. The low energy data points (1200 - 1400 MeV) were extracted from the March 2003 data. The higher energy data points were extracted from the May 2003 data. Each plot shows the spin density matrix element name along with its range in cosine of the polar angle of the ω in the center-of-mass frame.

To extract the polarized SDMEs, ρ_{00}^1 and ρ_{11}^1, the events in each initial photon energy and $\cos\theta_{c.m.}^\omega$ bin was filled into a three-dimensional angular distribution. The angular distribution has 5 Φ_{pol}, 5 $\cos\theta_d$, and 12 ϕ_d bins and was acceptance corrected and normalized according to Equation 7.19 . These angular distributions were fitted to Equation 7.16 using a χ^2 minimization fit. Before fitting, the ϕ_d was integrated over and the unpolarized SDMEs were fixed to the values from the fits on unpolarized data. The unpolarized SDMEs were determined with smaller uncertainty in the unpolarized data and have the same values in the polarized fits as shown in Figure 9.13. Equation 7.16 was modified by integrating over the ϕ_d variable before fitting. The values of the polarized SDMEs were restricted using the restrictions in [10] and are based on the values of the unpolarized SDMEs.

Figure 9.14 shows the polarized SDMEs extracted from the polarized data. Due to the magnitude of the degree of polarization, the SDMEs for an energy bin could only be extracted from the dataset with a significant degree of polarization. In this analysis, the threshold for a significant degree of polarization is 0.2 (shown in Figure 6.20) and only fits were done for energy bins with polarizations exceeding this value.

These measurements mark the first time these SDMEs have been shown. The values are small and close to zero.

CHAPTER 10

CONCLUSIONS

The photoproduction of ω mesons and $\pi^0\omega$ meson pairs off of protons was studied using data measured at the CBELSA/TAPS experiment in Bonn, Germany. The motivation for studying these reactions is to find baryon resonances contributing to these reactions.

Unpolarized photons were produced through bremstrahlung reactions by scattering 3.175 GeV electrons from the ELSA accelerator off of a copper radiator. The resulting bremstrahlung electrons were analyzed by the Tagger hodoscope to tag each initial photon with an energy and time. The unpolarized photons were then incident upon a stationary target of liquid hydrogen which supplied the unpolarized protons. Hadronic reactions decaying to mesons were produced and the decay photons from those mesons were detected in the calorimeter detectors, Crystal Barrel and TAPS. The crystals in the calorimeter detectors were optimized to measure photon energies and positions. Any charged particles produced in any reactions were detected by scintillating materials and were combined with the spatially corresponding calorimeter signals to identify any non-photon calorimeter signals.

Photons were reconstructed from their energy deposits in the calorimeter crystals. Using those reconstructed photons, π^0 mesons and protons were reconstructed by using a kinematic fitting method. The ω meson was identified using invariant masses reconstructed from $\pi^0\gamma$ combinations. The final state contributions were deduced by using an event-based probabilistic method called the Q-factor method.

The search for baryon resonances was motivated by the discrepancy between the current number of experimentally verified resonances and theoretically predicted resonances from constituent quark models. The relatively large number of "missing" predicted states caused experimental physicists to resort to using photon beams to produce baryon resonances, due to studies suggesting these missing states could be found there. The couplings of some of these "missing" baryon states to the ω meson in the final state were predicted to be non-negligible in [5, 7, 8].

There have been several measurements of the differential cross sections and spin-density matrix elements for the $\gamma p \to p\omega$ reaction, but the angular coverage has been incomplete or the mass resolution has been too poor for these measurements to be used to maximally separate the non-resonant processes from the effect of the baryon

resonances. The almost 98% solid angle detector coverage of the CBELSA/TAPS experiment allows this analysis to improve on the existing information on this reaction.

There have also been discrepancies discovered between these previous $\gamma p \rightarrow p\omega$ measurements which will effect the solutions of analyses trying to isolate baryon resonances. To investigate the causes of these discrepancies, new independent measurements like the measurements in this analysis will help resolve these issues. We have discovered an energy dependent normalization discrepancy between the differential cross sections measured in this analysis and those measured by the CLAS collaboration [14]. This discrepancy is most likely due to each measurement's determination of the number of photons which had the opportunity to create a reaction, photon flux. This hypothesis is gathered by comparing the results for the differential cross sections, which depend on the photon flux, and the spin-density matrix elements, which do not rely on photon flux. The comparison of spin-density matrix elements from this analysis and the CLAS collaboration match very well. Also, the discrepancy between the differential cross sections seem to have a dependence on incoming photon energy only, which matches the signature of a discrepancy in photon flux.

The $\gamma p \rightarrow p\pi^0\omega$ reaction at these energies has only been measured once before with small statistics. This analysis has been able to reconstruct significantly more events which allows the measurement of differential cross sections with enough quality to be used in isolating baryon resonances for the first time.

The differential cross sections for the $\gamma p \rightarrow p\omega$ and $\gamma p \rightarrow p\pi^0\omega$ reactions were measured and presented. The mass resolution and angular coverage are sufficient to isolate baryon resonances. In the differential cross section distributions, the dominant processes can be deduced. The low energy $\gamma p \rightarrow p\omega$ cross section indicates baryon resonance production. At higher energies ($E_\gamma > 1.5$ GeV), this reaction is dominated by t-channel meson exchange. The $\gamma p \rightarrow p\pi^0\omega$ differential cross section suggests the same sort of meson exchange process, but also indicates there is some baryon resonance production in the intermediate decays.

The $\gamma p \rightarrow p\pi^0\omega$ reaction differential cross sections also show a hint of $b_1(1235)$ meson production. When examining the behavior of the cross sections as the reaction reaches the production threshold for the $b_1(1235)$ meson, there is a possibility that this meson is involved in a meson exchange process.

While these differential cross sections can be useful for seeing the dominant contributions, there are many processes and baryon resonances which contribute and will require a more sophisticated analysis to isolate. There are several baryon resonances with little or no evidence for existence which have the chance to be isolated using these data.

The unpolarized spin-density matrix elements were extracted for the $\gamma p \rightarrow p\omega$ reaction from the same data by fitting angular distributions in the helicity, Gottfried-Jackson, and Adair systems. For the first time these elements were extracted from the radiative decay of the ω meson and for all angles with small enough incoming photon energy bins useful for isolating "missing" baryon resonances. The polarized

126

spin-density matrix elements were also extracted for the $\gamma p \to p\omega$ reaction from linearly polarized photon beam data. Values are reported for the first time for the ρ^1_{00} and ρ^1_{11} SDMEs. The addition of these SDMEs in interpretation analyses will help separate processes and baryon resonances with different quantum numbers.

The combination of the CLAS data and the data presented here also present an opportunity to study the effect of final state interactions. Since the data presented in this paper were reconstructed from the $\omega \to \pi^0\gamma$ decay and the CLAS data were reconstructed using the $\omega \to \pi^+\pi^-\pi^0$ decay, the re-scattering of the charged pions can be studied.

The data presented in this thesis will certainly improve the world data set in regards to ω meson photoproduction. This improvement will make it possible to isolate the "missing" baryons which contribute with more precision. The existing analyses which attempt to isolate baryon resonances (interpretation analyses), like the coupled-channel effective Lagrangian analysis by the Gießen group [12], will improve when the information in the forward scattering angles from this analysis is added to the fits. This new data will hopefully spark a new round of interpretation analyses on ω meson photoproduction in both the $\gamma p \to p\omega$ reaction and the $\gamma p \to p\pi^0\omega$ reaction. These new analyses will shed new light on the baryon resonances which contribute and hopefully help solve the "missing" baryon problem.

APPENDIX A

ACCEPTANCE CORRECTION PROJECTIONS FOR THE $\gamma p \to p\pi^0\omega$ ANALYSIS

The acceptance correction is the factor which accounts for the fraction of the desired reaction events not seen by the analysis. This is done by generating Monte Carlo simulated events which are modeled in the experimental setup. The acceptance correction factor is defined as a ratio of the number of reconstructed Monte Carlo events to the number of generated Monte Carlo events. If the experiment is modeled correctly, this ratio is a good estimate of what fraction of events were not measured. Since the simulation has been thoroughly checked, the acceptance correction is beleived to be correct (to within the quoted uncertainties).

All values in this appendix are calculated as

$$\mathcal{A} = \frac{N_{rec}^{MC}}{N_{gen}^{MC}} \tag{A.1}$$

where N_{rec}^{MC} is the number of events remaining after simulation and analysis, and N_{gen}^{MC} is the number of originally generated events in the simulation.

The $\gamma p \to p\pi^0\omega$ detector acceptance plotted versus initial photon energy is shown in Figure A.1. The sudden shift in the acceptance at 1600 MeV is corresponds to the point at which the proton has enough momentum to break free of the target and target structure and is able to be detected in the detector systems .
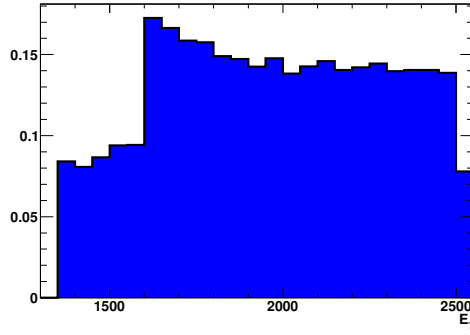
The plots versus $\cos\theta$ are shown in Figures A.2, A.3, and A.4.
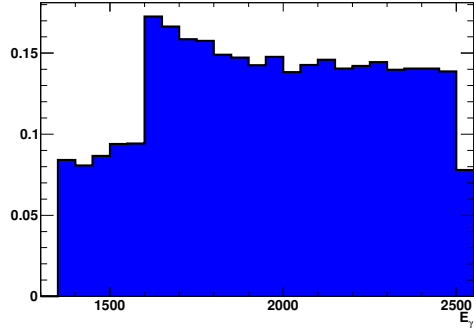
(a) $\omega_{c.m.}$
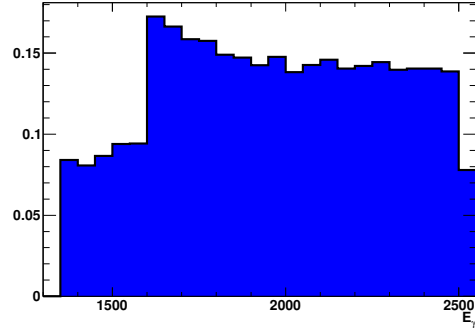
(b) $\pi^0_{c.m.}$

(c) $p_{c.m.}$

Figure A.1: $\gamma p \to p\pi^0\omega$ Acceptance vs E_γ. Each plot is labeled with it's kinematic variable defined in Table 7.1. The horizontal axis of each plot is the energy of the initial photon measured in MeV.
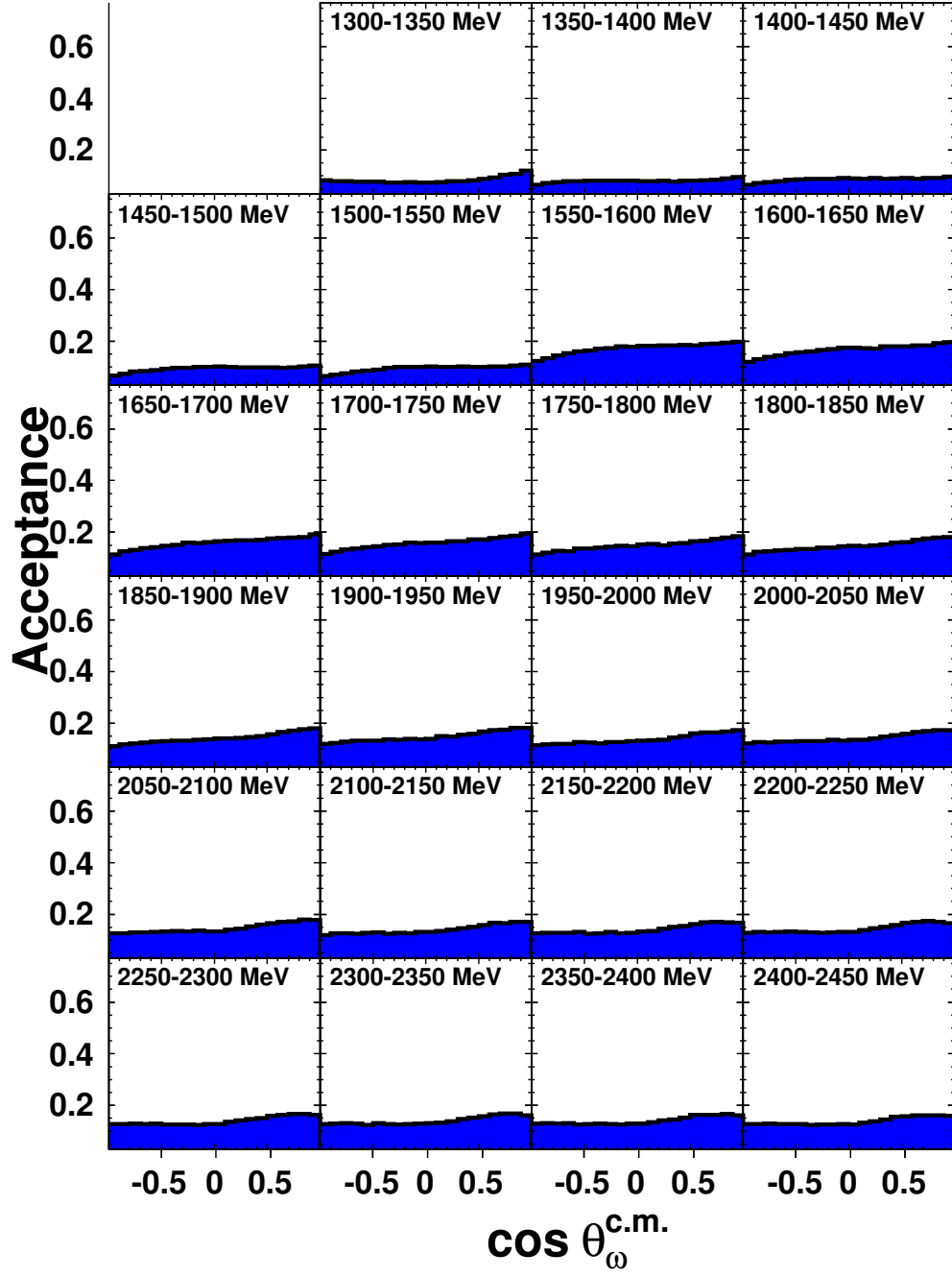
Figure A.2: $\gamma p \to p\pi^0\omega$ Acceptance vs $\cos\theta^\omega_{c.m.}$. Each plot is labeled with its range in initial photon energy.

Figure A.3: $\gamma p \to p\pi^0\omega$ Acceptance vs $\cos\theta_{c.m.}^{\pi^0}$. Each plot is labeled with its range in initial photon energy.

Figure A.4: $\gamma p \rightarrow p\pi^0\omega$ Acceptance vs $\cos\theta^p_{c.m.}$. Each plot is labeled with its range in initial photon energy.
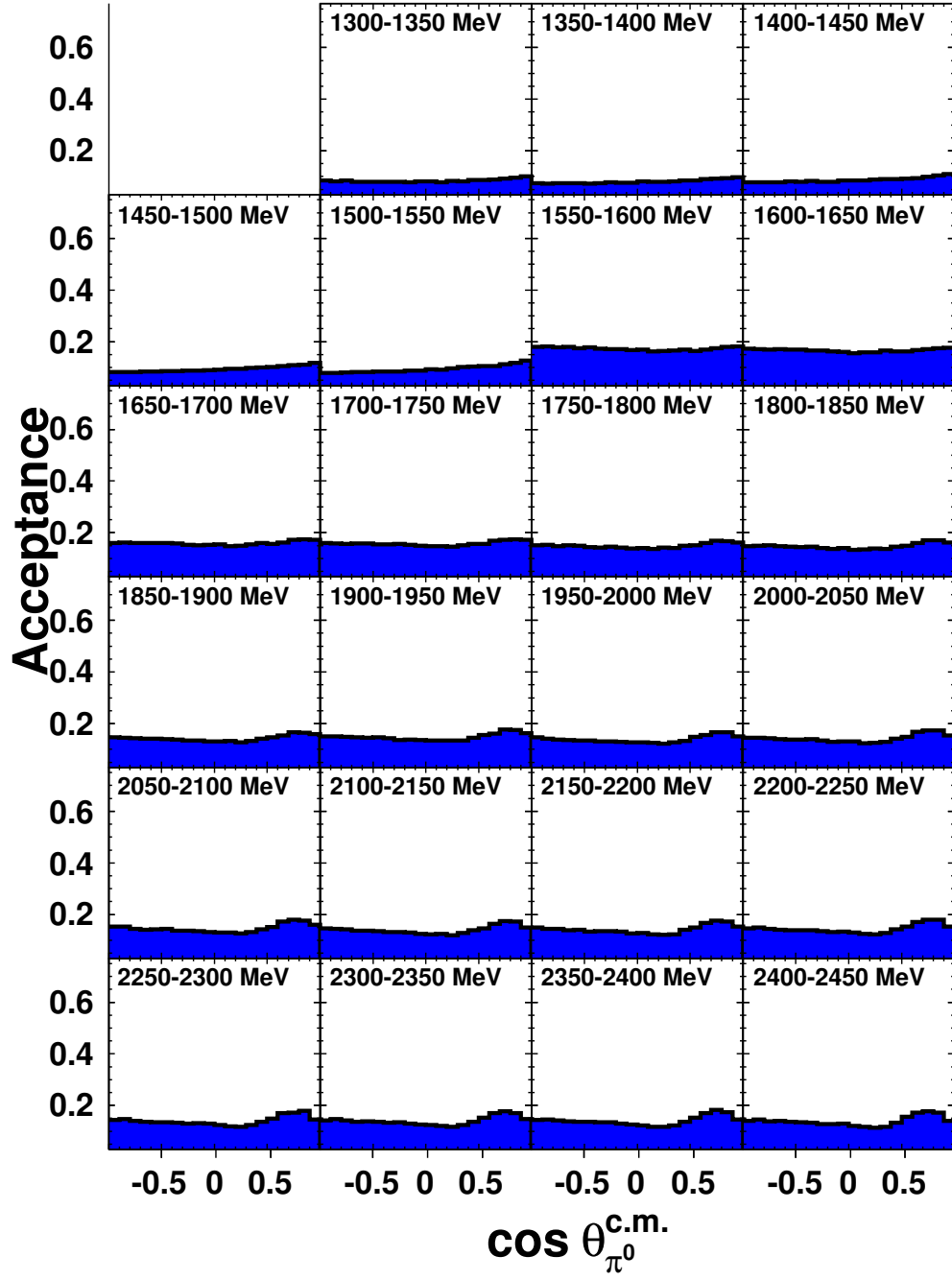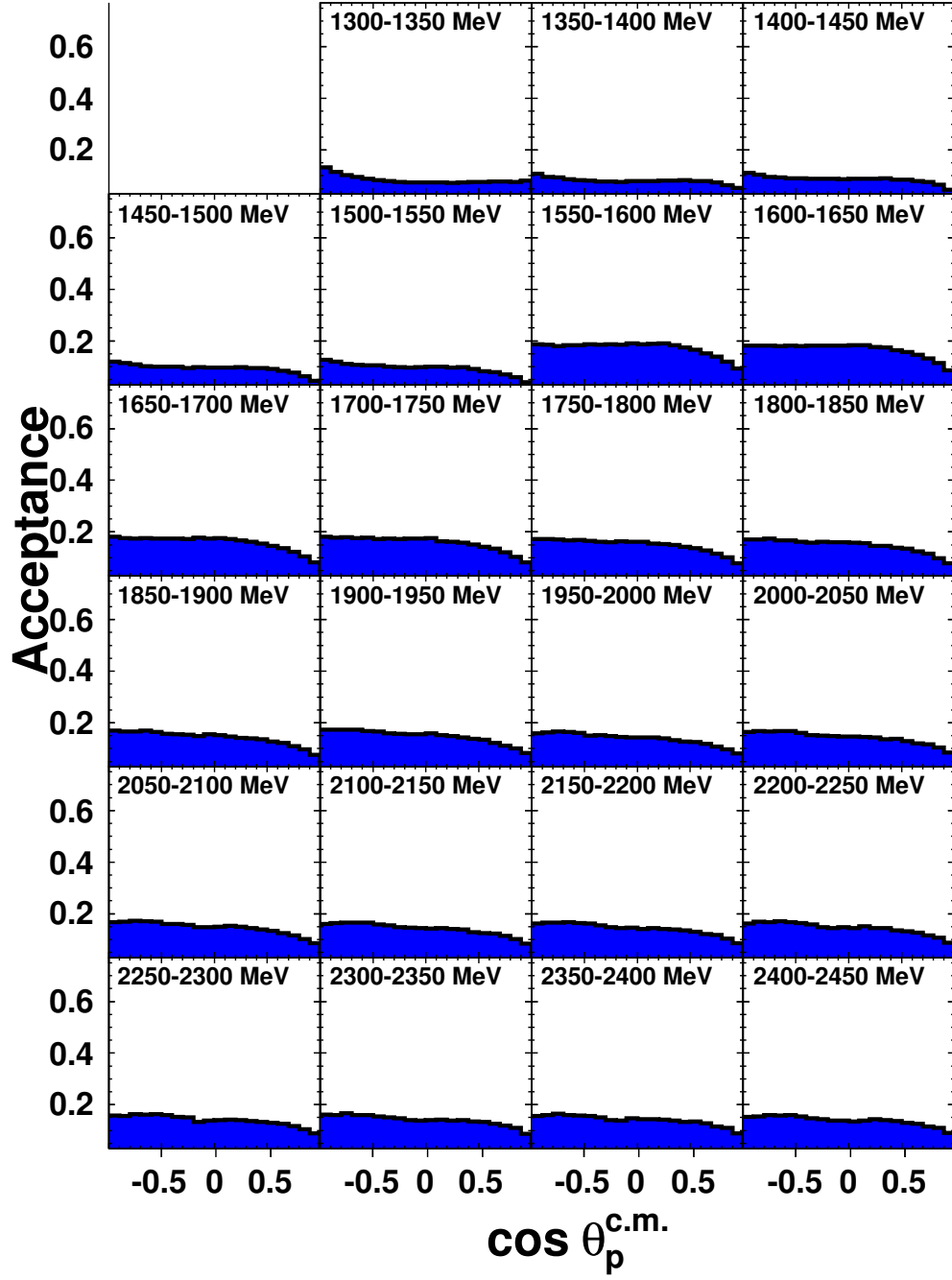
APPENDIX B

TUNING THE FITS IN THE $\gamma p \to p\pi^0\omega$ ANALYSIS

To evaluate how well each Q-factor fit modeled the nearest neighbor invariant mass distribution, the goodness of fit statistic was used. The goodness of fit statistic, also called reduced χ^2 (χ^2_{red}), is defined as

$$
\chi^2_{red} = \frac{1}{\nu} \sum_i \frac{(f_i - d_i)^2}{\sigma_i} \quad ,
\tag{B.1}
$$

where ν is the number of degrees of freedom, d_i is the value of the experimental data in bin i, f_i is the value of the fitted function in bin i, and σ_i is the value of the statistical error of the experimental data in bin i. A distribution which is well described within the error has a $\chi^2_{red} = 1$.

The goodness of fit statistic derived from the Q-factor fits over the experimentally measured data are averaged over all fits in the data set and plotted in Figures B.1 and B.2. The fit quality in Figure B.1 does not vary much with confidence level cut, therefore the confidence level cut was chosen to be low to preserve the maximum number of events in the analysis.

The choice of the number of nearest neighbors has a large effect on the fit quality in Figure B.2. The larger the number of nearest neighbors means the kinematic phase space coverage is larger. The larger phase space volume allows a more complicated background shape and deviates from the assumed background function shape. The number of nearest neighbors has been chosen to be 150. A smaller number of nearest neighbors is not used due to the possibility of a small statistics causing fit instability.
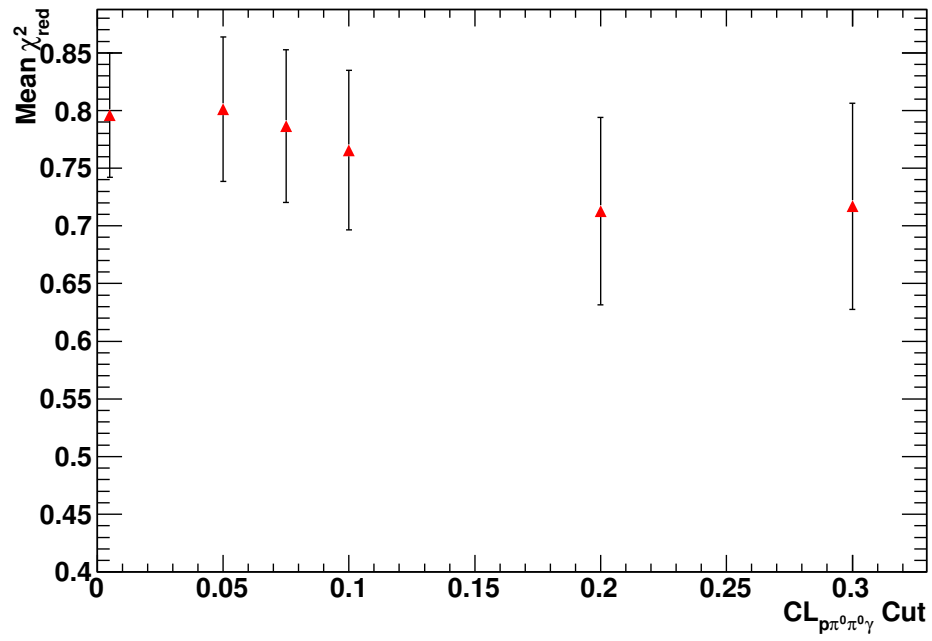
Figure B.1: $\gamma p \rightarrow p\pi^0\omega$ Confidence Level vs. Goodness of Fit Statistic. All the fits were done using 150 nearest neighbors.
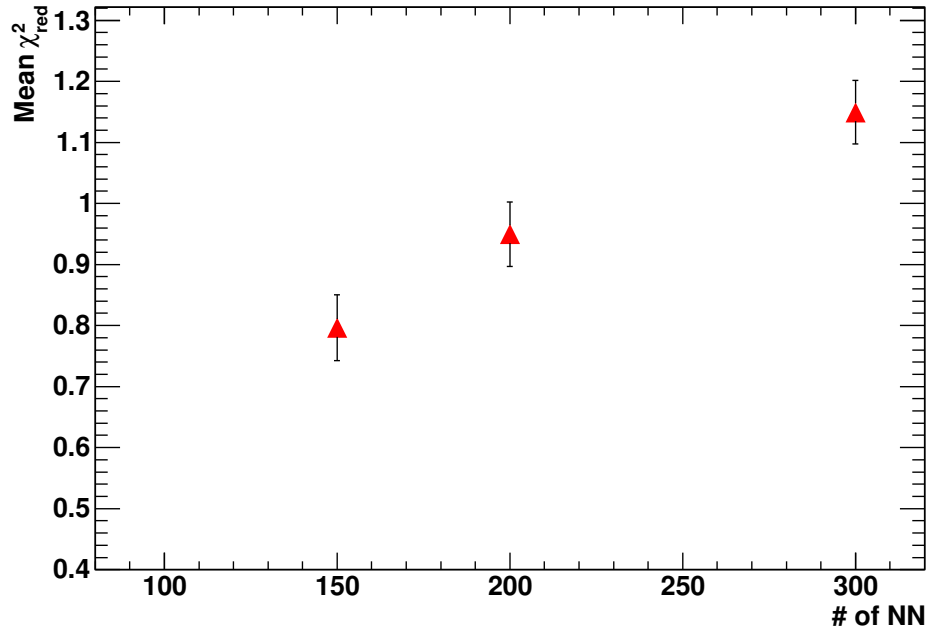
Figure B.2: $\gamma p \to p\pi^0\omega$ Number of Nearest Neighbors vs. Goodness of Fit Statistic. All the fits were done using events which had a confidence level of $CL_{\gamma p \to p_{missing}\pi^0\pi^0\gamma} > 0.005$.

REFERENCES

[1] J. Beringer *et al.*, "Review of Particle Physics (RPP)," *Phys.Rev.*, vol. D86, p. 010001, 2012.

[2] R. G. Edwards, J. J. Dudek, D. G. Richards, and S. J. Wallace, "Excited state baryon spectroscopy from lattice QCD," *Phys.Rev.*, vol. D84, p. 074508, 2011.

[3] U. Loring, B. C. Metsch, and H. R. Petry, "The Light baryon spectrum in a relativistic quark model with instanton induced quark forces: The Strange baryon spectrum," *Eur.Phys.J.*, vol. A10, pp. 447–486, 2001. 45 p. postscript, including 20 figures and 20 tables, submitted to Eur.Phys.J. A Report-no: TK-01-07.

[4] S. Fleck, B. Silvestre-Brac, and J. Richard, "SEARCH FOR DIQUARK CLUSTERING IN BARYONS," *Phys.Rev.*, vol. D38, pp. 1519–1529, 1988.

[5] R. Koniuk and N. Isgur, "Baryon Decays in a Quark Model with Chromodynamics," *Phys.Rev.*, vol. D21, p. 1868, 1980.

[6] S. Capstick and W. Roberts, "N pi decays of baryons in a relativized model," *Phys.Rev.*, vol. D47, pp. 1994–2010, 1993.

[7] S. Capstick and W. Roberts, "Quasi two-body decays of nonstrange baryons," *Phys.Rev.*, vol. D49, pp. 4570–4586, 1994.

[8] S. Capstick and W. Roberts, "Strange decays of nonstrange baryons," *Phys.Rev.*, vol. D58, p. 074011, 1998. 25 pages, 8 figures, RevTeX Report-no: FSU-SCRI-98-42,JLAB-THY-98-15.

[9] E. Klempt and J.-M. Richard, "Baryon spectroscopy," *Rev.Mod.Phys.*, vol. 82, pp. 1095–1153, 2010.

[10] K. Schilling, P. Seyboth, and G. E. Wolf, "On the Analysis of Vector Meson Production by Polarized Photons," *Nucl.Phys.*, vol. B15, pp. 397–412, 1970.

[11] B. Friman and M. Soyeur, "Photoproduction of vector mesons off nucleons near threshold," *Nucl.Phys.*, vol. A600, pp. 477–490, 1996.

[12] V. Shklyar, H. Lenske, U. Mosel, and G. Penner, "Coupled-channel analysis of the omega-meson production in pi N and gamma N reactions for c.m. energies up to 2-GeV," *Phys.Rev.*, vol. C71, p. 055206, 2005.

[13] M. Williams *et al.*, "Partial wave analysis of the reaction $\gamma p \to p\omega$ and the search for nucleon resonances," *Phys.Rev.*, vol. C80, p. 065209, 2009.

[14] M. Williams *et al.*, "Differential cross sections and spin density matrix elements for the reaction gamma p $\to$ omega p," *Phys.Rev.*, vol. C80, p. 065208, 2009.

[15] J. Barth, W. Braun, J. Ernst, K.-H. Glander, J. Hannappel, *et al.*, "Low-energy of photoproduciton of omega-mesons," *Eur.Phys.J.*, vol. A18, pp. 117–127, 2003.

[16] J. Junkersfeld *et al.*, "Photoproduction of pi0 omega off protons for E(gamma) <= 3-GeV," *Eur.Phys.J.*, vol. A31, pp. 365–372, 2007.

[17] M. Sumihama *et al.*, "Backward-angle eta photoproduction from protons at E(gamma) = 1.6 - 2.4 GeV," *Phys.Rev.*, vol. C80, p. 052201, 2009.

[18] W. Hillert, "The Bonn electron stretcher accelerator ELSA: Past and future," *Eur.Phys.J.*, vol. A28S1, pp. 139–148, 2006.

[19] E. Aker *et al.*, "The Crystal Barrel spectrometer at LEAR," *Nucl.Instrum.Meth.*, vol. A321, pp. 69–108, 1992.

[20] J. Ajaka, Y. Assafiri, O. Bartalini, V. Bellini, S. Bouchigny, *et al.*, "Simultaneous photoproduction of eta and pi0 mesons on the proton," *Phys.Rev.Lett.*, vol. 100, p. 052003, 2008.

[21] G. Suft *et al.*, "A scintillating fibre detector for the Crystal Barrel experiment at ELSA," *Nucl. Instrum. Meth.*, vol. A538, pp. 416–424, 2005.

[22] A. Gabler, W. Doering, M. Fuchs, B. Krusche, V. Metag, *et al.*, "Response of TAPS to monochromatic photons with energies between 45-MeV and 790-MeV," *Nucl.Instrum.Meth.*, vol. A346, pp. 168–176, 1994.

[23] R. Castelijns, *Photoproduction of strange mesons and hyperons in the proton*. PhD thesis, Rijksuniversiteit Groningen, 2006.

[24] A. Gabler, W. Doering, M. Fuchs, B. Krusche, V. Metag, *et al.*, "Response of TAPS to monochromatic photons with energies between 45-MeV and 790-MeV," *Nucl.Instrum.Meth.*, vol. A346, pp. 168–176, 1994.

[25] V. Crede *et al.*, "Photoproduction of eta and eta-prime mesons off protons," *Phys.Rev.*, vol. C80, p. 055202, 2009.

[26] T. Awes, F. Obenshain, F. Plasil, S. Saini, S. Sorensen, *et al.*, "A Simple method of shower localization and identification in laterally segmented calorimeters," *Nucl.Instrum.Meth.*, vol. A311, pp. 130–138, 1992.

[27] V. Hejny, *Photoproduktion von eta-Mesonen an Helium 4.* PhD thesis, Physikalisches Institut Universitat Giessen, 1998.

[28] J. Junkersfeld, "*Kalibration des Crystal-Barrel-ELSA Detektors mit Hilfe der Reaktion $\gamma p \to p\pi^0$.* Helmholtz-Institut fur Strahlen- und Kernphysik, Universitat Bonn." Diploma Thesis, 2000.

[29] J. Junkersfeld, *Photoproduktion von $\pi^0\omega$ am Proton bei Energien bis zu 3 GeV.* PhD thesis, Helmholtz-Institut fur Strahlen- und Kernphysik, Universitat Bonn, 2005.

[30] V. Crede, "*CBGEANT 1.08/01.*" CB Note, October 2001.

[31] M. Williams, M. Bellis, and C. Meyer, "Multivariate side-band subtraction using probabilistic event weights," *JINST*, vol. 4, p. P10003, 2009.

[32] W. Verkerke and D. P. Kirkby, "The RooFit toolkit for data modeling," *eConf*, vol. C0303241, p. MOLT007, 2003.

[33] H. Albrecht *et al.*, "Measurement of the polarization in the decay B → J / psi K*," *Phys.Lett.*, vol. B340, pp. 217–220, 1994.

[34] Q. Zhao, J. Al-Khalili, and P. Cole, "Vector meson photoproduction studied in its radiative decay channel," *Phys.Rev.*, vol. C71, p. 054004, 2005.

[35] C. Amsler *et al.*, "Anti-proton - proton annihilation at rest into two-body final states," *Z.Phys.*, vol. C58, pp. 175–190, 1993.

[36] O. Bartholomy *et al.*, "Neutral pion photoproduction off protons in the energy range 0.3-GeV < E(gamma) < 3-GeV," *Phys.Rev.Lett.*, vol. 94, p. 012003, 2005.

[37] I. Horn *et al.*, "Study of the reaction gamma p → p pi0 eta," *Eur.Phys.J.*, vol. A38, pp. 173–186, 2008.

[38] U. Thoma, M. Fuchs, A. Anisovich, G. Anton, R. Bantes, *et al.*, "N* and Delta* decays into N pi0 pi0," *Phys.Lett.*, vol. B659, pp. 87–93, 2008.

BIOGRAPHICAL SKETCH

I was born in Ashburn, Georgia on November 19, 1977. Except for a year when I lived in Santa Cruz, California, when I was 4 years old, I grew up in Ashburn and graduated from Turner County High School. During high school, I took my first physics class and enjoyed the mathematical reasoning used in solving the assigned problems.

My first college experience took place at Abraham Baldwin Agricultural College (ABAC) in Tifton, Georgia. I spent two years at ABAC where I was the only student to declare a physics major within recent memory. After taking all the useful physics and mathematics courses offered at ABAC, I transferred to the University of Georgia (UGA) in Athens, Georgia. At UGA, I graduated with a Bachelor of Science degree in Physics in December 2000.

During my time at UGA, I was hired as a student worker at the National Ultraviolet Monitoring Center (NUVMC). This center was a Environmental Protection Agency supported program which was charged with monitoring the amount of ultraviolet radiation at several sites around the US. I was hired on full time as a calibration technician in June 2000 and then promoted to Network Manager at the end of 2002. However, the funding for this program was in danger of being cut during the spring of 2003 and I opted to take a job teaching.

I taught math and science to middle school and high school students in the same school system I grew up in for two years. I was able to briefly indulge a childhood dream of coaching athletics at the high school level during this time. I taught high school physics, chemistry and physical science to high school student at Turner County High School and was fortunate enough to teach my own brother, Patrick, high school physics during the 2005-2006 school year.

At this point in my life, I decided that I needed to continue with my dream of obtaining a PhD in Physics and pursuing a career in research. I enrolled in the PhD physics program at UGA during the 2006-2007 school year, with the idea to get started in a familiar department. During this time I met Dr. Kanzo Nakayama who introduced me to hadronic physics. Through my brief time working with Dr. Nakayama, I decided to pursue a career in experimental hadronic physics and applied to the Florida State University Physics Department the following year.

Upon applying to FSU, I contacted my current thesis adviser Dr. Volker Crede and started working with him the summer before starting classes at FSU. He promptly

sent me to Bonn, Germany to start working on the CBELSA/TAPS experiment, which of course led to this thesis.

I gave two conference talks during my time at Florida State University. The first was at the Hadron 2009 conference held in Tallahassee, Florida in 2009 and was titled "Helicity Beam Asymmetry I° in Two Neutral Pseudoscalar Photoproduction Reactions at the Crystal Barrel Experiment". I also published a conference proceedings paper on this talk with the same title in "AIP Conf.Proc. Vol. 1257. HADRON 2009: Proceedings of the XIII International Conference on Hadron Spectroscopy, pp.607.". The second talk was given at the NSTAR 2011 conference held in Newport News, Virginia in 2011 and was titled "ω Photoproduction at the CBELSA/TAPS Experiment.". I also published a conference proceedings paper with the same title in "AIP Conf.Proc. Vol. 1432. THE 8TH INTERNATIONAL WORKSHOP ON THE PHYSICS OF EXCITED NUCLEONS:NSTAR 2011, pp.409."

I was involved in the publishing of three papers during my graduate student career at Florida State University. These are :

- N. Sparks *et al.* [CBELSA/TAPS Collaboration], "Measurement of the Beam Asymmetry Σ in the Forward Direction for $\vec{\gamma}p \to p\pi^0$ Photoproduction," Phys. Rev. C **81**, 065210 (2010).

- V. Crede *et al.* [CBELSA/TAPS Collaboration], "Photoproduction of Neutral Pions off Protons," Phys. Rev. C **84**, 055203 (2011).

- A. Thiel *et al.*, "Well-established nucleon resonances revisited by double-polarization measurements," Phys. Rev. Lett. **109**, 102001 (2012).

As a result of the work in this thesis, several papers are in preparation.